U.PORTO

FEUP FACULDADE DE ENGENHARIA
UNIVERSIDADE DO PORTO

Multi-field Modeling of Composite Structural Batteries

Rui Martim Lopes Busto Salgado

Thesis submitted to the Faculty of Engineering of the University of Porto - FEUP
in partial fulfillment of the requirements for the degree of
Master in Mechanical Engineering

Supervisors
Prof. Dr. Pedro Manuel Ponces Rodrigues de Castro Camanho
Prof. Dr. Maria Helena Braga
Prof. Dr. Anter El-Azab

Mestrado Integrado em Engenharia Mecânica (MIEM)
Departamento de Engenharia Mecânica (DEMec)
Faculdade de Engenharia (FEUP)
Universidade do Porto (UP)

Porto, September 2021

Acknowledgements

I take this opportunity to express my gratitude to Prof. Pedro P. Camanho, Prof. M. Helena Braga and Prof. Anter El-Azab for taking the time to share their expertise and for all the support and encouragement given over the past few months without which this work would not have been possible.

I would also like to mention the great respect and admiration I have developed for Prof. Pedro P. Camanho, who introduced me to his research family when I was still a young and inexperienced undergraduate.

I gratefully acknowledge the financial support provided by the Fulbright Commission Portugal and FLAD, under grant *Fulbright Research Grant with FLAD's support*. I would also like to acknowledge the institutional support of INEGI, LAETA, and Purdue university.

I would like to thank my colleagues at University of Porto, Dr. Albertino Arteiro, Dr. Fermin Otero, Dr. Rodrigo Tavares, Dr. Carolina Furtado, Dr. Federico Danzi, Luís Pereira, Giuseppe Corrado, and at Purdue, Sanjoy Kumar, Sreekar, Kyle Starkey, Joseph Anderson, Ahmad Ahmad, and Vignesh for their feedback, cooperation and friendship.

Finally, I thank my friends, my parents and my family for providing me with all the friendship and support I could ask for the last five years.

Abstract

The main purpose of this work is to develop a tool to aid the design of a next generation multifunctional material system commonly referred to as a *structural battery* or a *composite battery*. The main goal is to develop analysis models to study and predict their material, structural and system behavior involving coupled fields phenomena occurring at several length scales. A numerical finite element framework to study the multi-physics evolution at a component/macro scale is proposed and focused on the fracture and damage characterization at the engineering fracture mechanics length scale. A modeling technique of loosely coupling temperature, chemical, or other relevant fields with the displacement, (elastic) strain and stress fields is proposed. On the other hand, a strong coupling between the elasticity fields and macroscopic crack evolution is considered. To capture relevant cracking phenomena such as crack initiation, propagation, and deflection, a phase field model for brittle fracture was implemented.

The numerical analyses presented were validated by studying state-of-the-art benchmark problems usually encountered in other works concerned with phase field models for brittle fracture. A good agreement with benchmark results taken from the literature is obtained. A comparison between different modeling techniques is presented focusing on their effect on maximum strength, structural stiffness, crack propagation and load drop during collapse. It was concluded that the model is able to capture crack phenomena such as initiation, propagation, and crack irreversibility and stiffness recovery due to tension-compression load reversal.

A phase-field fracture model loosely coupled with simple diffusion problems obeying Laplace's equation was also considered. A numerical analysis for a coupled fracture and transient heat conduction single-edge notched tension specimen with prescribed temperature and insulation showed that physically accurate results can be obtained by considering loose coupling of fracture problems with thermal fields. Moreover, it was also highlighted that the presence of temperature gradients significantly influences the structural response of a material.

An experimental mechanical characterization of a new composite battery is also addressed in this thesis. A three point bending test was performed until the point of structural collapse. The material system tested has been recently patented by the MatER - Materials for Energy Research-Group - and has resulted from a joint effort by the Physics and Mechanical departments at FEUP, and researchers at INEGI. The design is based on a all-solid-state glass electrolyte-based sodium battery with auto and thermal charge capability as the electrochemical harvesting material, and a carbon fibre thin-ply quasi-isotropic laminate as the structural element. The multi-functional (structural and energy storage) beam battery showed very promis-

ing results for system-level mass reduction. Furthermore, by introducing multi-functionality, the failure mode obtained for the beam changed from a progressive load and stiffness degradation to a pseudo-ductile structural behavior improving the post-peak bending response of traditional tubular beams.

Contents

Acknowledgements **i**

Abstract **v**

Contents **v**

List of figures **viii**

List of tables **xi**

List of symbols **xiii**

I Introduction **1**

1 Introduction **3**
1.1 Motivation and objectives 3
1.2 Thesis layout 5

II Literature Survey **7**

2 Fracture and Damage models **9**
2.1 Energy models for brittle fracture 9
2.2 Numerical methods for LEFM and NLFM 9
2.2.1 Diffuse models 10
2.2.2 Remarks on continuum damage models 11
2.3 Brief introduction to the modeling of microstructures using the phase field approach 15
2.4 The variational approach to fracture. Phase field models for brittle fracture 18
2.4.1 Regularized form of the fracture functional 20
2.4.2 Influence of the length scale parameter l on diffuse crack topology 23
2.5 Strain energy degradation 23
2.5.1 Strategies to impose crack field irreversibility 25
2.5.2 Penalization 27
2.6 Algorithm Schemes 27
2.7 Interpreting the variational approach to fracture as a phase-field model of brittle fracture 28

2.8 Material and Numerical Parameters 29
2.9 Hybrid Formulation 30
2.10 Understanding the phase-field approach to fracture as a damage model 30

3 Coupled Problems 33
3.1 Miehe's thermodynamically consistent model for coupled problems . 33
3.1.1 Purely geometric approach 33
3.1.2 Evolution of the crack surface 34
3.1.3 Constitutive crack driving functional 34
3.1.4 Equilibrium equations 35
3.1.5 Numerical solution of the evolution equation 36
3.2 Algorithm scheme 37
3.3 Diffusion problems in fractured media 37
3.3.1 Definition of material degradation for diffusion problems . . . 38
3.4 Heat Transfer problem in solid media 39
3.4.1 Weak and FEM form of the 2-D transient heat equation . . . 39
3.5 Concluding remarks 41

III Phase-field analysis models to predict brittle fracture in coupled problems 43

4 A Phase Field Model for Brittle Fracture 45
4.0.1 Ensuring a Correct Physical Behavior 47
4.0.2 FEM discretization of the Domain 49
4.0.3 Determination of Numerical/Material Parameters 50
4.0.4 Algorithm Scheme 51
4.1 Rate-independent models 51

5 Model Implementation 53
5.1 Introduction 53
5.2 Numerical and modeling aspects 53

6 Model validation 59
6.1 SENT - Single-edge notched tension test 60
6.1.1 Monolithic solution 60
6.1.1.1 Effect of initial mesh size and h-adaptivity levels . . 63
6.1.1.2 Effect of refinement threshold 63
6.1.2 Staggered solution 65
6.2 SENS - Single-edge notched shear test 67
6.2.1 Monolithic solution 67
6.2.2 Crack path prediction for mode-II loading 68
6.3 L-shaped panel test 69
6.3.1 Monolithic and staggered results 69
6.4 Concluding remarks 73

7 Coupled thermo-mechanical SENT model 75
7.1 Introduction 75
7.2 SENT test with time-dependent heat conduction 75

IV Experimental work **81**

8 Flexural response of an all-solid-state structural beam-type battery **83**
8.1 Introduction 83
8.2 Material characterization. Fabrication and configuration of test specimens 85
8.3 Results and discussion 87
8.4 Concluding remarks 93

V Conclusions and future work **95**

9 Conclusions and future work **97**
9.1 Conclusions 97
9.1.1 Phase-field models to predict the failure of brittle materials . 97
9.1.2 Coupled problems modeling 97
9.1.3 Bending response of a coaxial structural battery 98
9.2 Future work 98

VI Appendix **101**

Appendix A Peak stress for a 1D bar in tension with prescribed displacement **103**

List of Figures

2.1 (left) Damaged and (right) effective configurations considered in damage models . . . 12
2.2 Diffuse 1-D crack topology for distinct values of the length scale parameter l . . . 23
2.3 Phase-field model behavior for compressive states: unphysical stiffness degradation for the isotropic formulation . . . 27

3.1 Unnotched heat flux and concentration of the thermal field near the crack . . . 39
3.2 Heat conduction in a solid with internal heat source . . . 40

4.1 Definition of the continuum and nomenclature considered for the variational statement. Representation of a diffuse crack topology. Adapted from [1] . . . 45

6.1 SENT test configuration. Adapted from [2] . . . 61
6.2 SENT mesh using h-adaptivity . . . 61
6.3 Crack field at (a) initial and (b) final load steps. . . . 62
6.4 SENT test results: load-displacement curves for monolithic solution 62
6.5 Mesh size effects on SENT test force-displacement curve . . . 64
6.6 Effect of refinement threshold on the force-displacement curves . . . 65
6.7 SENT simulation using a staggered scheme: (left) crack path and (right) final mesh topology. Displacement scale factor = 2 . . . 66
6.8 SENT test results: load-displacement curves for monolithic and staggered solution . . . 66
6.9 SENS test configuration. . . . 67
6.10 SENS test results: load-displacement curves for monolithic solution . 68
6.11 Monolithic SENS test crack path and mesh for the final load step . . 69
6.12 L-shaped panel test definition . . . 70
6.13 Force-displacement curve for the L-shaped panel test . . . 71
6.14 Evolution of cracks for the l-shaped panel test . . . 72

7.1 Thermal boundary conditions for the SENT heat transfer problem . 76
7.2 Effect of thermo-mechanical coupling on the force-displacement curve for the SENT heat transfer problem. . . . 77
7.3 Vertical displacement (u_y) and temperature field for the load step prior to initial crack propagation. . . . 78
7.4 Heat flux concentration near the crack tip . . . 79

7.5 σ_{yy} field near the crack tip 79

8.1 Simplified drawing of the outer shell and experimental setup for the beam battery bending tests. The hollow entire is completely filled for beam cell configurations 86
8.2 Visual description of test setup and measurements 87
8.3 Experimental force-displacement curves obtained in previous (prev.) [3] and current three point bending tests 89
8.4 Experimental force-strain curves obtained for all three point bending tests 90
8.5 Mid-section ovalization due to the mechanical test of composite batteries 90
8.6 Multi-functional vs traditional structural and energy storage systems 92
8.7 Multi-functional test [3]: LED light bulb powered by a beam battery loaded in bending 94

A.1 Fixed-free 1D bar with homogeneous damage growth and prescribed displacement at the free end 103

List of Tables

2.1 Fracture functional parameters for the linear and quadratic models . 21

6.1 Nomenclature for Solid Mechanics parameters 59
6.2 Meshing parameters 59
6.3 Model and material parameters for the SENT test 60
6.4 Peak values (U,P) and stiffness comparison between benchmark and monolithic results for the SENT 63
6.5 Peak values (U,P) obtained for monolithic simulations of the SENT using different values of α_{ref} 65
6.6 Peak values (U,P) and stiffness comparison between benchmark, monolithic and staggered results for the SENT 66
6.7 Peak values (U,P) and stiffness comparison between benchmark and monolithic results for the SENS 68
6.8 Model and material parameters for the L-shaped panel test 70
6.9 Peak values (U,P) and stiffness comparison between benchmark, monolithic and staggered results for the l-shaped panel test 71

7.1 Nomenclature for Heat transfer parameters 75
7.2 Model and material parameters for the SENT with heat transfer test 76
7.3 Peak values (U,P) and stiffness comparison for the SENT heat transfer problem with and without thermo-mechanical problem 77

8.1 Configurations tested for the three-point bending test 85
8.2 Nominal dimensions of the battery components according to Fig. 8.1 86
8.3 Real cross-section dimensions of the three specimens 87
8.4 Structural batteries and CFRP outer shell beams bending performance: peak load, P, mass, m, and specific maximum load, $\bar{P}$ 89
8.5 Experimental data reported in [3] for the performance of the Na^+-ASSB composite battery 92
8.6 Multi-functional performance of the structural batteries 92

List of symbols

General nomenclature

$\mathbf{x}$	Position vector in a Cartesian coordinate system
t	time parameter
$\nabla()$	Gradient operator
$\Delta()$	Laplace operator
$\frac{\partial()}{\partial()}$	Partial derivative operator
$\frac{\delta()}{\delta()}$	Total variation operator
$\bar{\mathbf{t}}$	Traction force vector
$\mathbf{B}$	Body force vector
Ω	Bulk 2D or 3D domain
$\partial\Omega$	Surface 1D or 2D domain associated with Ω
$\partial\Omega_N$	Surface domain with Neumann-type boundary conditions
$\partial\Omega_D$	Surface domain with Dirichlet-type boundary conditions
$\mathcal{G}$	Energy release rate
$\mathcal{G}_c$	Critical energy release rate
$\delta(x)$	Dirac-delta function
Π	Functional defined for a variational problem
H^1	Sobolev space of support for the solution of the partial differential (in)equations

Chapter 2 - Damage models

ϕ_1	Damage variable, effective area reduction
l_1	Damage variable, effective stiffness reduction
$(\bar{\square})$	Property measured in the effective configuration
D_i	Damage variable for property i
$\mathbf{I}_8$	Eighth-rank identity tensor
$\mathbf{D}_8$	Eighth-rank damage tensor
Ψ	Helmholtz free energy density
N_k	Internal state variable k

G	Complementary free enery density
d_i	Scalar damage variable i
α_{ii}	Coefficient of thermal expansion along direction i
β_{ii}	Coefficient of hygroscopic expansion along direction i
$\mathbf{H}$	Compliance tensor (obtained from the complimentary free energy density)
F_N	Damage activation function N
ϕ_N	Loading history function N
r_N	Elastic domain threshold expressions

Chapter 2 - Phase-field models

k	thermal conductivity
ρ	Mass density
c_p	specific heat at constant pressure
L_f	Latent heat of fusion for solidification
V_n	Velocity normal to the evolving interface
κ	interface curvature
γ	solid-liquid surface energy
μ	Local atomic interface mobility
c_i	Conserved phase-field variable i
η_i	Order parameter i
ϕ_i	Phase-field variable i
F	Free energy of a bulk system
L_i	Mobility associated with the order parameter η_i
f_0^j	Homogeneous free energy functional associated with phase j
$\mathbf{v}$	Set of fields/state variables relevant for the phase-field problem
κ	Gradient energy coefficient
$h(\phi)$	Interpolation function (interpolation for bi-phasic system)

Chapter 2 - Brittle fracture variational models

Γ_i	Sharp crack surface at step i
E	Energy functional
F_A	Closed subset of $\partial\Omega$ where a crack may occur
Ψ	free energy density
$\mathcal{H}^{n-1}$	Hausdorff measure of surface
c	Field governing the evolution of the diffuse crack
c_w	Scaling parameter of the regularized energy functional
w_c	Geometric (*local*) homogeneous evolution function

l	length scale parameter
$\gamma(c, \nabla c)$	crack surface density function
$f(c)$	Degradation function
Ψ^+	Positive (or active) component of the strain energy density
Ψ^-	Negative (or passive) component of the strain energy density
λ	Lamé's first parameter
μ	Lamé's second parameter
$\boldsymbol{N}_i^{\varepsilon}$	eigenvector i
k	Residual stiffness
$E_{\mathbf{u}}$	Equations obtained from the variational statement (displacement field)
E_c	Equations obtained from the variational statement (c field)
V	Space of admissible functions for the displacement field
v	Displacement test functions
β	c field test functions
$\mathcal{H}$	History field variable
λ_P	Penalty parameter
d	Phase-field variable for brittle fracture problems
$\mathcal{G}_c^{eff}$	Effective numerical fracture toughness
h	Finite element characteristic size
l_0	Engineering expression for determining the length-scale parameter
M_η	Mobility parameter for damaged models
$h(\eta)$	Free energy interpolation function
$wg(\eta)$	Damage energy dissipation function

Chapter 3 - Phase-field model for coupled fracture problems

S	Constitutive crack driving functional
$\mathcal{R}$	Local viscous crack resistance
η	Viscosity parameter

Chapter 3 - Coupled diffusion problems

$\phi(x, y)$	Scalar potential function
$f(x, y)$	Diffusive flux
$k(d)$	Degraded material property
$g(d)$	Interpolation function for degraded material properties
k_i	Thermal conductivity along direction i
C	Thermal capacity

$\dot{g}$	heat generation function
w	Test function

Chapter 4

V	Space of admissible functions for the displacement field
D	Space of admissible functions for the phase field
g(d)	Strain energy degradation function
λ	Lamé's first parameter
μ	Lamé's second parameter

Chapter 8

R_0	Layer outer radius
d_0	Layer outer diameter
t	Layer thickness
L	Layer length
K	Stiffness (measured from three-point bending force-displacement curves)
P	Peak load
$\bar{P}_{sb}$	Specific peak load for structural batteries
$\bar{P}_{CFRP}$	Specific peak load for CFRP tubular beam
$\bar{E}_{sb}$	Energy density for structural batteries
$\bar{E}_{CFRP}$	Energy density for CFRP tubular beam
P^*	Maximum admissible load
m_{sb}	Mass of structural battery
m_b	Mass of traditional battery
m_{CFRP}	Mass of CFRP tubular beam
m_{trad}	Sum of the mass of equivalent traditional system
α	Structural efficiency parameter
β	Energy storage efficiency parameter

Part I

Introduction

Chapter 1

Introduction

1.1 Motivation and objectives

Composite batteries or structural power composites result from the combination of structural and energy harvesting phases at a macro, meso, or micro-scale. While these materials can be distinguished from traditional composite materials due to their multi-functionality, they are still covered by the definition of the latter. There is a multitude of combinations between different sub-materials to simultaneously achieve structural performance and energy storage using one material. A fundamental difference between different concepts is the scale at which multi-functionality is obtained:

- Macro-scale integration, where a pre-existing energy storage material system is embedded in a structure with minimal redesigning of both and demanding a redefinition of the manufacturing process for the structure. Examples of such material is embedding a Li-ion battery in a sandwich structure or incorporating a Li-ion battery pack into the chassis.

- Meso-scale integration, where both structure and energy storage system are redesigned resulting in new sub-materials that combine structural and energy storage features. The impact on the manufacturing process (at a macro-scale) may be minimal depending on the design solution. An example of such material is a laminated power composite where some layers act as electrodes and an electrolyte interphase exists.

- Micro-scale, where each homogeneous phase is a truly multi-functional material that provides both structural integrity and an active role on energy harvesting mechanisms. Again, the impact on the manufacturing process is highly dependent on the multi-functional solution found. On the other hand, novel raw materials must be considered. An example of such material is a laminated fiber-reinforced polymer (FRP) composite where the fibres act as the cathode/anode materials and the matrix acts as electrolyte and separator.

Historically, research and technological development of these multi-functional materials has been promoted by the hardware industry and by the vehicles industry. Focusing on the latter, one of the earliest contributions date back to the US military efforts to realize a structural battery engineered at the micro-scale in mid-2000s. Since then, the challenging task of developing materials providing satisfying performance indicators for both functionalities (structural and energy storage) has led

to several different design ideas for which *compromise* is the key word. For vehicles, the end goal with multi-functionality is system-level mass savings driven not only by emission reduction but also by vehicle performance. In fact, both can be complementary, as is shown by the difficulty faced by the aeronautical industry in developing electrical commercial airplanes with enough specific energy and power to accomplish mid- or long-distance flights.
The present work has been developed within a broader project targeting the development of novel structural power composites for vehicles enabling disruptive future mobility solutions in terms with global sustainability goals and follows the extensive review works focusing on the state-of-the-art of electric vehicles batteries and structural batteries [4, 5] that led to the following main conclusions:

- Li-ion batteries possess a dominant market share over other energy storage alternatives for electric vehicles. Within Li-ion technology, only five different cathodes are used, and the recent tendency has been to increase the use of nickel percentage on the cathode material.

- The market share of electric automobiles is increasing at a fast pace and may soon be leveled with that found for internal combustion engine cars. Moreover, electric ships have also gained importance over the last few years, and a continuous increase on production of new electrified vessels is expected. However, the first fully electric commercial flight is far from being realized due to the insufficient compromise between energy density and lift achieved with present-day state-of-the-art battery technology.

- Present-day research efforts are mainly focused on improving the cycle life of these batteries. The complex degradation phenomena occurring within the electrodes and associated with the electrolyte interfaces have been extensively studied and solution to mitigate their effects on cell performance have been proposed. However, most of these solutions are unfeasible for industrial-scale technologies.

- In spite of recent efforts to improve the safety of Li-ion batteries, the presence of a flammable liquid electrolyte poses a significant risk of explosion.

- All-solid-state batteries with a ferroelectric as the solid electrolyte may be the future disruptive step that resolves the main issues of present-day Li-ion batteries. Besides overcoming the (1) safety problem related to the flammability of liquid electrolytes, all-solid-state batteries exhibit (2) longer cycle life and (3) higher energy/power density than present-day alternatives, while also (4) allowing for faster charge rates. these are the four main drawbacks of electric vehicles available on the market.

- The (1) integration of commercially available Li-ion batteries in composite structures, and the (2) fabrication of carbon fibre-based multifunctional materials (macro- and micro-scale designs) are two multi-functional material solutions of particular interest. The latter shows the highest potential for system-level mass reduction by synergistically combining the fibres and plymeric matrices with ionic salts and cathodic materials to fabricate truly multi-functional monolithic materials. Moreover, the main challenges faced by these configurations are the maximum temperature allowable during the curing cycle and

the realization of electrolytes with sufficient ionic conductivity and structural performance. While some research works have idealized this structural electrolyte as a bi-phasic solid/liquid material (structural/conductive phases, respectively), the use of solid-state electrolytes that overcome the poor structural behavior of such bi-phasic configurations based on solid-state electrolytes is suggested in [4].

During the course of this work, a macro-scale composite battery was developed at FEUP [3] using an all-solid-state (ASS) sodium battery embedded in a laminated thin-ply carbon fiber composite. However, comprehensive studies still need to be conducted to assess the electro-chemo-thermo-mechanical behavior of these materials, especially the failure mechanisms that control their final failure. Given the complexity of the phenomena involved, developing simulation techniques to study all these aspects is paramount. It is considered that numerical models capable of performing such simulations are the only viable option for optimizing the multifunctional material system and aid their iterative design. The objective of this work is to lay out the first steps in developing a computational tool capable of providing an insight into the behavior of these materials and to further elaborate on their experimental characterization.

1.2 Thesis layout

This thesis is divided in five parts. In Part II, the literature review is presented with a first chapter dedicated to phase-field models for brittle fracture and a second chapter where the addition of coupled fields to the previous models is addressed.

In Part III of this thesis, an analysis model to predict brittle fracture using the phase-field technique and a coupling strategy to model multi-field problems is presented in detail. In Chapter 4, a finite element modeling methodology to simulate fracture mechanics problems is considered. The proposed methodology is used throughout the remaining part of the numerical work. In Chapter 6, three numerical results are presented to validate the phase-field model with a clear emphasis on the ability to model distinct macro-scale crack phenomena. Chapter 7 introduces a thermo-mechanical numerical problem to assess the ability to model coupled thermo-mechanical fields.

In Part IV, an experimental work to determine the bending response of a structural composite battery is presented. Given the dissimilarities between this and the remaining parts of this work, brief introductory remarks are made to help clarify the concept behind these material systems, as well as some of the research challenges commonly faced in this field. Based on the experimental data obtained for a three-point bending test, the effect of redesigning a tubular carbon fibre beam to incorporate multi-functionality (structural and energy storage) is explored.

Finally, the main conclusions of the work carried out and potential future modeling and structural battery design developments are presented in Part V.

Part II

Literature Survey

Chapter 2

Fracture and Damage models

2.1 Energy models for brittle fracture

The theory of Fracture Mechanics applied to brittle materials has its foundations in the work published by Griffith where a quantitative relation between flaw size, a, and fracture stress, σ_r, was first proposed. By invoking the first law of thermodynamics, the governing expression for brittle fracture was obtained [2] considering the theorem of minimum potential energy,

$$\frac{dE}{d\ \mathrm{A}} = \frac{d\Pi}{d\ \mathrm{A}} + \frac{dW_s}{d\ \mathrm{A}} = 0 \tag{2.1}$$

where E is the total energy, Π the potential energy due to the strain energy and external work, and W_s is the energy associated with the formation of crack surfaces that, for perfectly brittle materials, is equal to twice the surface energy, γ_s. Introducing the fracture toughness material parameter $\mathcal{G}_c$ and the *energy release rate*, expression 2.1 may be re-written in its usual form that defines the conditions for crack propagation:

$$\mathcal{G} = -\frac{d\Pi}{d\ \mathrm{A}} = \mathcal{G}_c \tag{2.2}$$

where $\mathcal{G} = \frac{dW_s}{d\ \mathrm{A}}$.

Considering the simplicity of the model proposed by Griffith, the fact that all phase-field (PF) models (and many different modeling strategies) developed are based on this competition between fracture energy and potential energy, as will be seen in section 2.4, is remarkable. Together with stress based models relying on the concept of stress intensity factor $\mathcal{K}$, this model established the foundations for the development of Linear Elastic Fracture Mechanics (LEFM) and non-linear fracture mechanics (NLFM).

2.2 Numerical methods for LEFM and NLFM

Griffith's model captures the effect that a given pre-existing flaw, described by its size a, has in the strength of a material. On the other hand, both the energetic and the stress intensity approach to fracture are based on an idealized representation of cracks as sharp geometric entities, either one dimensional, for 2D bodies, or two dimensional, for 3D bodies. A stress singularity thus arises in the vicinity of the crack front. The assumptions that led to the analytical treatment of fracture have

also led to some limitations and difficulties associated with developing numerical models.

The main weaknesses of traditional LEFM are the following:

- Strength predictions are based on a relation of the type $\sigma_r \propto (\sqrt{a})^{-1}$ which leads to infinite strength for uncracked bodies, meaning that the theory is unable to predict crack initiation.
- Inadequacy for predicting the direction of crack propagation [6], crack jumps, and crack branching or merging.
- The existence of a stress singularity at the vicinity of the crack tip poses significant issues to numerical analysis.

Furthermore, several difficulties arise from the finite element discretization of LEFM/NLFM:

- A conforming mesh topology is necessary to represent the propagating crack [7].
- Special finite elements at the crack tip are required since typical quadratic or three nodes elements based on polynomial interpolation functions are unable to reproduce the stress singularity [8].
- Tracking crack paths is a challenging task, often requiring either *ad hoc* crack path determination algorithms [9] or predetermined paths [10, 11].
- Crack path, maximum strength, and local stress state at the vicinity of the crack tip are highly dependent on mesh size.

Different techniques have been proposed to tackle some of these problems individually: remeshing algorithms can be used to adjust the mesh to the crack evolution; by discretizing the crack tip using quarter-point elements the stress singularity is obtained; opting for different methods, such as the virtual crack closure technique or path independent integrals has proven to be effective for predicting crack paths [7].

Within the scope of the FEM, methods used to model crack propagation are usually divided into two groups considering the treatment of cracks: discrete and diffuse (or continuum based) methods [6, 9, 10, 12]. Discrete methods, such as cohesive surfaces, hybrid discrete/finite elements, node splitting, element deletion, embedded finite element (E-FEM), or extended finite element (X-FEM) use a combination of the FEM and a LEFM/NLFM model to predict fracture involving discontinuities in the displacement field [6]. Diffuse crack models introduce a variable that determines the extent of fracture [6] and degrades the stiffness of the material. This type of model refers to continuum damage mechanics (CDM) and variational models for fracture, such as the PF model, that will be used in this work.

2.2.1 Diffuse models

The modeling of fracture by means of diffuse models is achieved without actually introducing a geometric crack into a structure. A displacement discontinuity

no longer exists, and cracks are never explicitly represented [7]. This is made possible by introducing the concept of material degradation modeled by an additional variable that substitutes the existence of a geometric crack. In reality, this approach encompasses a broader set of fracture mechanics problems, as the existence of any type of flaw (such as a void) can be studied by using some sort of degradation. An advancing crack front (or the growth of a flaw) is replaced by the evolution of a damage variable across the solid domain throughout the loading history. Some fundamental advantages arise from this strategy to describe fracture: the concept of a preexisting crack can still exist (introduced by different strategies, commonly by specifying an appropriate value for the damage variable considered) but is no longer required since, in terms of model behavior, no fundamental difference exists between an uncracked and cracked domain. Furthermore, predicting the crack path and occurrence of phenomena, such as crack bridging, deflection after impinging on a surface, or crack merging, naturally arises from the evolution of the variable according to a set of criteria [13]. This criteria can either result from a mechanical or thermodynamical approach and corresponds to the fundamental distinction between different diffuse models for fracture. Recently, PF models have been regarded as damage like models due to their strong similarities, which will be addressed in section 2.10. For this reason, the variable controlling fracture in diffuse crack models, and PF models in particular, may be seen as a damage variable with no loss of generality. Furthermore, its effect on material degradation and evolution can be regarded as the damaged state and damage progression over a solid domain, respectively.

2.2.2 Remarks on continuum damage models

Within the scope of CDM models, micro-defects are treated as continuous regions where CDM laws apply. It can be understood as a distinct approach from fracture mechanics since individual defects are lumped together and no discontinuities are considered [14]. CDM enables the study of the growth of micro-cracks by considering their effect on the mechanical behavior of a material [15] provided that all relevant phenomena and physically sound constitutive models are considered. Since these models refer to a larger scale than the scale at which the individual defects occur, a representative volume element (RVE) over which all properties are homogenized [15] must be considered, linking damage evolution to the averaged stiffness degradation occurring within the RVE. Furthermore, it is established a correspondence between the (real) damaged material, for which a Cauchy stress tensor may be defined, and a fictitious undamaged material, for which an effective stress tensor is defined in terms of the damage variable(s), taking into account that the mechanical behavior of both materials must be equivalent. Fig.2.1 exhibits the damaged and effective configurations, the former including an illustration of an RVE. To capture the most general case of damage evolution the damage field is often described by a second-, or even, fourth-rank tensor. A much simpler isotropic damage model employs two scalar damage variables defined in terms of the cross-sectional area in the damaged material, A, and in the fictitious configuration, $\bar{A}$,

$$\phi_1 = \frac{A - \bar{A}}{A}, \quad 0 \geq \phi_1 \leq 1 \tag{2.3}$$

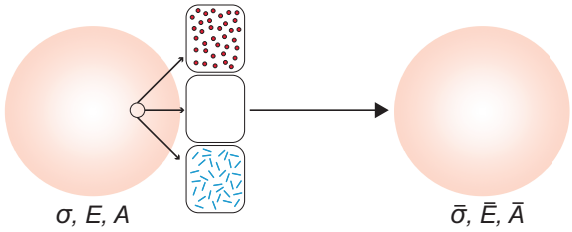


Figure 2.1: (left) Damaged and (right) effective configurations considered in damage models

and, considering that the same load is applied to both configurations,

$$\bar{\sigma} = \frac{\sigma}{1 - \phi_1}. \tag{2.4}$$

Thus, the effective stress varies between the value of stress in the damaged configuration ($\phi_1 = 0$) and tends to infinite values as the effective area is reduced ($\phi_1 = 1$). A reduction in the elastic modulus of the damaged material is governed by the second damage variable l_1,

$$l_1 = \frac{\bar{E} - E}{E}. \tag{2.5}$$

For an undamaged material, $l_1 = 0$ and $E = \bar{E}$, while $E \leq \bar{E}$ for increasing values of l_1. To establish a relation between both scalar variables, a constitutive equation must be postulated. Under the hypothesis of strain energy equivalence [14]:

$$\frac{\sigma^2}{2E} = \frac{\bar{\sigma^2}}{2\bar{E}} \tag{2.6}$$

a mathematical relation between the damage variables is found. The interaction between damage evolution and the strain and stress fields can be modeled using two methods: uncoupled and fully coupled approaches [16]. While using the former, we first solve for the strain and stress fields and then determine damage evolution; the latter approach consists in introducing damage evolution in the constitutive equations of the problem, solving for all fields at once.

Anisotropic damage models

The existence of material heterogeneity or anisotropic nature, or simply anisotropic damage progression renders the task of choosing adequate damage variables one of the most challenging steps in the development of damage models [17]. Moreover, damages models are of phenomenological nature and require some postulate forms for the description of damage evolution, encompassing not only stiffness degradation but also more complex phenomena, such as plastic deformation. For instance, Cauvin [17] defines, for an isotropic material, a set of damage variables relating effective properties to the elastic properties of the virgin material,

$$\bar{E} = (1 - D_E)\, E, \quad \bar{G} = (1 - D_G)\, G, \quad \bar{K} = (1 - D_K)\, K, \quad \bar{\nu} = (1 - D_v)\, \nu \tag{2.7}$$

where it is clear that, in spite of the material isotropy, damage evolution may be anisotropic with respect to the material properties considered, E, G, K, and ν -

Young's modulus, shear modulus, bulk modulus, and Poisson's ratio, respectively - thus requiring a set of distinct damage variables, D_i. A loss of material symmetry will, thus, determine the interdependency of the above listed damage variables. Considering a functional dependency of a fourth-rank tensor $\bar{\mathbf{E}}$ similar to the one shown in Eq.2.5, the most general damage tensor must be an eighth-rank tensor. If a linear relation between pristine and damaged configurations is assumed, then [17]

$$\bar{\mathbf{E}} = (\mathbf{I_8} - \mathbf{D_8}) :: \mathbf{E}. \tag{2.8}$$

However, by considering the principle of strain equivalence that imposes equivalence between the effective and actual strain, damage is described by a fourth-rank tensor. Clearly, by extending the concept of 1D damage, governed by the scalar variables ϕ_1 and l_1, the physically sound interpretation of damage as progressive loss of area leading to stiffness degradation ceases to exist.

Thermodynamic framework for damage evolution

One of the most important strategies to develop damage evolution laws is to consider the thermodynamic evolution of the material or structure considered. Thermal elastic, thermal elasto-plastic, thermal electrochemical elasto-plastic (among other) damage material behavior may be modeled by postulating a Helmholtz free energy density function Ψ written as a function of *(1)* dependent constitutive variables (implicitly), *(2)* field variables, and *(3)* phenomenological state variables [18]. For a thermal elastic damage material behavior:

$$\Psi = \tilde{\Psi}\left(\varepsilon_{ij}, T, \nabla_i T, N_k\right) \tag{2.9}$$

where Ψ is a function of the elastic strain tensor ε_{ij}, temperature T and temperature gradient $\nabla_i T$, and a set of k internal state variables N_k. These variables are of either scalar or tensorial nature and are a function of damage hardening internal state variables [18]. On the other hand, the equations governing the evolution of all state variables can be obtained by the balance laws - conservation of mass, linear and angular momentum - and the first and second laws of thermodynamics.

Continuum damage model for composite structures

Historically, composite materials have been one of the main drivers for the development of continuum damage mechanics. This fact stems from their quasi-brittle failure behavior. There is arguably no other failure type more appropriately designated by the word *Damage*, considering that several failure mechanism occurring at different length scales progressively degrade the stiffness of the material or structure. Studying the accumulation of damage prior to structural collapse is paramount to understand the damage tolerance of a structure [19]. To develop continuum damage models for fiber reinforced polymer (FRP) composites the nature and morphology of the material must be taken into consideration. By doing so, the generic fourth-order damage tensor obtained by considering the strain equivalence in Eq. 2.8 is no longer required, and a set of scalar damage variables may be associated to preferred directions for crack growth [19]. For instance, Maimí et al. [19, 20] developed a

constitutive damage model (hence, fully coupled) for laminated FRPs based on the thermodynamics of irreversible processes. Instead of using computationally expensive fourth-rank damage tensors, such as seen in many reference models in the field of CDM (see, for example, [14, 21, 22]), a set of scalar damage variables was defined, each linked to a specific experimentally observable damage mechanism. There are two major advantages associated with this modeling approach: damage evolution is based on physically sound evidence, instead of potentially fitting parameters related with some abstract tensor representation of damage; subsequent model implementation in numerical frameworks, such as a finite element framework, potentially leads to a less computationally expensive damage computation. The obvious pitfall is the requirement of high constitutive modeling skill, as well as a not so obvious definition of all the relevant damage mechanisms occurring at the modeled length scale. The ply-scale model relies on the definition of a complementary free energy density G that takes into account the effect of temperature and moisture:[19]

$$\begin{aligned} G =& \frac{\sigma_{11}^2}{2\left(1-\mathrm{d}_1\right)E_1} + \frac{\sigma_{22}^2}{2\left(1-\mathrm{d}_2\right)E_2} - \frac{v_{12}}{E_1}\sigma_{11}\sigma_{22} \\ &+ \frac{\sigma_{12}^2}{2\left(1-\mathrm{d}_6\right)G_{12}} + \left(\alpha_{11}\sigma_{11} + \alpha_{22}\sigma_{22}\right)\Delta T \\ &+ \left(\beta_{11}\sigma_{11} + \beta_{22}\sigma_{22}\right)\Delta M \end{aligned} \tag{2.10}$$

where the subscripts *1* and *2* denote the fibre and matrix directions, respectively; E_i, G_{ij}, and ν_{ij} are in-plane elastic orthotropic properties of a composite lamina; α_{ij} are the coefficients of thermal expansion, and β_{ij} the coefficients of hygroscopic expansion. Here, the stress tensor corresponds to an averaged quantity over a RVE. The damage variables d_1, d_2 are linked to longitudinal fibre failure and transverse matrix cracking, while d_6 is related with longitudinal and transverse cracks. The compliance tensor of the RVE is then obtained by evoking the second law of thermodynamics, i.e., the irreversibility of the damage process,

$$\dot{G} - \dot{\sigma} : \varepsilon \geq 0 \tag{2.11}$$

and by evaluating the total time derivative of the complementary free energy density:

$$\left(\frac{\partial G}{\partial \sigma} - \varepsilon\right) : \dot{\sigma} + \frac{\partial G}{\partial d_1}\dot{d_1} + \frac{\partial G}{\partial \mathrm{d}_2}\dot{d_2} + \frac{\partial G}{\partial d_6}\dot{d_6} \geq 0. \tag{2.12}$$

The arbitrariness of the time variance of the stress tensor imposes a null value on the first term on the left hand side of Eq. 2.12,

$$\varepsilon = \frac{\partial G}{\partial \sigma} = \mathbf{H} : \sigma + \alpha \Delta T + \beta \Delta M \tag{2.13}$$

Substituting in Eq.2.13 the expression for G presented in Eq.2.10, the compliance tensor $\mathbf{H}$ is thus obtained as a function of the elastic constants and set of damage variables,

$$\mathbf{H} = \frac{\partial^2 G}{\partial \sigma^2} = \begin{bmatrix} \frac{1}{(1-d_1)E_1} & -\frac{v_{21}}{E_2} & 0 \\ -\frac{v_{12}}{E_1} & \frac{1}{(1-\mathrm{d}_2)E_2} & 0 \\ 0 & 0 & \frac{1}{(1-\mathrm{d}_6)G_{12}} \end{bmatrix}. \tag{2.14}$$

Additionally, a distinction must be made between the damaged state caused by tension and compression loads to take into account the crack closure effect. Depending

on the sign of the stress tensor components, either the positive or negative damage variable must be active,

$$\begin{aligned} \mathrm{d}_1 &= \mathrm{d}_{1+}\frac{\langle\sigma_{11}\rangle}{|\sigma_{11}|} + \mathrm{d}_{1-}\frac{\langle-\sigma_{11}\rangle}{|\sigma_{11}|} \\ \mathrm{d}_2 &= \mathrm{d}_{2+}\frac{\langle\sigma_{22}\rangle}{|\sigma_{22}|} + \mathrm{d}_{2-}\frac{\langle-\sigma_{22}\rangle}{|\sigma_{22}|} \end{aligned} \tag{2.15}$$

where the McCauley operator is defined as $\langle x\rangle := (x+|x|)/2$. A key input ingredient for a constitutive damage model is the set of failure criteria considered. In the work published by Maimí et al [19, 20] the LaRC04 criteria developed for intralaminar failure [23] were used - failure criteria for (1) tensile and (2) compressive failure of fibres, and (3) tensile and (4) compressive failure of the polymer matrix, also taking into account the interaction between stress components - as damage activation functions. Hence, four damage activation functions, F_N, and four elastic domain (or undamaged domain) thresholds, r_N [19] were defined. The latter are related to the damage variables by damage evolution laws by means of monotonously increasing functions. The loading history is stored in loading functions, ϕ_N that depend on the stress field and strength properties. This set of functions are related by a set of inequalities

$$F_N = \phi_N - r_N \leq 0\ , \quad N = \{1_+,\ 1_-,\ 2_+,\ 2_-\} \tag{2.16}$$

which, taking into account that $\dot{d}_i \geq 0$ subsequently lead to the following *Kuhn-Tucker conditions* [19]:

$$\dot{r}_N \geq 0; \quad F_N \leq 0; \quad \dot{r}_N F_N = 0. \tag{2.17}$$

These conditions ensure that from the moment that a certain loading function N increases to the point that its corresponding damage activation function verifies $F_N = 0$, further positive increments of ϕ_N lead to damage evolution, $\dot{r}_N > 0$.

Summary of continuum damage models

While the detailed description of damage models, and, in particular, of the damage model for advanced composites developed by Maimí et al. [19, 20] may seem to lie outside the scope of the present work, a clear understanding of the underlying principles and methodologies employed will prove of fundamental value to understand the *engineering adaptations* that several authors have made to phase-field models applied to brittle fracture. These can be better understood by regarding the *phase field approach to fracture* as yet another form of *a continuum damage mechanics approach to fracture.*

2.3 Brief introduction to the modeling of microstructures using the phase field approach

The study of microstructures in materials engineering is of paramount importance to understand the influence of a wide range of material properties. High-strength aluminum alloys owe their high strength value to a hardening mechanism called precipitation hardening, consisting in heterogeneous particles visible in their

microstructure. Carbon fibres used in advanced composites exhibit different young's modulus and strength based on their microstructure (giving rise to one of the most fundamental distinctions between carbon fibre types - high modulus, intermediate modulus, and high strength carbon fibres). The degradation of the microstructure of cathodes and anodes during charge/discharge electrochemical cycles is responsible for most of the failure mechanisms and performance lost of LIBs [5]. Moreover, stainless steel is a poor electricity and heat conductor due to its high content in alloy elements, which disrupt an otherwise regular iron lattice thus restricting movement of free electrons. Of obvious importance is the study of evolving microstructures in the kinetics of physical reactions such as the solidification process of a material. Many materials science models rely on such concepts as bulk free energy minimization, surface energy, and strain-induced transformation to explain the size, shape, and spatial arrangement of all these microstructural features [24, 25]. For instance, to model the kinetics of the solidification of a pure material, the mathematical description of the solidification front consists in a sharp interface model [25], known as the Stefan problem, for which the transient heat conduction equation and a flux boundary condition, applied to the solid-liquid interface, must be considered

$$\begin{aligned} \frac{\partial T}{\partial t} &= \nabla \cdot \left(\frac{k}{\varrho c_p} \nabla T \right) \equiv \nabla \cdot (\alpha \nabla T) \\ \varrho L_f V_{\mathrm{n}} &= k_{\mathrm{S}} \nabla T \cdot \vec{n}|_{\mathrm{int}}^{\mathrm{s}} - k_{\mathrm{L}} \nabla T \cdot \vec{n}|_{\mathrm{int}}^{\mathrm{L}} \end{aligned} \tag{2.18}$$

where subscripts/superscripts L and s denote the liquid and solid phases, respectively, k is the thermal conductivity, T denotes the temperature, ρ the mass density, α the thermal expansion coefficient, c_p the specific heat at constant pressure, and V_n is the normal velocity of the interface normal to vector $\vec{n}$, and L_f is the latent heat of fusion for solidification. An additional equation is required to incorporate the Gibbs-Thomson condition that correct the curvature of the temperature at the interface [25],

$$T_{\mathrm{int}} = T_{\mathrm{m}} - \left(\frac{\gamma T_{\mathrm{M}}}{L_{\mathrm{f}}} \right) \kappa - \frac{V_{\mathrm{n}}}{\mu} \tag{2.19}$$

where γ is the solid-liquid surface energy, T_M the melting temperature, κ the interface curvature, and μ the local atomic interface mobility. While the exact derivation of the equation above lies outside the scope of the present discussion, it represents the volumetric tendency for solidification to progress (bulk energy minimization) and the surface tendency to arrest interface evolution [26]. Because Sharp interface models are developed for larger length scales than the interface width, terms such as the flux boundary condition in Eqs. 2.18 and the Gibbs-Thomson condition need to be incorporated. Two major issues prevent a wider spread use of sharp interface models [25]: it is not usually easy to define an exact model for more complex problems and numerical solutions are difficult to obtain. Moreover, for these free boundary problems, such as the growth of a participate, the position of the interface depends on the solution of a diffusion equation which, in turn, depends on the position itself [27]. Phase field models are a class of relatively recent numerical models that generally consist in re-interpreting sharp interface free boundary problems using a continuum approach. Besides the physical field we intend to solve - temperature, mass concentration, displacement, chemical potential, or others - an additional continuum field called *phase field* or *order parameter* is introduced [25].

Its extreme values, typically 0 and 1, identify with the two phases to be distinguished; the position of the interface is modeled by a continuous change in value of the phase field variable(s) [28]. Consequently, it is only possible to model diffuse interfaces, although by setting its length scale parameter the solution of phase field models must converge to the one given by a sharp interface model. One of its most interesting features for the field of materials science is the capacity to predict the evolution of complex morphologies with no need to keep track of the position of the interface [28]. The same type of difficulty was mentioned in section 2.2 for keeping track of the crack path. The equations governing the field's evolution are traditionally established by a phenomenological free energy functional [25]. The fact that free energy functionals may be defined for various physical phenomena has lead to the successful development of phase field models for numerous application including fracture and damage mechanics models.

Phase field evolution equations

There are three types of field variables used in phase field modeling which can be divided in two groups [28]: conserved variables, usually identified as c_i, that keep track of some composition and must be employed when interpolation is made between two phases obeying a conservation law; and nonconserved field variables. There are two types of nonconserved variables - phase fields, ϕ_i, and order parameters, η_i[1] [24]. An obvious example for the use of conserved variables is the case of modeling interfaces in chemical/physical reactions, for which the concentration fractions c_i for a binary system of phases *1* and *2* must obey the relation

$$c_1{+}_2 = 1. \tag{2.20}$$

Since the problem of fracture deals with a geometric interface between two phases (uncracked phase and cracked phase) that do not obey to such conservation law, nonconserved fields can be used to model cracking phenomena. Moreover, while a rigorous distinction between field variables is paramount in problems such as phase transformation since the three are simultaneously present, for fracture models *order parameter* and *phase field* are terms used interchangeably, and their meaning need not to follow the original definition. For nonconserved actions, the evolution of the field variable is governed by the Allen-Cahn equation (valid for static or quasi-static problems) or the time-dependent Ginzburg-Landau equation [24]. For a binary system, we obtain the expression

$$\dot{\eta} = -L\frac{\delta F}{\delta \eta\,(\mathbf{x}, t)} \tag{2.21}$$

for the Ginzburg-Landau equation, where L is the mobility associated with η, and F is the free energy defined for the bulk system. Cahn and Hilliard assumed that for conserved problems the free energy must depend on local and nonlocal composition (conserved order parameter) and developed an expression for F containing a bulk term and gradient terms, $F = F(c, \nabla c, \nabla^2 c, ...)$ [24]. For problems described by order parameters, the same rational was employed to obtain $F = F(\eta)$, the so-called

[1] In phase field models for brittle and ductile fracture, the nomenclature established to distinguish between these types of field variables is occasionally not followed

Landau free energy function (usually a fourth-order or sixth-order polynomial). An entire different class of phase field models is only concerned with a phase-field ϕ used to make a distinction between two coexisting phases, such as solidification problems. In their review article on phase field models, Moelans et al. [28] classify this as *more phenomenologically oriented phase-field models*. Furthermore, if no conserved variables are of interest, the bulk free energy is defined as

$$F = \int_V \left[f_0 \left(\mathbf{x}, \phi, \mathbf{v} \right) + \frac{\kappa}{2} (\nabla \phi)^2 \right] \mathrm{d}\mathbf{x} \tag{2.22}$$

with f_0 the homogeneous free energy density functional, and $\mathbf{v}$ a given set of fields of relevance for the problem (displacement, temperature, chemical potential, etc), and κ a (positive) gradient energy coefficient, which are energetically unfavorable [28]. Moreover, expressions for $f_0 = f_0(\phi, \mathbf{v})$ result from interpolating values of free energies for each phase α and β

$$f_0 \left(\phi, \mathbf{v} \right) = (1 - h(\phi)) f_0^{\alpha} \left(\phi, \mathbf{v} \right) + h(\phi) f_0^{\beta} \left(\phi, \mathbf{v} \right) \tag{2.23}$$

where the interpolation function $h(\phi)$ is a smooth function equal to 1 for ϕ=1 and equal to 0 for $\phi = 0$ and possesses local extrema at both points. Under these conditions, the Allen-Cahn equation for single phase-field problems is [28]:

$$\begin{aligned} \frac{\partial \phi(\mathbf{x}, t)}{\partial t} &= -L \frac{\delta F \left(\phi \right)}{\delta \phi(\mathbf{x}, t)} \\ &= -L \left[\frac{\partial f_0 \left(\phi \right)}{\partial \phi} - \nabla \cdot \kappa(\phi) \nabla \phi \right]. \end{aligned} \tag{2.24}$$

From Eq.2.24, it is seen that the time evolution of the phase field is governed by a partial differential equation involving the positive term concerned with minimization of the free energy density and a negative surface energy term. In practice, the latter penalizes the growth of a phase β in a similar way to the Gibbs-Thomson condition seen in Eq.2.19. It is thus seen that all single phase field models with no conserved action are governed by the same evolution law, for which three specific quantities must be defined: the free energy density functional f_0, the parameter influencing the kinetics of phase growth, mobility L, and the positive gradient energy coefficient κ.

2.4 The variational approach to fracture. Phase field models for brittle fracture

The variational model for fracture was first proposed by Francfort and Marigo in 1998 [29] and largely developed by the PhD dissertation work from Bourdin [30] published in the same year. It falls within the scope of diffuse damage models by *revisiting brittle fracture as an energy minimization problem*, as the title of the original work suggests. While Griffith invoked the principle of minimum total potential energy with respect to crack growth, with the so-called variational approach it is presupposed that the minimization refers to global (not local, pre-crack associated) energy [29]. Eq. 2.1, that states the original law as a minimization problem for an already cracked geometry is substituted by a variational statement, a postulate much

like those commonly found in damage models, extended to the whole domain [29]. Considering also that fracture is an evolving phenomenon for which no reversibility of an existing crack geometry can be observed, a certain notion of time [2] must be incorporated in the formulation. Consequently, a *quasi-static* process is assumed [30], and the system attains an equilibrium state at each instant (step), i. The total energy $E(\mathbf{u}, \Gamma_i)$, a function of the displacement field, $\mathbf{u_i}$, and crack surface, Γ_i, at each instant t_i ($t_i > t_{i-1}$) is obtained via an energy minimization criterion,

$$E(\mathbf{u}, \Gamma_i) = \inf_{\substack{\Gamma \in F_A \\ \Gamma \supset \Gamma_{i-1}}} \inf_{\mathbf{u} \in V_u} E(\mathbf{u}, \Gamma), \tag{2.25}$$

where irreversibility is enforced by guaranteeing that $\Gamma \supset \Gamma_{i-1}$, and the total energy $E(u, \Gamma)$ is defined as a sum between bulk and surface energies,

$$E(\mathbf{u}, \Gamma) = E^{\Omega}(\mathbf{u}, \Gamma) + E^{\Gamma}(\Gamma) - \int_{\partial\Omega_N} \bar{\mathbf{t}}\mathbf{u} d\partial\Omega_N. \tag{2.26}$$

The scope of Eq. 2.25 extends that of crack growth, which means that the initial constraints and limitations of Griffith's model disappear: crack initiation, propagation, branching, or other cracking phenomena are natural consequences of the minimization procedure. Therefore, it allows to robustly model fracture for brittle materials capturing complex crack topologies in 3-D solids [13].

At any admissible state, the bulk energy depends on the displacement field and the crack surface. It is given by the strain energy stored within the domain Ω, naturally taking into account the release of elastic energy associated with the evolution of a crack. The same sort of dependency is observed in Griffith's law. However, it is now explicitly defined as a global measure for a potentially cracked body, also defined for non-cracked geometries,

$$E^{\Omega}(\mathbf{u}, \Gamma) = \int_{\Omega/\Gamma} \Psi(\varepsilon(\mathbf{x}))\, d\mathbf{x}. \tag{2.27}$$

In case a pristine geometry is considered, the integral defined in Eq. 2.27 is simply extended to the whole domain. The surface energy term depends on the extent of cracking that has occurred at any given step as well as the toughness of the material considered. For a heterogeneous material, it can be defined as

$$E^{\Gamma}(\Gamma, \mathbf{x}) = \int_{\Gamma} \mathcal{G}_c(\mathbf{x}, \mathbf{n}(\mathbf{x}))\, d\mathcal{H}^{n-1}(\mathbf{x}), \tag{2.28}$$

where $\mathcal{H}^{n-1}$ represents the Hausdorff measure of the crack surfaces, n is the dimension of the domain Ω considered, and $\mathbf{n}$ is the normal to Γ at $\mathbf{x}$. It is now possible to mathematically define the space of admissible value for Γ:

$$F_A = \left\{ \Gamma \subset \bar{\Omega}; \mathcal{H}^{n-1}(\Gamma) < +\infty \right\}, \tag{2.29}$$

where $\bar{\Omega}$ is the complete domain of dimension $n-1$ where cracking may occur, obtained from Ω. Even though the variational statement 2.25 can provide analytical

[2] This notion of *time* does not imply a relation to a quantifiable passage of time. Instead, the influence of *time* is understood simply as imposing an irreversibility condition, an *arrow* indicating a relation between pristine and cracked conditions.

solutions for simple models, the minimization problem leads to significant algorithmic problems due to the complexity of determining the optimal crack geometry at each time t_i [31]. To achieve an expression better suited for numerical analysis based on weak formulations a new functional must be obtained. The solution was found within the context of image segmentation (credited to [32]) and consists in defining an additional field, c, for the functional that governs the evolution of the crack thus replacing the actual crack surface Γ. Since both energy terms defined in Eq. 2.25 depend explicitly on Γ, these must be redefined as a function of the field c. The regularized functionals thus obtained assume the form [33]

$$E(\mathbf{u}, c) = \int_\Omega f(c)\Psi(\varepsilon)d\mathbf{x} + \frac{\mathcal{G}_c}{c_w\, l} \int_\Omega w(c) + l^2|\nabla c|^2 d\mathbf{x} - \int_{\partial\Omega_N} \bar{\mathbf{t}} \cdot \mathbf{u} \tag{2.30}$$

where the function $f(c)$ degrades the strain energy according to the evolution of c, $w(c)$ defines the decaying profile of c [33], and c_w is a normalization constant determined as to guarantee the so-called Γ-convergence of the second term in expression 2.30, i.e., its value ensures that the term converges to E^Γ as defined in 2.28, $c_w = \int_0^1 \sqrt{w(t)}dt$. Comparing with the former expression for E^Γ, the definition of E presented in Eq. 2.30 allows us to interpret the term $\frac{\mathcal{G}_c}{c_w\, l}$ as a volumetric fracture toughness, equivalent to the actual fracture toughness $\mathcal{G}_c$, but with respect to energy released per unit volume. Clearly, the fact that the Hausdorff measure of the fracture surface ($n-1$ dimension) is replaced by an integral extended over the bulk (n dimension), and taking into account that $w(c)$ is a non-dimensional function, the analogy between 2.28 and 2.30 allows this interpretation.[3]

2.4.1 Regularized form of the fracture functional

The conversion of the original crack integral term to a new integral extended to the whole bulk domain was achieved by incorporating the c-field and by defining a new function $f(c)$ that allows for suitable numerical implementations without the need to keep track of the fracture interface; this is exactly the same key feature that has made PF models so attractive in the material science world and enables robust numerical implementations. The fracture energy term depends explicitly not only on c but also on its gradient, ∇c. Additionally, a length scale parameter, l, must be defined in order to control the smearing out of the original crack. In purely geometric terms the crack regularization consists in approximating the exact crack, Γ, by a diffused (or smeared) representation, usually mathematically described by a crack surface density γ,

$$\int_\Gamma dS \approx \int_\Omega \gamma dV. \tag{2.31}$$

The following conditions are usually imposed to determine γ:

- Γ-convergence must be ensured, i.e., Eq. 2.31 must tend to an equality for decreasing values of l.
- Its value over the domain is determined by c.

[3] Some authors prefer to write the fracture energy term of the functional as $\mathcal{G}_]/c_w \int_\Omega w(c)/l + l|\nabla c|^2 d\mathbf{x}$. This equivalent expression leads to a $n-1$ dimension of the integral, providing an alternative interpretation of the regularized functional term.

- The dependence $\gamma = \gamma(c, \nabla c)$ takes into account not only the local character, but also non-local effects associated with the progression of c. This characteristic can also be observed in CDM models.

The function $w(c)$ must be continuous and increase monotonously with an evolving crack field, c. Assuming for subsequent expressions that $c = 0$ and $c = 1$ for pristine and fully broken states, respectively, then $w(0) = 0$, and $w^{'}(c) \geq 0$ for $c \in [0, 1]$. Furthermore, we choose $w(c)$ such that $w(1) = 1$. The most widely used functions are credited to Ambrosio and Tortorelli [32], and the choices are $w(c) = c$ (linear model, also called AT-1), and $w(c) = c^2$ (second order quadratic approximation, At-2 model). These expressions determine c_w such that $c_w = 8/3$ and $c_w = 2$, respectively. Table 2.1 summarizes the previous expressions for both models.

Table 2.1: Fracture functional parameters for the linear and quadratic models

Parameter	AT-1 (linear) model	AT-2 (quadratic) model
$w(c)$	c	c^2
c_w	8/3	1/2

Smeared crack surface. The crack surface density function

The adequacy of a second order approximation for the crack surface density can be inferred from a cracked 1D body such as an infinitely long bar, as demonstrated by Miehe et al. [34]. Consider a bar with cross-section A and length L defining a domain $\omega = A \times L$, such that $L \gg A$. If a crack is fully developed at $x = 0$, its sharp topology may be described by a c field using the Dirac delta function [35],

$$c(x) = \delta(x) = \begin{cases} 1 & \text{for } x = 0 \\ 0 & \text{otherwise} \end{cases} . \tag{2.32}$$

This crack representation corresponds to a sharp crack interface. To obtain a smooth or diffused crack topology, c must be approximated by a smooth function of x which is accomplished by considering an exponential function

$$c(x) = e^{-|x|/l}, \tag{2.33}$$

where the extent of smearing can be controlled by and is proportional to the parameter l [4]. For finite values of l, the exponential function 2.33 has the property [34]

$$c(0) = 1 \quad \text{and} \quad c(\pm\infty) = 0. \tag{2.34}$$

Furthermore, expression 2.33 is the solution of the following differential equation:

$$c(x) - l^2 c''(x) = 0 \quad \text{in} \quad \Omega \tag{2.35}$$

[4] $\lim_{l \to 0} \exp -|x|/l = 0$ and $e^{-0/l} = 1$ regardless of the value of l

subject to the Dirichlet boundary conditions in 2.34. Eq. 2.35 may be obtained by considering the functional [36]

$$I(c) = \frac{1}{2}\int_{\omega} \left\{ c^2 + l^2 c'^2 \right\} dV \tag{2.36}$$

and its minimization by variational principles,

$$c = \mathrm{Arg}\left\{ \inf_{c \in W} I(c) \right\}. \tag{2.37}$$

The concept of Γ-convergence is easily explained by considering that Γ assumes the value of A and dV=Γdx in Eq. 2.36 and evaluating the integral with the solution given by Eq. 2.33

$$I(c) = \frac{1}{2}\int_{-\infty}^{+\infty} \left(e^{|x|/l}\right)^2 - \left(e^{-|x|/l}\right)^2 dV = l\Gamma \tag{2.38}$$

.

Proof

Considering that the solid $\mathcal{B}$ possesses a cross section coincident with the crack surface, Γ, and its length extends over an infinite domain, L=[-∞,+∞], substituting for c in expression 2.36 with expression 2.33

$$\begin{aligned} & \frac{1}{2}\int_{-\infty}^{+\infty} e^{-2|x|/l} + l^2 \cdot \left(\frac{e^{-2|x|/l}}{l^2}\right)\Gamma dx \\ I(c) = & = \Gamma \cdot \frac{1}{2}\int_{-\infty}^{+\infty} 2e^{-2|x|/l} dx \\ & = \Gamma \cdot 2 \cdot \int_{0}^{+\infty} e^{-2|x|/l} dx \\ & = \Gamma \cdot l \end{aligned} \tag{2.39}$$

From the result in Eq. 2.38, we can define the (smeared) crack surface in terms of the functional [36]

$$\Gamma_l(c) := \frac{1}{l} I(c) = \frac{1}{2l}\int_{\Omega} \left\{ c^2 + l^2 c'^2 \right\} dV. \tag{2.40}$$

The extension of the mathematical relations above to a multi-dimensional solid lead to the definition of the crack surface density function as

$$\gamma(c, \nabla c) = \frac{1}{2l}c^2 + \frac{l}{2}|\nabla c|^2 \tag{2.41}$$

which coincides with the expression found for the AT-2 model. Thus, it is seen that an expression for γ_l can be motivated by either a *prescribed shape of the regularization of sharp cracks* [37], as just described, or Γ-*convergence regularization* for constructing elliptical functionals, as was originally done by Ambrosio, Tortorelli et al. [32]. Although both can lead to the same functional, these are still distinct approaches, leading to a clear distinction between what is called in the literature

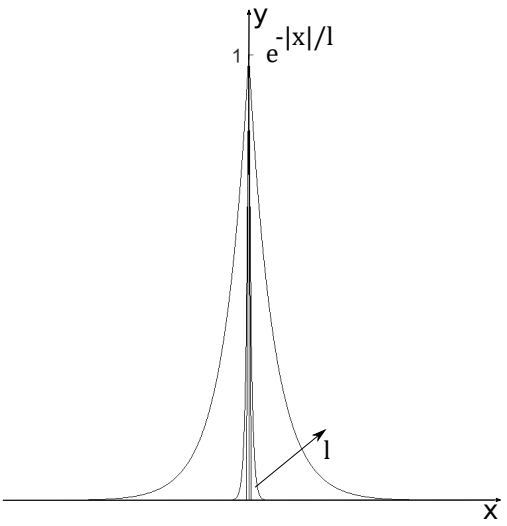


Figure 2.2: Diffuse 1-D crack topology for distinct values of the length scale parameter l

the mathematical and engineering variational approaches to fracture [11]. Another important feature found in the general expression for γ,

$$\gamma(c, \nabla c) := \frac{\alpha(c)}{l} + l|\nabla c|^2 \tag{2.42}$$

is that it contains a local term $\frac{\alpha(c)}{l}$, explicitly depending on the length scale and the c variable. Furthermore, the term $l|\nabla c|^2$ is regarded as a non-local term due to the explicit dependency on the gradient of the c variable [38].

2.4.2 Influence of the length scale parameter l on diffuse crack topology

While the spatial configuration of cracks in a domain Ω is governed by the c field, the decaying profile, i.e., the topology of a smooth crack described by γ_l, is completely controlled by the length scale parameter l. In Fig.2.2, the effect of varying l in the crack surface density function is illustrated for the same 1D infinitely long bar as considered before. It is clearly seen that l must be small enough to achieve accurate topological representations of the actual sharp crack. On the other hand, a change in the diffuse description of the crack also leads to changes in the diffuse damaged areas thus affecting the energy released during crack propagation which affects the mechanical response.

2.5 Strain energy degradation

Another function required to introduce the c field in the variational statement is the degradation function $f(c)$ that maps a spatial configuration of c into a degraded

spatial configuration of bulk (free) energy obeying the following set of conditions:

$$\begin{array}{c} f'(c) < 0 \\ f(0) = 1 \quad \& \quad f(1) = 0 \ . \end{array} \tag{2.43}$$

Since the strain energy density of a cracked phase is always null, $f(c)$ may be regarded as an interpolation function between elastic energy values of damaged and undamaged zones. A quadratic expression for $f(c)$ is typically assumed by several authors ([33, 39, 40] among others) for both AT-1 and AT-2 models,

$$f(c) = (1-c)^2 \, . \tag{2.44}$$

Alternatives to the quadratic expression have been provided in [41], namely, a cubic degradation function that increases the linearity of stress-strain responses before softening occurs. A more comprehensive study by Wu [42] provides further insight into its effect on the softening law. Considering a generic polynomial expression

$$f(c) := \frac{1}{1+\phi(c)} = \frac{(1-c)^p}{(1-c)^p + Q(c)} \tag{2.45}$$

where the coefficients of polynomials $Q(c)$ and $P(c)$ were calibrated from standard material properties. A cubic expression was considered for various numerical applications.

Elastic Energy Decomposition

An energy decomposition is necessary to accurately predict anisotropic fracture behavior with respect to tension and compression [43] and is also required to model crack closure upon load reversal [34]. Another physically inconsistent feature of isotropic models is the existence of interpenetration of crack lips upon crack closure, leading to a force-displacement curve such as depicted in Fig. 2.3 for the isotropic model. The strain energy density, integrand function of the first integral in Eq.2.30 is divided into (degraded) positive and negative components. Assuming an independent behavior of the latter with respect to c, that is, $\Psi^+ = \Psi^+(\varepsilon, c)$, and $\Psi^- = \Psi^-(\varepsilon)$,

$$\begin{aligned} \Psi(\varepsilon, c) &= \Psi^+(\varepsilon, c) + \Psi^-(\varepsilon) \\ &= f(c)\Psi^+(\varepsilon) + \Psi^-(\varepsilon) \, . \end{aligned} \tag{2.46}$$

Choosing an appropriate split for expression 2.46 is a challenging task that significantly influences the accuracy of cracking phenomena within a solid media and currently available options limit the physical soundness of some phenomena observed. After the first numerical approaches introduced to model asymmetric behavior during tension and compression, and a formulation by Lancioni and Carfagni [44] associating cracks to mode-II loading, Amor et al [45] proposed a splitting of Ψ based on spherical and deviatoric parts. The fairly recent interest of the damage mechanics community in variational models of brittle fracture has led to the usage of a spectral decomposition of strain [46], as proposed for damage models in [47],

$$\begin{array}{l} \Psi^+(\varepsilon) = \frac{\lambda}{2}\left(\langle \mathrm{tr}[\varepsilon] \rangle_+\right)^2 + \mu \, \mathrm{tr}\left[\varepsilon_+^2\right] \\ \Psi^-(\varepsilon) = \frac{\lambda}{2}\left(\langle \mathrm{tr}[\varepsilon] \rangle_-\right)^2 + \mu \, \mathrm{tr}\left[\varepsilon_-^2\right] \end{array} \tag{2.47}$$

where μ and λ are Lamé constants, $tr[]$ denotes the trace of the strain tensor matrix, and the spectral decomposition of the strain is given by

$$\varepsilon^{\pm} = \sum_{i=1}^{n} \langle \varepsilon_i \rangle^{\pm} \cdot \boldsymbol{N}_i^{\varepsilon} \otimes \boldsymbol{N}_i^{\varepsilon}. \tag{2.48}$$

A more generic expression for considering the decomposition of bulk free energies in problems involving other fields is obtained by considering a split of the Helmholtz free-energy into ***pas**sive* and ***act**ive* components

$$\Psi(\boldsymbol{\varepsilon}, c) = f(c)\Psi^{\text{act}}(\boldsymbol{\varepsilon}) + \Psi^{\text{pas}}(\boldsymbol{\varepsilon}). \tag{2.49}$$

This definition is valid regardless of the actual Helmholtz free-energy and constitutive equations considered, providing a useful mathematical treatment for coupled-field problem, non-elastic materials, or even different types of strain tensors.

Degradation function expression for numerical implementation

The numerical treatment of a system of algebraic equations stemming from expression 2.30 requires a residual stiffness term in the expression of $f(c)$,

$$f(c) = (1-c)^2 \cdot (1-k) + k \tag{2.50}$$

Where k is the residual stiffness, necessary in order to prevent numerical problems associated with the rank of the stiffness matrix for a complete loss of stiffness, while simultaneously preventing that the resulting system of equations becomes ill-conditioned [39]. The numerical parameter should be the smallest number as possible for all the domain except the boundary of the solid because of the compactness property [38]. This residual stiffness typically assumes a value $\approx 10^{-6}$ [48]. Scenarios for which a tensile load, and its associated strain energy $\psi_0^+(\varepsilon)$, decreases with the evolution of time can still lead to unrealistic crack healing effects (typical examples are load reversal and cyclic loads). To overcome this issue different strategies have been proposed as follows.

2.5.1 Strategies to impose crack field irreversibility

Gerasimov and Lorenzis [33] have identified three main strategies to enforce the irreversibility of a fracture process:

- Definition of a crack-set within which, above a threshold value, irreversibility is explicitly imposed on the crack field.
- Definition of the so-called history field variable.
- Definition of a penalization term in the variational expression of Π.

'Crack-set' Irreversibility

First, a set CR_{n-1} is defined where, according to an assumed threshold value for c, *CRTOL*,

$$\text{CR}_{n-1} := \left\{ \mathbf{x} \in \bar{\Omega} : c_{n-1}(\mathbf{x}) \geq \text{CRTOL} \right\}. \tag{2.51}$$

Then, the value of the crack field is explicitly set as $c = 1$ for all $\mathbf{x} \in \mathrm{CR}_{n-1}$. The variational inequality δE that would be obtained from expression [5] 2.30 is replaced by an equality, and the following system of equations is obtained:

$$\begin{cases} E_{\mathbf{u}}\left(\mathbf{u}, c; \boldsymbol{v}\right) = 0, & \forall \boldsymbol{v} \in \mathbf{V}_0 \\ E_c\left(\mathbf{u}, c\right); \beta) = 0, & \forall \beta \in \left\{ H^1(\Omega) : \beta|_{\mathrm{CR}_{n-1}} = 0 \right\} \end{cases} \tag{2.52}$$

Where V is the space of admissible functions supporting the displacement field, $\boldsymbol{v}$ and β the test functions, and $H^1(\Omega)$ the Sobolev space (with Ω denoting the solid media).

History field irreversibility

The 'history field' approach is based on the assumption that the positive part of the free energy is the driving force of the phase-field evolution and, thus, considering its maximum local value throughout all loading steps will prevent crack self-healing

$$\mathcal{H}_n(\mathbf{x}) := \max_{n \geq 1} \left\{ \mathcal{H}_{n-1}(\mathbf{x}), \Psi^+(\boldsymbol{\varepsilon}(\boldsymbol{u})) \right\} \tag{2.53}$$

and the variational expression for the phase-field variable is modified, now expressed in terms of the history variable $\mathcal{H}$,

$$\widetilde{E}_c(\boldsymbol{u}, c; w) := \int_\Omega \left[\mathrm{g}'(c)\mathcal{H}_n\beta + \frac{G_c}{c_{\mathrm{W}}} \left(\frac{1}{\ell} \mathrm{w}(c)\beta + 2\ell \nabla c \cdot \nabla \beta \right) \right] \mathrm{d}\mathbf{x}, \tag{2.54}$$

leading to a system where both equations express an equality,

$$\begin{cases} E_{\boldsymbol{u}}(\boldsymbol{u}, c; \boldsymbol{v}) = 0, & \forall \boldsymbol{v} \in \mathbf{V}_0 \\ E_c(\boldsymbol{u}, c; \beta) = 0, & \forall \beta \in H^1(\Omega) \end{cases} \tag{2.55}$$

Gerasimov and Lorenzis [33] state that since this approach leads to loss of the variational character of 4.16 [6], no obvious equivalence between such expression and expression 2.55 exists, and lacks both theoretical and numerical proof. Furthermore, if a 2^{nd} order linear approximation is used, the additional constraint $c \geq 0$ is necessary. The authors [33] also question the base assumption of regarding Ψ^+ as the driving force for the evolution of the phase-field. On the other hand, adopting $\mathcal{H}$ as the crack driving force has been a procedure common to several models found in the literature (see [37, 39, 49–51] among others) and, from a modeling point of view, is analogous to the incorporation of phenomenological observations frequently done in CDM models. The maximum reference energy obtained during loading history is thus computed by considering

$$\mathcal{H} = \begin{cases} \psi_0^+\left(\nabla_s \boldsymbol{u}_n\right) & \text{for } \psi_0^+\left(\nabla_s \boldsymbol{u}_n\right) > \mathcal{H}_n \\ \mathcal{H}_n & \text{otherwise} \end{cases} \tag{2.56}$$

[5] To maintain a natural order of the complete derivation of the variational model, the variational statements will be introduced in subsequent sections

[6] Due to the fact that the equation obtained are not supported by a variational statement

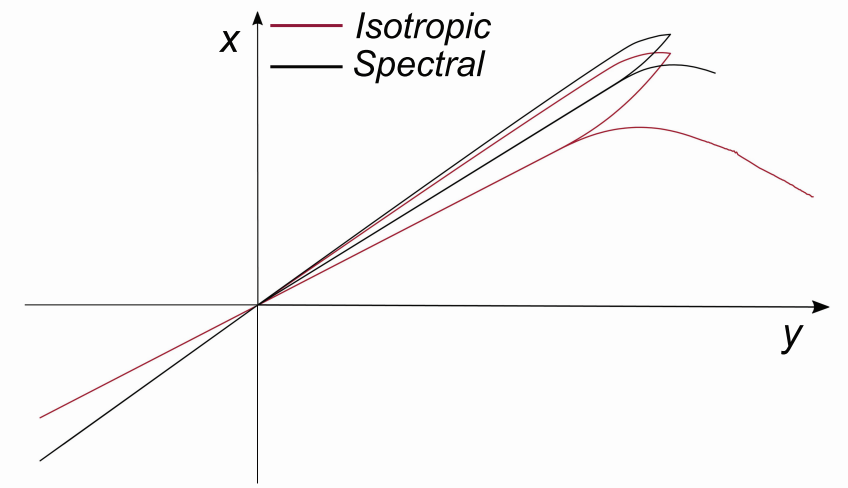


Figure 2.3: Phase-field model behavior for compressive states: unphysical stiffness degradation for the isotropic formulation

2.5.2 Penalization

The inequality is addressed via a penalization term P added to the energy functional,

$$P(c;\lambda) := \frac{\lambda_P}{2}\int_\Omega \langle c - c_{n-1}\rangle_-^2 \ \mathrm{d}\mathbf{x}, \quad \lambda \gg 1 \tag{2.57}$$

leading to a new weak form where both equations express an equality,

$$\begin{cases} E_{\boldsymbol{u}}(\boldsymbol{u}, c; \boldsymbol{v}) = 0 \quad \text{for all} \boldsymbol{v} \in \mathbf{V}_0, \\ E_c(\boldsymbol{u}, c; \beta) + \lambda_P \int_\Omega \langle c - c_{n-1}\rangle_- \beta = 0, \quad \forall \beta \in H^1(\Omega) \end{cases} \tag{2.58}$$

An additional method that can be used to model the irreversibility of the c field is to solve the differential variational inequality (DVI) naturally stemming from the minimization of $E(\mathbf{u}, c)$ with the irreversibility constraint [52, 53] instead of a Partial Differential Equation (PDE) obtained from variational principles.

2.6 Algorithm Schemes

Both equations arising from the variational statement $\delta\Pi = 0$ posses a coupled non-linear character due to the inter-dependency between the displacement and phase fields. Two types of algorithm schemes are usually employed to solve the system of equations, the so-called monolithic and staggered approaches. With the first, the two governing equations are solved simultaneously, i.e., considering an anisotropic formulation and the AT-2 model, the system

$$\begin{cases} \boldsymbol{\sigma}(\boldsymbol{u}, c) := (1-c)^2 \frac{\partial \Psi_0^+(\boldsymbol{\varepsilon})}{\partial \boldsymbol{\varepsilon}} + \frac{\partial \Psi_0^-(\boldsymbol{\varepsilon})}{\partial \boldsymbol{\varepsilon}} \\ -\ell^2 \Delta c + c = \frac{2\ell}{\mathcal{G}_c}(1-c)\mathcal{H} \end{cases} \tag{2.59}$$

is solved all at once with $\boldsymbol{\sigma} = \boldsymbol{\sigma}(\boldsymbol{u}, c)$ and $c = c(\boldsymbol{u}, c)$, since $\mathcal{H} = \mathcal{H}(\boldsymbol{u})$. The numerical treatment of 2.59 requires convergence of the vector and scalar fields as a solution pair for each step. Conversely, by using staggered solutions a solution for each field is found while fixing the other field, and an algorithm scheme with

global iterations to find $(\boldsymbol{u}; c)$ supported by two nested iterations sequentially solving for $(\boldsymbol{u})$, and (c), or vice-versa. It should be highlighted that none of the original equations lose their non-linear character (intrinsic for the phase field) if anisotropic formulations are considered [11, 43]. Conversely, the displacement equations for the isotropic (no split considered) and hybrid formulation (refer to Section 2.9) assume a linear character.
Deciding for a staggered or monolithic scheme to numerically solve fracture is a fairly complex and dividing topic. While the former provides increased robustness and modularity, since the elasticity equations may be solved using explicit or implicit schemes [6] and the impact of the phase field model is minimized, the latter leads to lower computational costs and should lead to the most accurate description of the physical phenomenon being treated. Monolithic schemes usually require one single loop of Newton-Raphson iterations (if convergence can be obtained), while staggered schemes typically require several Jacobi-type [34] iterations that allow the solver to overcome the problem of non-convexity of the fully coupled equations [54]. Considering recent contributions to phase field modeling of fracture, there seems to be a tendency to choose the latter [6, 11, 12, 33, 41, 50, 54–60] over the former [39, 46, 61].

2.7 Interpreting the variational approach to fracture as a phase-field model of brittle fracture

Over the past recent years, research focused on the variational model presented in 2.4 is based on the reinterpretation of the crack field c as a phase-field that interpolates between the unbroken and the broken states of the material [34], since both models

- model evolving (micro)structures within a bulk media
- involve recasting discrete interfaces as diffuse interfaces within a bulk phase, accomplished by the introduction of a length-scale parameter controlling the diffusive character of a growing phase
- rely on bulk energy minimization (free energy and strain energy) to develop governing equations including the interpolation of the energy of each phase (null for a crack field)
- require the definition of gradient terms to avoid localization during the evolution of the field

Moreover, the evolution of a crack is clearly a nonconserved action (no conservation law is applicable to the evolving crack surface). In subsequent expressions, the nomenclature used reflects the common practice in phase-field models for fracture: phase-field nonconserved variables used to model crack phases will be designated by the letter d, $g(d)$ designates the free energy degradation function, and Π is the functional used to develop the governing equations from variational principles.

2.8 Material and Numerical Parameters

Effective fracture toughness

Bourdin et al. [40] studied the effect of mesh size on the local energy dissipation due to the evolution of the phase-field and have shown that the fracture toughness may be significantly overestimated by insufficiently refined meshes. Taking this effect into account, an effective fracture toughness, $\mathcal{G}_{eff}$ is defined as

$$\begin{aligned} \mathcal{G}_c^{eff} &= \mathcal{G}_c \left(1 + \frac{h}{4c_w l}\right) \\ &= \mathcal{G}_c \left(1 + \frac{h}{2l}\right) \quad , \text{ AT-2 model.} \end{aligned} \tag{2.60}$$

For a vanishing ratio between mesh size h and length-scale parameter l, the effective (numerical) toughness tends to the actual (material) toughness $\mathcal{G}$.

Determination of the phase field length scale and discretization size

Traditionally, PF models must rely on significantly low values of the length-scale parameter l_0 when compared to the geometric length-scale to obtain good convergence and accurate solutions for diffuse interface problems. A similar argument regarding phase-field models for brittle fracture may be made if the problem of determining l_0 is centered on fulfilling the Γ-convergence of the diffuse crack interface within a fine tolerance. For numerical models, and as a general rule of thumb, the element size should be determined by fulfilling the condition $h \leq l_0/2$ [62]. One solution to quantify the length-scale parameter is to regard l as a material property instead of a numerical or model parameter solely related with the topology of the diffuse crack [63]. By considering the analytical solution for the free energy minimization problem of a linear elastic 1D bar with its left-end fixed and a displacement imposed on the right boundary and imposing a homogeneous phase-field, closed form expressions may be developed for l_0 as a function of three material properties - Young's modulus E, the apparent strength σ_c and the fracture toughness $\mathcal{G}_c$. The complete mathematical derivation considering the At-2 model is provided in Appendix A and leads to the following expression for l_0:

$$l_0 = \frac{27}{256} \frac{E^{'} \mathcal{G}_c}{\sigma_c^2} \tag{2.61}$$

and, for the AT-1 model,

$$l_0 = \frac{3}{8} \frac{E^{'} \mathcal{G}_c}{\sigma_c^2}. \tag{2.62}$$

Eq.2.61 is valid for 1D prescribed displacement problems involving second-order quadratic approximations for the crack surface density γ, where a homogeneous evolution of the PF ($\nabla d = 0$) or the PF evolution at $\partial\Omega$ is studied. This expression has led several authors to regard l_0 as a material parameter (derived from other materials parameters typically determined by experiments) in their models, giving rise to the so-called engineering approach to phase-field models of fracture [11]. Although regarding the length scale as a material parameter poses obvious model implementation advantages, the original Γ-convergence character of the model is now lost [43].

2.9 Hybrid Formulation

Recently, Ambati et al. [11] proposed a so-called Hybrid Formulation (HF) to PF that simultaneously assures the physical consistency of the crack process (no cracking or crack face interpenetration during compression) and a reduced computational cost compared to anisotropic formulations. The model was compared to the model developed by Miehe et al. [34] and reported savings of 85% in computational time were achieved for several applications. Furthermore, predictions for the peak load and failure modes agreed very well with the benchmark model [34]. A drawback of the HF is the loss of *variational coupling* [11] since it is no longer possible to derive the equilibrium equations from a single functional. In essence, the model is obtained by considering a linear momentum equation identical to the equation obtained for isotropic models,

$$\boldsymbol{\sigma}(\boldsymbol{u}, d) := (1-d)^2 \frac{\partial \Psi_0(\boldsymbol{\varepsilon})}{\partial \boldsymbol{\varepsilon}} \tag{2.63}$$

While, at the same time, cracking must only occur due to tensile loads, leading to the following equation:

$$-\ell^2 \Delta d + d = \frac{2\ell}{G_c}(1-d)\mathcal{H}. \tag{2.64}$$

The system of equations is still incomplete since eq. 2.63 will lead to crack faces interpenetration. This issue is addressed by spatially setting the damage variable equal to zero in all points $\boldsymbol{x}$ where the following condition holds:

$$\forall \boldsymbol{x} : \Psi_0^+ < \Psi_0^- \Rightarrow d := 0. \tag{2.65}$$

While the main drawback of the hybrid formulation is its variational inconsistency [43], its computational efficiency has proved to be far superior when compared to the anisotropic formulation. Additionaly, Ambati et al. [33] argue that the same is also true for models relying on the history field variable to impose crack irreversibility.

2.10 Understanding the phase-field approach to fracture as a damage model

Certain aspects already mentioned for CDM models in section 2.4 have been addressed above in section 2.2.2 regarding phase field models for fracture. The problem of opting to solve fully coupled or uncoupled strain and damage fields gives rise to the monolithic and staggered solution schemes in phase field models. Also, both types of fracture models rely on a diffuse representation of cracks requiring a length scale parameter to control the topology of the fracture zone. Moreover, a notion of RVEs is present in both approaches - both model cracks as a lumped effect of other defects and phenomena occurring at some smaller scale(s). While the original phase field model of brittle fracture relied on a variational framework, recent models [36, 38, 51] are not directly obtained from a variational statement, but result from physically consistent observations that agree well with past experience, as is the case with many CDM models, and incorporate stress, energy, or fracture mechanics failure criteria. Voyiadjis and Mozaffari [64] highlight some differences

between the traditional variational approach to fracture, based on fracture mechanics, proposed by Bourdin [40], Miehe [55] and other authors, and CDM models using similar models. They developed a nonlocal damage model based on a modified phase field equation and evolution laws resembling conventional damage models. The two phases associated with the phase field are averaged over an RVE which, in its damaged configuration, contains some undetermined spatial arrangement of microcracks and voids. Considering isotropic damage and a single scalar damage variable, d, this configuration would be modeled by a monotonously increasing value of d. By considering this evolution of damage as a nonconserved order parameter η, the we get the following map between d and η:

$\eta = 0, \quad d = 1 \qquad \longrightarrow$ fully damaged
$0 < \eta < 1, \quad 0 < d \longrightarrow$ damaged
$\eta = 1, \quad d = 0 \qquad \longrightarrow$ undamaged

Since a nonconserved action must take place when the phase field equations are applied to damage growth, the evolution of the order parameter with time is governed by an Allen-Cahn equation

$$\frac{\partial \eta}{\partial t} = -M_\eta \left[\frac{\partial \Psi}{\partial \eta} - \epsilon_\eta^2 \left(\nabla^2 \eta \right) \right]. \tag{2.66}$$

According to the authors, the mobility constant M_η and gradient coefficient ϵ_η, which incorporates the effect of a length scale parameter, can be obtained via experiments or by comparison with other phase field models. The free energy functional Ψ is obtained by summing the interpolation of the individual free energies of each phase (damaged, Ψ^d, and undamaged,Ψ^{ud}) with a positive dissipation term $wg(\eta)$,

$$\Psi(\bar{\varepsilon}, \eta) = h(\eta)\Psi^{ud}(\bar{\varepsilon}, \eta) + (1 - h(\eta))\Psi^{d}(\bar{\varepsilon}, \eta) + wg(\eta) \tag{2.67}$$

with $h(\eta)$ the interpolation function and $g(\eta)$ a monotonously increasing function of η [64]. Regardless of the specific functions chosen for h and $g(\eta)$, the free energy chosen for the undamaged phase is a form of strain energy that uses a decomposition of strain in *damaged* and *undamaged* elastic strain, in a similar fashion to the strain tensor decomposition methods used in other phase field models for fracture. Eq.2.67 is formally identical to those defined for the free energy functional in non-conserved problems using order parameters instead of phase fields, ϕ_i.

Chapter 3

Coupled Problems

3.1 Miehe's thermodynamically consistent model for coupled problems

A gradient damage formulation that aims to incorporate coupled field problems via a generalization of crack driving forces, either introducing energetic definitions or stress-based criteria was presented in [51]. An interesting aspect of this model is its modular framework, which is well suited to our goals. To account several phenomena of different natures, the approach proposed is based on the following steps:

- Adopt a purely geometric and modular strategy to model phase field evolution by driving the field via a balance equation for a regularized crack surface.
- Assuming the relevant constitutive assumptions for each specific model, construct a crack driving force arising from different fields combined, e.g. displacement and temperature, while maintaining the expected physical behavior during crack initiation and propagation, which should be driven by local tensile states.
- Maintain the thermodynamic equilibrium of the solid, which simultaneously guarantees the energetic equilibrium of the system and an accurate coupling between phenomena.
- Continuously degrade both mechanical and non-mechanical fluxes across crack faces.

3.1.1 Purely geometric approach

The geometric approach has its roots in Bourdin's contribution to the variational approach to fracture [30]. Adopting the crack phase field as a scalar variable defined in the entire bulk domain,

$$d : \begin{cases} \mathcal{B}_0 \times \mathcal{T} \to [0,1] \\ (\boldsymbol{X}, t) \mapsto d(\boldsymbol{X}, t) \end{cases} \tag{3.1}$$

where, as usual in gradient damage models, $d = 0$ for the unbroken state, and $d = 1$ for the fully broken state. The time variable may represent an actual time evolution, for transient, rate-dependent problems, or an incremental loading parameters

for a rate independent, quasi-static model. The solution is then sought from the minimization principle of diffusive crack topology

$$d(\boldsymbol{X},t) = \arg\left\{\inf_{d\in W_{\Gamma(t)}} \Gamma_l(d)\right\} \tag{3.2}$$

with the regularized crack surface functional given by Γ_l, defined generically in terms of the crack surface density function

$$\Gamma_l(d) = \int_{\mathcal{B}_0} \gamma_l(d,\nabla d)dV. \tag{3.3}$$

The present model distinguishes itself from other previously seen in the sense that the geometric definition of the crack surface, as given by eq. 3.3, is no longer used in the variational statement of brittle fracture according to Griffith's model. Instead, a constitutive balance equation is assumed for the regularized crack surface [51], the geometric character of the approach, thus allowing for different cracking phenomena (other than brittle fracture caused by loading a solid in its elastic regime) to be considered. The time evolution of the functional $\Gamma_l(d)$ is given by

$$\frac{d}{dt}\Gamma_l(d) = S(d,\dot{d},\mathcal{H}) \tag{3.4}$$

where S is a constitutive crack driving functional which depend on the familiar quantities d, $\dot{d}$, and the local crack driving force $\mathcal{H}$. The problem of fracture is now recast into a new constitutive and physically meaningful form:

$$\text{Evolution of the regularized crack surface} = \text{Crack driving functional.} \tag{3.5}$$

3.1.2 Evolution of the crack surface

Taking into account that $\Gamma = \Gamma(d,\nabla d)$ and applying the time derivative, chain derivative rule and some mathematical identities the geometric crack resistance may be defined as

$$\frac{d}{dt}\Gamma_l = \frac{1}{l}\int_{\mathcal{B}_0} l\delta_d\gamma_l\dot{d}\; dV + \int_{\partial\mathcal{B}_0} (\partial_{\nabla d}\gamma\cdot\boldsymbol{n}_0)\,\dot{d}\; dA, \tag{3.6}$$

where $\boldsymbol{n}_0$ is the outward normal on $\partial\mathcal{B}_0$. For a second order quadratic approximation of the crack surface,

$$l\delta_d\gamma_l = d - l^2\Delta d. \tag{3.7}$$

3.1.3 Constitutive crack driving functional

The crack driving functional S is written as the power expression

$$S = \frac{1}{l}\int_{\mathcal{B}_0} [(1-d)\mathcal{H} - \mathcal{R}]\dot{d}\; dV. \tag{3.8}$$

The last equation notoriously resembles the first term in eq. 3.6 and a justification for this is provided by the local evolution equation stemming from the global Eq. 3.4. The new quantity here introduced is he local viscous crack resistance $\mathcal{R}$ which is assumed to only depend on $\dot{d}$, $\mathcal{R}(\boldsymbol{X},t) = \tilde{\mathcal{R}}(\dot{d}(\boldsymbol{X},t))$; as typically assumed, the local

crack driving force is a function of the *state variables*, $\mathcal{H}(\boldsymbol{X},t)=\tilde{\mathcal{H}}((\text{state}(\boldsymbol{X},s),0\leq s\leq t))$. However, within the present framework it can be associated with any of the following: (1) energetic state, (2) stress state, or (3) internal variables. A straightforward constitutive assumption is made regarding the dissipative term,

$$\tilde{\mathcal{R}}=\eta\dot{d}, \tag{3.9}$$

where η is essentially a viscosity parameter affecting crack propagation. This simple approach still allows us to recover the rate-independent model, for $\eta=0$.

3.1.4 Equilibrium equations

Substituting expressions 3.8 and 3.6 into eq. 3.4 we obtain the global equilibrium of the bulk $\mathcal{B}_0$

$$\begin{aligned}\frac{d}{dt}\Gamma_l &= \frac{1}{l}\int_{\mathcal{B}_0} l\delta_d\gamma_l\dot{d}\;dV+\int_{\partial\mathcal{B}_0}(\partial_{\nabla d}\gamma\cdot\boldsymbol{n}_0)\,\dot{d}\;dA\\ &= \frac{1}{l}\int_{\mathcal{B}_0}[(1-d)\mathcal{H}-\mathcal{R}]\dot{d}\;dV.\end{aligned} \tag{3.10}$$

Accordingly, the local evolution of the crack phase field ($\dot{d}\neq 0$) across the domain is given by the statement

$$\eta\dot{d}=(1-d)\tilde{\mathcal{H}}-\left[d-l^2\Delta d\right], \tag{3.11}$$

with the Neumann condition

$$\nabla d\cdot\boldsymbol{n}_0=0\quad\text{ on }\partial\mathcal{B}_0. \tag{3.12}$$

It can be seen that the original equation 3.5 is now recast by taking into account the definition 3.8 of the crack driving functional, thus allowing to identify the terms in eq. 3.11 as

$$\textit{Phase field evolution}\quad=\textit{driving force}\;-\;\textit{Geometric crack resistance}. \tag{3.13}$$

The expression 3.11 is a generalized Ginzburg-Landau-type equation [51]. Due to the irreversibility of the cracking phenomena, an additional constraint is necessary to prevent crack healing

$$\frac{d}{dt}\Gamma_l(d)=S\geq 0, \tag{3.14}$$

which allows to interpret the crack driving force as the maximum local value reached during the entire loading history. Furthermore, and taking into account the positiveness of S, the usual restraints are also here considered: $d\in[0,1]$, $\dot{d}\geq 0$, and $\mathcal{H}\geq 0$. Consequently, the pristine and fully broken states can be identified by the following three constraints,

$$\tilde{\mathcal{H}}\Big|_{\substack{\text{unbroken}\\ \text{state}}}=0,\quad \tilde{\mathcal{H}}\Big|_{\substack{\text{broken}\\ \text{state}}}=\infty,\quad \frac{d}{dt}\tilde{\mathcal{H}}\geq 0. \tag{3.15}$$

To help clarify the relation $d=\mathcal{H}$, Miehe et al. [51] have included the close form solution for d considering a rate independent and homogeneous problem, obtained by imposing $\nabla d=\eta=0$

$$\begin{cases} d=\frac{\mathcal{H}}{1+\mathcal{H}}\in[0,1]\\[2ex] 0\dot{d}=\frac{\dot{\mathcal{H}}}{(\mathcal{H}+1)^2}\geq 0\end{cases} \tag{3.16}$$

Expressions in 3.16 clearly lead to the equivalences

$$d = 0 \Leftrightarrow \mathcal{H} = 0 \quad \text{and} \quad d = 1 \Leftrightarrow \mathcal{H} \to \infty \tag{3.17}$$

and the constraints 3.15. Finally, as a consequence of the monotonously increasing character of $\mathcal{H}$, imposed by crack irreversibility, its value is given by the ansatz

$$\tilde{\mathcal{H}}(\boldsymbol{X}, t) = \max_{s \in [0,t]} \tilde{D}(\text{state}(\boldsymbol{X}, s)). \tag{3.18}$$

Considering the constraint 3.14 and the definition 3.18,

$$\eta \dot{d} = \left\langle (1-d)\tilde{D} - l\delta_d \gamma_l \right\rangle \geq 0 \tag{3.19}$$

and, for the particular case of a rate-independent evolution, the Karush-Kuhn-Tucker conditions must be applied

$$\dot{d} \geq 0, \quad \left[(1-d)\tilde{D} - l\delta_d \gamma_l\right] \leq 0, \quad \dot{d}\left[(1-d)\tilde{D} - l\delta_d \gamma_l\right] = 0. \tag{3.20}$$

Comparing models involving different (and possibly multi-) field phenomena, Eqs. 3.19 and 3.20 provide a powerful and robust modeling strategy: it is sufficiently generic to take into account different crack driving forces arising from different (among other types, mechanical, thermal, or electrical) loading scenarios, as the only modification required is in the definition of $\tilde{D}$.

3.1.5 Numerical solution of the evolution equation

Due to the complexity of developing numerical frameworks with three or more tightly coupled fields, coupled field problems typically rely on staggered solution schemes [37, 65]. The update of the phase field is achieved by considering a staggered scheme and a constant value for $\mathcal{H}$ during the time interval between time steps. This strategy is valid regardless of the actual crack driving function and state variables considered in the problem. Under these assumptions, the time integration of eq. 3.10 leads to a closed form solution

$$\begin{aligned} \Gamma_l(d_n) =& \Gamma_l\left(d_{n-1}\right) + \\ & \frac{1}{l}\int_{\mathcal{B}_0} \left\{ \left[(d_n - d_{n-1}) - \frac{1}{2}\left(d_n^2 - d_{n-1}^2\right) \right] \mathcal{H}_n + \right. \\ & \left. - \frac{\eta}{2\tau}\left(d_n - d_{n-1}\right)^2 \right\} dV. \end{aligned} \tag{3.21}$$

Algorithm 1: Staggered solution scheme for load step n at t_n

Initialization, k=0, TOL_{state} at current time step t_n;
Set $\mathcal{H}_n = \mathcal{H}_{n-1}$.
Staggered iterative procedure, $k \geq 1$:
2. *Update crack surface* with respect to $\mathcal{H}_n^k$,
$d = f(\mathcal{H})$
3. *Update the bulk response*: given d, update the bulk response by an iterative procedure, using some specified crack transition rule,
$\hat{\boldsymbol{f}}(\text{ state };d) = g^s(d)\tilde{\boldsymbol{f}}^s(\text{ state }) + g^c(d)\tilde{\boldsymbol{f}}^c(\text{ state })$
4. *Update the crack driving force*: for given state variables $state(\boldsymbol{X}, s)$ of bulk response, update the history variable
$\mathcal{H}(\boldsymbol{X}, t) = \max_{s\in[0,t]} \tilde{D}(\text{state}(\boldsymbol{X}, s))$
5. Repeat steps from 2 to 4 until convergence is achieved considering some measure of error, $E(state)$, such that
$E(\text{state}(\boldsymbol{X}, s) \leq TOL_{state}$.

3.2 Algorithm scheme

The question of choosing staggered or monolithic schemes to solve coupled problems is similar to the same issue regarding the phase field models for brittle fracture. The arguments in favor of both approaches are identical to those mentioned in Section 2.6 and demand a careful study of the phenomena relevant for each problem. For instance, Singh and Pal [66] solve a coupled chemo-mechanical fracture problem using staggered (decoupled) iterations for the chemical and mechanical *sub-problems*. Miehe et al [51] solved a coupled temperature/displacement/phase field problem using staggered iterations for the phase field and remaining field, while solving the thermomechanical problem with a monolithic scheme. The effect of crack energy dissipation and plasticity were considered within the coupled field framework, which potentially implies a strong coupling between the latter fields. On the other hand, brittle fracture models (negligible plasticity and abrupt crack propagation) with no contact between solid bodies are typically modeled as loosely-coupled problems, thus enabling staggered solution schemes. However, using a fully staggered algorithm to solve for the three fields would require three nested loops per each staggered global iteration, thus increasing computational cost even further than what is typically observed for elastic problems involving brittle fracture governed by a phase field. It is thus seen that opting for a solution scheme must be supported by both physical and numerical principles.

3.3 Diffusion problems in fractured media

The development of analytical and numerical fracture models has led to an increasing interest in coupled problems where cracks arise or develop due to the impact of, not only the mechanical phenomenon, but also other fields. Moreover, a two-way effect is here involved since the presence of cracks also affects diffusion caused by field gradient. The review work [5] on Li-ion batteries currently used in electric vehicles reports several crack phenomena degrading the electro-chemical performance at the battery cell level, which is explained by thermal, electrical, and chemical field

high concentrations and a change in respective fluxes. Kuna [8] mentions that a recent rise in interest to study coupled problems is especially motivated by the new usage of multi-functional materials in mechatronics, adaptronics and microsystem technology - an immediate parallel can be made with the motivations that support the present work. Restricted to simple field problems, Poisson's equation describes a diffusive flux in terms of a scalar field gradient - for instance, temperature, concentration of a species, and electric potential for thermal, chemical, and electrostatics problems, respectively - and its general expression for 2-D problems is [67]:

$$\left(\frac{\partial^2}{\partial x^2} + \frac{\partial^2}{\partial y^2}\right)\phi(x,y) = f(x,y) \tag{3.22}$$

where ϕ is a scalar potential and the physical meaning of the diffusive flux $f(x,y)$ and $\nabla^2 = \left(\frac{\partial^2}{\partial x^2} + \frac{\partial^2}{\partial y^2}\right)$ is problem dependent. Moreover, Poisson's equation degenerates into Laplace's equation if the diffusive flux is null, i.e., for $f(x,y) = 0$:

$$\nabla^2\phi(x,y) = 0 \tag{3.23}$$

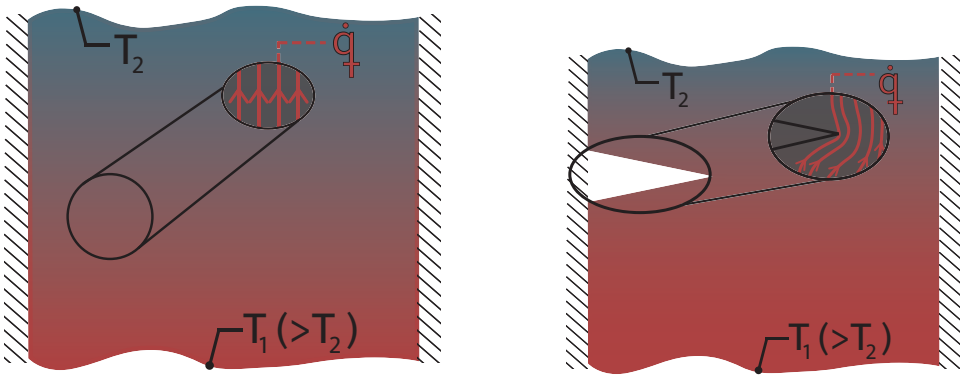
which, according to the first law of thermodynamics, is the form of Fourier's law if no internal heat sources are present, or Fick's law for a system with null species diffusion.

3.3.1 Definition of material degradation for diffusion problems

The concept of stiffness degradation due to the evolution of the phase field may be extended to the generic case of *material degradation* in diffusion problems. On the other hand, taking into account traditional phase field models, this degradation may be reinterpreted as a simple evolution of an interpolation between corresponding values of two phases (the crack and pristine phases) for the same material property. Considering a material property k assuming the values k_d and k_b for the cracked and non-cracked domains, respectively, a value for k of the bulk can be obtained (in an averaged, RVE sense) using an interpolation function $g(d)$,

$$k(d) = g(d)^2 k_d + (1 - g(d))^2 k_b. \tag{3.24}$$

As an example, consider the case of steady-state heat conduction across a square plate with an end-notch of size a, modeled by a phase-field d, adiabatic vertical boundaries and prescribed temperatures T_1, at the bottom, and T_2, at the top ($T_1 > T_2$). The concentration of the thermal field at a crack is schematically shown in Fig. 3.1 and is analogous to the stress concentration effect near notched regions.



(a) Unnotched heat flux (b) Notched heat flux

Figure 3.1: Unnotched heat flux and concentration of the thermal field near the crack

3.4 Heat Transfer problem in solid media

The heat equation for the solid bulk domain in Fig. 3.2 is given by an equilibrium between the rate of change in internal energy and the sum of volumetric heat generation and heat conduction across the boundaries. Assuming homogeneous properties, it assumes the form of the Fourier equation

$$C\frac{\partial T}{\partial t} = k_x\frac{\partial^2 T}{\partial x^2} + ky\frac{\partial^2 T}{\partial y^2} + k_z\frac{\partial^2 T}{\partial z^2} + \dot{g}, \tag{3.25}$$

where:

- C is the volumetric heat capacity, defined as $C = c\rho$ for solid bodies, where c is the specific heat capacity per unit mass.
- k_i is the thermal conductivity along direction i, with $i = x, y, z$.
- $\dot{g}$ is the total heat generated within the entire bulk domain.

For the special case of a solid layer of material with constant in-plane thermal conductivity, eq. 3.25 may be simplified and recast in the form

$$C\frac{\partial T}{\partial t} = k_1\left(\frac{\partial^2 T}{\partial x^2} + \frac{\partial^2 T}{\partial y^2}\right) + k_2\frac{\partial^2 T}{\partial z^2} + \dot{g}. \tag{3.26}$$

with the following boundary conditions:

$$\begin{aligned} T &= \bar{T} \text{ on } \Gamma_T \\ \mathbf{k}\nabla\mathbf{T} &= -q \text{ on } \Gamma_q \end{aligned} \tag{3.27}$$

where q is a prescribed heat flux, Γ_T is the boundary where temperature is prescribed, and Γ_q is the boundary of prescribed flux.

3.4.1 Weak and FEM form of the 2-D transient heat equation

Re-writing the differential equation 3.26 for transient planar conduction problems with no internal heat sources in the following notation:

$$C\frac{\partial T}{\partial t} - \boldsymbol{\nabla}\cdot[\boldsymbol{k}\bullet\boldsymbol{\nabla T}] = 0 \tag{3.28}$$

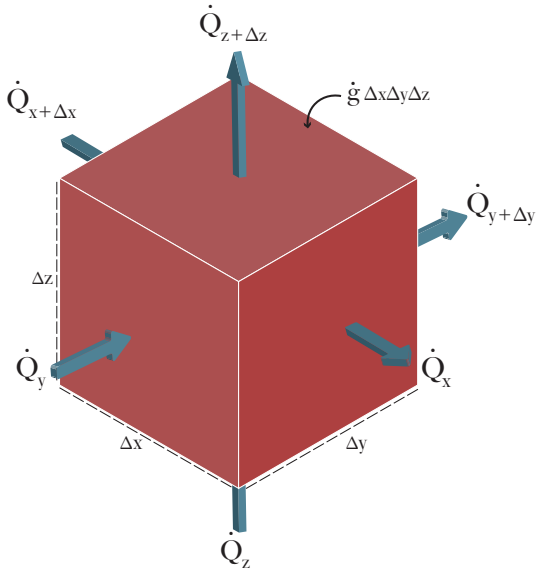


Figure 3.2: Heat conduction in a solid with internal heat source

the weak form after integration by parts for the 2D transient heat conduction problem with prescribed temperature or heat flux at the boundaries following the Galerkin method is [68]:

$$\int_\Omega \left(C\frac{\partial T}{\partial t}\right) w\, dV + \int_\Omega (\boldsymbol{\nabla} w)\cdot(\mathbf{k}\bullet\boldsymbol{\nabla} T)dV = \int_\Omega \dot{g} w\, dV + \int_{\Gamma_q} [w(\mathbf{k}\bullet\boldsymbol{\nabla} T)]\bullet\mathbf{n}\, dA. \quad (3.29)$$

The numerical FEM equations that result from a geometrical discretization and standard interpolation of T using nodal values and shape functions N_i is written in a convenient form as

$$[\mathbf{C}]\left\{\frac{d\mathbf{T}}{dt}\right\} + [\mathbf{K}]\{\mathbf{T}\} = \{\mathbf{f}\} \quad (3.30)$$

analogous to the equation found for dynamic analysis of mechanical systems, with the quantities below defined:

$$\begin{aligned}
[\mathbf{C}] &= \textstyle\int_\Omega C\,[\mathbf{N}]^T\,[\mathbf{N}]\,d\Omega,\\
[\mathbf{K}] &= \textstyle\int_\Omega [\mathbf{B}]^T\,[\mathbf{D}]\,[\mathbf{B}]\,d\Omega,\\
[\mathbf{D}] &= \begin{bmatrix} k_x & 0 \\ 0 & k_y \end{bmatrix},\\
\{\mathbf{f}\} &= -\textstyle\int_{\Gamma_q} \mathbf{q}\,[\mathbf{N}]^T\,d\Gamma.
\end{aligned} \quad (3.31)$$

For thermal problems coupled with a phase-field model for brittle fracture, and assuming an isotropic thermal behavior, the effect of phase-field cracks in heat diffusion may be simply modeled by a functional dependency of the thermal conductivity and heat capacity on the phase-field variable according to Eq. 3.24.

3.5 Concluding remarks

In this chapter, an extensive review of the framework proposed in [51] for coupled problems involving phase-field models for fracture. Given the motivation to model elasto-plastic fracture involving significant heat dissipation effects prior to catastrophic failure, this model departs from the starting point of the variational approach to fracture - Griffith's law - relying on a minimization of the diffuse crack topology. Moreover, a strong coupling with other fields is considered since, in order to assure thermodynamic consistency of the entire model, dissipative terms and contributions from other field to the crack driving functional must be considered.
Restricting the analysis to quasi-static brittle fracture processes, a different and loosened type of coupling may be considered given the absence of dissipative phenomena prior to (catastrophic) crack propagation. The set of coupled problems considered within the scope of the present work are described by loosely coupled frameworks, for which the only coupling existing between the phase-field and other potential fields is the degradation of material properties (effect of cracks in coupled field) and the existence of eigenstrains which, in turn, affect the stress state of the material.
Heat conduction in solids was briefly described in section 3.4 as a diffusion example problem that may be modeled according to the loosely coupled strategy above mentioned. The necessary steps to develop a coupled thermal and phase-field fracture problem are the definition of material parameters conductivity, heat capacity, and thermal expansion in terms of d (according to Eq. 3.24) and a calculations of the thermal stresses arising from the time- and space-dependent thermal expansion of the body.

Part III

Phase-field analysis models to predict brittle fracture in coupled problems

Chapter 4

A Phase Field Model for Brittle Fracture

The review provided in 2.4 allows us to establish a step-by-step approach to develop a Phase Field model from its continuous to finite element discrete formulation.

Step 1 - Reformulate Griffith's law for brittle fracture using a variational statement

For the solid body represented in Fig.4.1 on the left, and following the variational approach proposed by [29], consider the functional

$$\Pi(\mathbf{u})^* = \int_\Omega \Psi_e dV + \int_\Gamma \mathcal{G}_c dS \tag{4.1}$$

which assumes that the free energy for the problem of brittle fracture is given by the sum of the strain energy and surface energy associated with crack surfaces,

$$F = \Psi_e + \mathcal{G}_c \Gamma \tag{4.2}$$

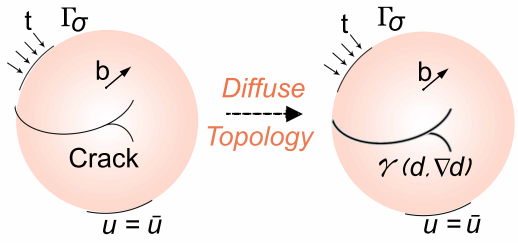


Figure 4.1: Definition of the continuum and nomenclature considered for the variational statement. Representation of a diffuse crack topology. Adapted from [1]

Step 2 - Change the fracture energy term into a regularized expression

. It is necessary to obtain a functional allowing suitable numerical implementations, which is achieved by a regularization of the fracture energy associated

with the recast of the sharp crack Γ as its smeared representation, mathematically described by a crack surface density γ,

$$\int_{\Gamma} dS \approx \int_{\Omega} \gamma dV \tag{4.3}$$

The new diffusive crack is illustrated in Fig. 4.1 on the right. The γ functional here proposed corresponds to a second order quadratic approximation given by

$$\gamma(\mathrm{d}, \nabla \mathrm{d}) = \frac{1}{2l}\mathrm{d}^2 + l/2|\nabla \mathrm{d}|^2 \tag{4.4}$$

that leads to the AT-2 model, for which the following aspects are considered:

- It ensures Γ-convergence.
- Its value over the domain is determined by the PF variable d
- d is here taken as a damage-like variable ranging from a null value (undamaged) to $d = 1$ (fully damaged material) with $\dot{d} >= 0$.
- The dependence $\gamma = \gamma/d, \nabla d$ takes into account not only the local character, but also non-local effects associated with damage progression.
- The functional allows an onset of damage since the initial load step (i.e. $d \geq 0$ for any initial tensile state), which can be seen by substituting $\bar{u}$ for any positive value in expression A.3 provided in the Appendix A.

Given that sharp discontinuities are no longer developed within the bulk, the domain of integration for the first integral in eq. 4.1 must be substituted by the entire bulk volume. The elastic strain energy released with fracture, and, subsequently stiffness degradation, must now be modeled as a function of the damaged state, by means of a function $g(d)$, here chosen as a quadratic function of d:

$$g(\mathrm{d}) = (1 - \mathrm{d})^2. \tag{4.5}$$

The procedure to obtain the governing equilibrium crack phase-field equations is a classical variational approach as typically employed in computational mechanics, i.e., the total potential energy of the system Π (the functional of the phase-field problem) must be postulated and the stationarity of Π must be invoked, $\delta\Pi = 0$ with respect to all state variables considered [69]. The following expressions are concerned with quasi-static processes involving brittle fracture in purely elastic media and negligible dynamic effects. Based on the constitutive and geometrical assumptions above listed, it is now possible to write a regularized version of the original functional in 4.1. Considering a general loading case with the existence of body and traction forces, represented by the load vectors $\mathbf{b}$ and $\mathbf{t}$, respectively, a final expression for the energy functional is thus obtained,

$$\Pi(\mathbf{u}) \approx \Pi(\mathbf{u}, \mathrm{d}) = \int_{\Omega} g(\mathrm{d})\Psi_e dV + \int_{\Omega} \mathcal{G}_c \cdot \left(\frac{1}{2l}\mathrm{d}^2 + \frac{l}{2}|\nabla \mathrm{d}|^2\right) dV + \int_{\Omega} \mathbf{b} dV + \int_{S} \mathbf{t}\mathbf{u} dS \tag{4.6}$$

and a solution $(\mathbf{u}, d)$ for Eq. 4.6 is obtained by invoking the stationarity of Π, $\delta\Pi = 0$ with respect to the state variables,

$$(\mathbf{u}, \mathrm{d}) = arg\ inf\ \{\Pi(\mathbf{u}, \mathrm{d})\}, \quad \mathbf{u} \in V, \mathrm{d} \in D \tag{4.7}$$

where

$$V = \left\{ \mathbf{u} \in H^1 : \mathbf{u} = \bar{\mathbf{u}} \; on \; \partial\Omega_{\mathbf{u}} \right\}$$
$$D = \left\{ \mathrm{d} \in H^1 : \mathrm{d} = 0 \; on \; \partial\Omega \right\} \tag{4.8}$$

and H^1 is the Sobolev space.
For the phase-field, only Dirichlet boundary conditions are prescribed (to model, for instance, an initial notch) which is possible since the coupling of the fields is made under the assumption that displacement drives the phase-field and prescribed external loading are only associated with displacements [34]. Neumann-type boundary conditions for the phase-field arise from the impossibility to have damage extending beyond the solid volume,

$$\partial_{\nabla d}\phi \cdot \boldsymbol{n} = 0 \quad \text{on } \partial\mathscr{B} \tag{4.9}$$

Step 3 - Obtain a weak form from the variational statement

The solution (u,d) as given by 4.7 is obtained by taking into account the weak form equations governing the global and local equilibrium of the volume solid Ω,

$$\begin{cases} \delta\Pi_{\boldsymbol{u}}(\boldsymbol{u}, \mathrm{d}; \boldsymbol{v}) = 0, \quad \forall \boldsymbol{v} \in \mathbf{V}_0 \\ \delta\Pi_{\mathrm{d}}(\boldsymbol{u}, d; \beta - \mathrm{d}) \geq 0, \quad \forall \beta \in D_{d_{n-1}} \end{cases} \tag{4.10}$$

where the inequality observed for d stems from the necessary condition of irreversibility imposed on the crack field (see section 2.4), v and β are trial functions, and

$$\mathbf{V}_0 := \left\{ \boldsymbol{v} \in \mathbf{H}^1(\Omega) : \boldsymbol{v} = \mathbf{0} \text{ on } \Gamma_{D,0} \cup \Gamma_{D,1} \right\}$$
$$D_{d_{n-1}} := \left\{ \mathrm{d} \in H^1(\Omega) : \mathrm{d} \geq \mathrm{d}_{n-1} \text{ in } \Omega \right\}. \tag{4.11}$$

The variational expressions obtained by considering the expression for $\Pi(u, d)$ given in 4.6 for the AT-2 model are the following:

$$\delta\Pi_{\boldsymbol{u}}(\boldsymbol{u}, \mathrm{d}; \boldsymbol{v}) := \int_\Omega \left[\mathrm{g}(\mathrm{d}) \frac{\partial \Psi}{\partial \boldsymbol{\varepsilon}}(\boldsymbol{\varepsilon}(\boldsymbol{u}), \mathrm{d}) \right] : \boldsymbol{\varepsilon}(\boldsymbol{v}) \mathrm{d}\mathbf{x} - \int_{\Gamma_{N,1}} \bar{\boldsymbol{t}}_n \cdot \boldsymbol{v} \mathrm{d}s$$
$$\delta\Pi_{\mathrm{d}}(\boldsymbol{u}, \mathrm{d}; \beta) := \int_\Omega \left[\mathrm{g}'(\mathrm{d}) \Psi^+(\boldsymbol{\varepsilon}(\boldsymbol{u})) \beta + \frac{G_c}{2} \left(\frac{1}{\ell} 2\mathrm{d}\beta + 2\ell \nabla \mathrm{d} \cdot \nabla \beta \right) \right] \mathrm{d}\mathbf{x}. \tag{4.12}$$

4.0.1 Ensuring a Correct Physical Behavior

If the solution pair (u,d) is obtained by merely considering Π as given by Eq.4.12 leads to crack healing, crack face interpenetration, and cracking due to compression, upon load reversal. To eliminate such an unphysical behavior of the cracked body, the following modifications are considered:

- Additive decomposition of the free energy Ψ, $\Psi = \Psi^+ + \Psi^-$, and partial degradation of Ψ by considering $Psi(\mathrm{d}, \mathbf{u}) = g(\mathrm{d})\Psi^+ + \Psi^-$, simultaneously breaking the symmetry of cracking in tension/compression and preventing crack face interpenetration.

- Substitution of the positive component of Ψ for the maximum positive free energy that has been attained since the initial state considered, $\mathcal{H}$, to ensure no crack healing occurs.

The additive decomposition proposed here is either based on the spectral decomposition of strain,

$$\Psi^{\pm} = \lambda/2 \cdot \left(\langle tr[\varepsilon]\rangle^{\pm}\right)^2 + \mu \cdot tr[(\varepsilon^{\pm})^2] \tag{4.13}$$

where the spectral decomposition of the strain tensor is given by

$$\varepsilon^{\pm} = \sum_{i=1}^{n} \langle \varepsilon_i \rangle^{\pm} \cdot \boldsymbol{N}_i^{\varepsilon} \otimes \boldsymbol{N}_i^{\varepsilon}. \tag{4.14}$$

or on the volumetric/deviatoric decomposition of strain. Introducing the spectral decomposition defined by expression 4.13, a new bulk strain energy integral expression may be considered,

$$\int_{\Omega} g(\mathrm{d}) \cdot \Psi_e^{+} + \Psi^{-} dV. \tag{4.15}$$

The total variation of Π may now be evaluated as

$$\begin{aligned}\delta\Pi_b(\mathbf{u}, \delta\mathbf{u}, d, \delta d) = &\int_{\Omega} \sigma : \delta\varepsilon dV + \int_{\partial\Omega} \overline{\mathbf{t}} \cdot \delta\mathbf{u} d\partial V + \int_{\Omega} \mathbf{b} \cdot \delta\mathbf{u} dV + \\ &\int_{\Omega} \mathcal{G}_c l \left[\frac{1}{l^2} d\delta d + \nabla d \cdot \nabla(\delta d)\right] dV - \int_{\Omega} 2(1-d)\delta d \Psi_e^{+}(\varepsilon) dV.\end{aligned} \tag{4.16}$$

Crack irreversibility is achieved by substituting Ψ_e^{+} in 4.16 by $\mathcal{H}$, with

$$\mathcal{H}(\mathbf{x}, t) = \max_{\tau \in [0,t]} \Psi_e^{+}(\varepsilon)(\mathbf{x}, t) \tag{4.17}$$

and an updated version of the third integral expression on the right-hand side of 4.16 is thus achieved,

$$\int_{\Omega} 2(1-d)\delta d \mathcal{H}(\mathbf{x}, t) dV. \tag{4.18}$$

Final Weak Form

The weak form obtained by redefining the strain energy terms in the variational statement 4.12

$$\begin{cases} \int_{\Omega} \sigma : \delta\varepsilon dV + \int_{\partial\Omega} \overline{\mathbf{t}} \cdot \delta\mathbf{u} d\partial V + \int_{\Omega} \mathbf{b} \cdot \delta\mathbf{u} dV = 0 \\ \\ -\int_{\Omega} 2(1-\mathrm{d})\delta\mathrm{d}\Psi_e^{+}(\varepsilon) dV + \int_{\Omega} \mathcal{G}_c l \left[\frac{1}{l^2}\mathrm{d}\delta\mathrm{d} + \nabla\mathrm{d} \cdot \nabla(\delta\mathrm{d})\right] dV = 0 \\ \\ U = \{\delta\mathbf{u} \mid \mathbf{u} = \overline{\mathbf{u}} \text{ on } \partial\Omega_u, \mathbf{u} \in \mathcal{H}^1\} \\ \\ D = \{\delta\mathrm{d} \mid \delta\mathrm{d} = 0 \text{ on } \Gamma_b, \mathrm{d} \in \mathcal{H}^0\} \end{cases} \tag{4.19}$$

It is interesting to note that, although we are restricting the analysis to a quasi-static process, the *arrow of time* is implicitly added to the formulation in association with the irreversibility involved in cracking. Note, also, that $\mathcal{H}$ only affects the integral

term related to δd since the stiffness, and, hence, stress tensor still depend on the current value of strain energy, according to the following expression:

$$\begin{aligned}\sigma &= g(\mathrm{d}) \cdot \frac{\partial \Psi_e^+}{\partial \varepsilon} + \frac{\partial \Psi_e^-}{\partial \varepsilon} \\ &= (1-\mathrm{d})^2 \sigma^+ - \sigma^-.\end{aligned} \tag{4.20}$$

where Similarly, a thermodynamic force Y may be defined for the evolution of the phase-field

$$\begin{aligned}Y &= -\frac{\partial \Psi}{\partial \mathrm{d}} \\ &= -g'(\mathrm{d})\Psi_e^+\end{aligned} \tag{4.21}$$

Furthermore, the Allen-Cahn evolution equation (see Eq.2.24) is considered to govern the phase field evolution,

$$\begin{aligned}\frac{\partial \mathrm{d}(\mathbf{x},t)}{\partial t} &= -L\frac{\delta F(\mathrm{d})}{\delta \mathrm{d}(\mathbf{x},t)} \\ &= -L\left[\frac{\partial f_0(\mathrm{d})}{\partial \mathrm{d}} - \nabla \cdot \kappa(\mathrm{d}) \nabla \mathrm{d}\right].\end{aligned} \tag{4.22}$$

where the mobility is defined as $L = (\mathcal{G}_c \eta)$, η is the parameter used in the viscous regularization procedure used to alleviate convergence difficulties, and $\kappa = 2\mathcal{G}_c l/2$. The free energy F may be divided in the local and gradient terms

$$\begin{aligned}F &= g(\mathrm{d})\mathcal{H} + \Psi^- + \frac{1}{2}\left(\mathcal{G}_c/l \cdot \left(1-\mathrm{d}^2\right) + \mathcal{G}_c l \left|\nabla \mathrm{d}\right|^2\right). \\ &= F_{loc} + \mathcal{G}_c l/2 \left|\nabla \mathrm{d}\right|^2\end{aligned} \tag{4.23}$$

Substituting in Eq.4.22, the following evolution equation is obtained

$$\dot{d} = -L\left(\frac{\partial F_{loc}}{\partial \mathrm{d}} - \nabla \cdot \kappa \nabla \mathrm{d}\right) \quad = -L\left(-Y + \mathcal{G}_c l d - \nabla \cdot \kappa \nabla d\right). \tag{4.24}$$

In a similar way to Eq.2.24, the evolution of the crack phase-field is governed by a positive term related to minimization of the free energy, and a negative surface energy term penalizing the growth of a crack interface.

4.0.2 FEM discretization of the Domain

The displacement vector throughout the domain of each finite element is given by the interpolation of nodal values using shape functions. Furthermore, the same interpolation scheme is considered for both state variables d and $\mathbf{u}$,

$$\begin{cases} \mathbf{u}_e \cong \sum_{i=1}^n \boldsymbol{N}_i^u \cdot \mathbf{u}_i^e = \boldsymbol{N}_e^u \mathbf{u} \\ \delta\mathbf{u}_e \cong \sum_{i=1}^n N_i^u \delta\mathbf{u}_i^e = \boldsymbol{N}_e^u \delta\mathbf{u} \\ \Delta\mathbf{u}_e \cong \sum_{i=1}^n N_i^u \Delta\mathbf{u}_i^e = \boldsymbol{N}_e^u \Delta\mathbf{u} \end{cases} \quad \begin{cases} \mathbf{d}_e \cong \sum_{i=1}^n N_i^d \cdot d_i^e = \boldsymbol{N}_e^d \boldsymbol{d} \\ \delta\mathbf{d}_e \cong \sum_{i=1}^n N_i^d \delta d_i^e = \boldsymbol{N}_e^d \delta\boldsymbol{d} \\ \Delta\mathbf{d}_e \cong \sum_{i=1}^n N_i^d \Delta d_i^e = \boldsymbol{N}_e^d \Delta\boldsymbol{d} \end{cases} \tag{4.25}$$

Considering a generic discretization of the domain Ω into a set of n elements, the continuous weak form in expression 4.19 is redefined as

$$\begin{aligned}\delta\tilde{\Pi}_b^{el}(\mathbf{u},\delta\mathbf{u},\mathbf{d},\delta\mathbf{d}) = \delta\mathbf{u}^{\mathrm{T}}\Bigg\{\sum_{e=1}^{n}\int_{\Omega_e}\Big[\Big((1-d)^2+k\Big)\,\mathbf{B}_e^{\mathbf{T}}\sigma_+ + \mathbf{B}_e^{\mathrm{T}}\sigma_-\Big]\,dV + \\ -\sum_{e=1}^{n}\int_{\Omega_e} N_e^{\mathrm{T}}\,\bar{\mathbf{t}}\;d\partial V - \sum_{e=1}^{n}\int_{\Omega_e} N_e^{\mathrm{T}}\mathbf{b}\;dV\Bigg\} \quad + \\ \delta\mathbf{d}^{\mathrm{T}}\Bigg\{\sum_{e=1}^{n}\int_{\Omega_e} -2(1-d)N_e^{\mathrm{T}}\Psi_+^e(\varepsilon)dV + \\ \sum_{e=1}^{n}\int_{\Omega_e}\mathcal{G}_c l\left(\mathbf{B}_e^{\mathrm{T}}\nabla d + \frac{1}{l^2}N_e^{\mathrm{T}}d\right)dV\Bigg\}\end{aligned} \quad . \tag{4.26}$$

The governing equations can be obtained in a similar way to in eq. 4.19, resulting in the following matricial system of equations:

$$\begin{bmatrix} \boldsymbol{K_{uu}}(\mathbf{u}) & \boldsymbol{K_{ud}} \\ \boldsymbol{K_{du}} & \boldsymbol{K_{dd}} \end{bmatrix} \cdot \begin{bmatrix} \mathbf{u} \\ \mathbf{d} \end{bmatrix} = \begin{bmatrix} \boldsymbol{f_{u,ext}} \\ \mathbf{0} \end{bmatrix} - \begin{bmatrix} \boldsymbol{f_{u,int}} \\ \boldsymbol{f_{d,int}} \end{bmatrix} \tag{4.27}$$

4.0.3 Determination of Numerical/Material Parameters

As previously mentioned in section 4, the PF variable is here regarded as a damage variable associated with degradation of elastic stiffness. In the context of the so-called Fracture Mechanics approach that considers the PF model as a continuum damage-like model, the length scale l introduced in expression 4.4 is seen as a material parameter and, for the second order quadratic approximation given by 4.4, it is defined as

$$l = \frac{27}{256}\frac{\mathcal{G}_c E}{\sigma_c^2} \tag{4.28}$$

where E is the Young's modulus of the material, σ_c a maximum strength defined, e.g., as the experimental tensile strength. If both the material toughness and strength are known, the length-scale parameter can be computed using the former expression. Conversely, if there is no *a priori* experimental characterization for both parameters, then an approach closer to traditional phase-field models used by the materials science community must be considered choosing a vakue for l low enough to obtain Γ convergence within a specified tolerance.

To prevent ill-conditioning of the stiffness matrix arising from a full degradation of local stiffness, the degradation function *g(d)* is redefined as

$$g(d) = (1-d)^2 \cdot (1-k) + k \tag{4.29}$$

where k is a numerical constant taken as $k \approx 10^-5$ following [49]. On the other hand, to prevent the overestimation of the fracture domain, either a numerical *effective* critical energy release rate needs to be considered,

$$\mathcal{G}_{eff} = \mathcal{G}_c \cdot \left(1 + \frac{h}{4l}\right) \tag{4.30}$$

where h is the characteristic finite element length, or the ratio l/h must be $l/h \geq 5$ [40] leading to negligible local crack spurious modes.

4.0.4 Algorithm Scheme

Since the system of equations 4.27 is non-linear with respect to both variables, a linearization is needed. The matrix equation may be rewritten in its residual form

$$\begin{bmatrix} \mathbf{r}_u \\ \mathbf{r}_d \end{bmatrix} = \begin{bmatrix} \boldsymbol{K_{uu}}(\mathbf{u}) & \mathbf{0} \\ \mathbf{0} & \boldsymbol{K_{dd}} \end{bmatrix} \cdot \begin{bmatrix} \mathbf{u} \\ \mathbf{d} \end{bmatrix} - \begin{bmatrix} \boldsymbol{f_{u,ext}} \\ \mathbf{0} \end{bmatrix} - \begin{bmatrix} \boldsymbol{f_{u,int}} \\ \boldsymbol{f_{d,int}} \end{bmatrix} \tag{4.31}$$

The algorithm 2 describes a fixed point iterative scheme that can be used when decoupling a fracture phase-field from all other fields considered (to understand the quantities here involved, see Section 3.1).

Algorithm 2: Staggered solution scheme for load step i at t_i

Input: $(\boldsymbol{u}_{i-1}, \boldsymbol{d}_{i-1})$, $\mathcal{H}_{i-1}$
Output: $(\mathbf{u}_i, d_i)$
Initialization, k=0, $\text{TOL}_{\mathbf{u}}$, $\text{TOL}_{\mathbf{d}}$: ;

1. set $\left(\boldsymbol{u}^0, \boldsymbol{d}^0\right) = (\boldsymbol{u}_{i-1}, d_{i-1})$.

Staggered iteration, $k \geq 1$:

2. Update $\mathcal{H}$ in the domain.
3. Given the fixed displacement $\boldsymbol{u}_{i-1}$, solve $\Delta\mathbf{d} = \mathbf{d}_i^{(k)} - \mathbf{d}_{i-1}$.
4. Given the updated *phase field* $\mathbf{d}_i^{(k)}$, solve $\Delta\ \boldsymbol{u} = \boldsymbol{u}_i^{(k)}$ - $\boldsymbol{u}_{i-1}$.
5. Check RES^k $(\boldsymbol{u}_i^{(k)}, \boldsymbol{d}_i^{(k)}) \leq \text{TOL}$
   If fulfilled, move on to next load step

4.1 Rate-independent models

As demonstrated by Miehe et al. [55], the equation developed for the rate-dependent model,

$$\frac{g_c}{l}\left[d - l^2\Delta d\right] + \eta\dot{d} = 2(1-d)\mathcal{H} \tag{4.32}$$

may be used to model rate-independent fracture provided the viscosity parameter η is re-interpreted as a viscous regularization parameter. Numerical studies have demonstrated that $\eta \leq 1E-6$ leads to rate-independent results prior to failure, as well as limited influence on the post-peak behavior [55]. However, the value of η must be adjusted for each model, especially when either the post-peak behavior is of interest or if alternative crack driving forces are considered.

Chapter 5

Model Implementation

5.1 Introduction

In this chapter, some aspects of the numerical implementation strategy adopted for the phase field model described in chapter 4. The open-source FEM software MOOSE [65] was used to obtain the numerical solutions presented in chapter 6. Some of the pre-existing modeling capabilities for phase field and elasticity models were used to reduce the implementation effort. Moreover, the software was chosen due to its modular and multi-field driven architecture that naturally handles coupled problems. Element technology is handled by MOOSE using the public library *libmesh* [70]. It provides users with mesh generators capable of constructing simple mesh geometries, such as plates, cubes, annular rings, and 3D beam-like geometries of standard cross-sections. On the other hand, MOOSE also provides the user with the possibility to import meshes generated with other software tools, such as *Abaqus* using Abaqus input files. Both strategies were used for the models presented hereafter.
One of the most important aspects of coupled fields is the method used to solve the entire system of governing equations. The staggered (loosely coupled) and monolithic (strongly coupled) approaches have been briefly discussed in Part II, focusing on the coupled elasticity and phase field problem, but also addressing the issue of solving problems involving other fields such as heat conduction in solid media. While MOOSE provides the option to solve models using a strongly coupled framework, it is also possible to consider a loosely coupled approach by constructing independent models for each individual problem (or for a subset of problems) and transfer from other fields *just* the coupling information required to obtain a new solution. Information is transferred following a hierarchical relation between each problem.

5.2 Numerical and modeling aspects

Adaptive remeshing Strategy

The algorithm implemented on MOOSE performs an adaptation on the discretization based on a given measure of local error. The user can define this error based on an energy error norm, a jump on the gradient of a variable across element boundaries, as proposed in [71], leading to an error estimator e_i for each element i

[8]

$$(e_i)^n = \sum_{k=1}^{N_K} l_k \left\| \Delta u_i \right\|^n \tag{5.1}$$

where n is an integer, N_K are all element edges, l_k is the length of edge k, and u_i is the variable whose gradient jump, Δu_i, is under consideration. The jump of a variable's value across a boundary can be considered (an approach only valid for discontinuous formulations). A total error is defined from individual error estimators as the sum over all elements

$$e = \left(\sum_{i=1}^{I} (e_i)^n \right)^{1/n} . \tag{5.2}$$

Computing the error based on the energy norm is a standard procedure in h-adaptivity schemes used in FEM. Another measure of error, particularly common in displacement-based FEM using C^0 shape functions, is the quadratic norm of the traction jump across element boundaries (excluding the boundary edges of the mesh) due to the discontinuity of stress components across neighboring elements [8]. A simple yet effective approach when considering a phase-field model for fracture is to consider not the gradient of displacement (proportional to stress) but the gradient of the phase-field variable across element boundaries. Element boundaries near the crack tip (where refinement should occur to accurately capture crack propagation) exhibiting high phase-field gradients are, thus, refined, based on the following computation of the element error:

$$(e_i)^n = \sum_{k=1}^{N_K} l_k \left\| \Delta d_i \right\|^n . \tag{5.3}$$

The total error is evaluated by Eq.5.2 substituting $n = 2$ and the expression 5.3. Elements with an error above a fraction of the average value e will be refined,

$$e_i^2 \geq \alpha_{ref} e^2 \tag{5.4}$$

where α_{ref} is the coefficient defining the refinement threshold. Conversely, elements staged for coarsening obey the following inequality:

$$e_i^2 \leq \alpha_{coar} e^2 \tag{5.5}$$

where α_{coar} is the coefficient defining the coarsening threshold. Since the history variable used in the free energy functional depends on the full history of the simulation, storage of its spatial values is incompatible with mesh coarsening. For this reason, mesh coarsening was disabled for all simulations. A typical value used for α_{ref} is $\alpha_{ref} \approx 0.8$. However, the parameter should be carefully chosen according to the physical significance of the variable in use, especially if there exists a high variance associated with error observations e_i. The models employing h-adaptivity presented hereafter all use as error estimator the gradient of d across element boundaries. This strategy is supported by choosing an initial mesh for which convergence was obtained for a simpler problem involving the same geometry and excluding the phase-field problem. Each refinement step consist in dividing the initial 'master' element into 2^D equal 'child' elements, where D is the problem dimension. (4 and

8 new elements are created for 2D and 3D problems, respectively). The value attributed to each variable at new nodes is computed by interpolation of existing nodal values using the shape functions adopted in the FEM model. This procedure is also employed for quantities computed at quadrature points.

Solution methods used for numerically solving the FEM equations

Similarly to classical computational mechanics solving algorithms, a linearized model of the FEM non-linear Eq.5.17 is considered to solve iteratively for each solution vector $\mathbf{s}^{n+1}$ by performing a first-order Taylor series expansion about the last iteration point. The new solution at iteration v, $\mathbf{s}_v^{n+1}$, is obtained by considering [72]

$$\begin{aligned} \mathbf{s}_{v+1} &= \mathbf{s}_v + \Delta\mathbf{s} \\ &= \mathbf{s}_v - \frac{\mathbf{r}\left(\mathbf{s}_v, t^{n+1}\right)}{\mathbf{J}} \end{aligned} \tag{5.6}$$

where $\mathbf{r}$ is the residual vector, and $\mathbf{J} = \frac{\partial \mathbf{r}}{\partial \mathbf{s}}$ is the Jacobian matrix. Here, $\mathbf{J}$ is the equivalent to the tangent stiffness matrix found in computational mechanics problems, and can also be called a tangent *virtual* stiffness matrix (*virtual* due to the fact that $\mathbf{s}$ contains the phase-field variable). The iterative process must be stopped by evaluating one criterion. Commonly used criteria are [72] (1) magnitude of the residual $\mathbf{r}$, (2) magnitude of the update in the solution, $\Delta\mathbf{s}$, and (3) the energy error (using some definition of error). Ambati et al. [11] affirm that the quantity to control convergence of a decoupled solving scheme is the total energy of the system (E_v), and address the issue of choosing an appropriate definition of a functional $f\left(E_v\right)$ to be compared with a user-defined tolerance. For fully coupled Newton iterations, the L_2 residual norm [72]

$$||\mathbf{r}||_{l_2} = \left(\sum_{a=1}^{Ndof} \mathbf{r}_a^2 \right)^{1/2} \tag{5.7}$$

where *Ndof* is the number of degrees of freedom, can be used to check for convergence at the end of each iteration. When considering multi-fields coupled problems, or even phase-field coupled with solid mechanics, the order of magnitude of $||\mathbf{r_i}||$ varies significantly for different fields i which can lead to unreal convergence difficulties if residual vectors associated with fields of different nature are evaluated without appropriately scaling their values.

The tangent virtual stiffness matrix in *conservative equilibrium problems*, for which the solution is obtained by

$$\min \Pi(\mathbf{s}) \text{ subject to Dirichlet/Neumann boundary constraints} \tag{5.8}$$

is called the *Hessian matrix* [72] $\mathbf{J} = \frac{\partial^2 \Pi}{\partial \mathbf{s} \partial \mathbf{s}}$ and the linearized form of the non-linear system of Eqs leads to its corresponding expression for $\mathbf{r}_v$

$$\frac{\partial^2 \Pi}{\partial \mathbf{s} \partial \mathbf{s}} \Delta\mathbf{s} = -\mathbf{r}_v. \tag{5.9}$$

Expression 5.9 degenerates into expression 4.27 for phase field models for brittle fracture. Note that the Hessian matrix is a function of d for coupling and displacement field terms ($\boldsymbol{K_{uu}}$ and $\boldsymbol{K_{ud}}$). Consider also that full Newton schemes require a full evaluation and inversion of the Jacobian (or Hessian matrix for conserved systems) at each iteration; the method can only achieve its typically observed[1] quadratic convergence and robustness if [72] (1) the Jacobian matrix is a smooth function of the solution vector $\mathbf{s}$ and (2) $\mathbf{J}$ is invertible and well-conditioned in the entire domain. Since the phase field variable exhibits significantly high gradients near developed cracks the condition (1) is significantly hard to fulfill - it can be achieved at very high computational costs by increasing the level of mesh refinement - leading to slow convergence rates and/or decreased robustness. Furthermore, a full evaluation and subsequent inversion of the Jacobian at each iteration also increases the computational cost of the model, which can be achieved by only evaluating the full matrix at the beginning of each iterative procedure, with subsequent evaluations occurring only when a lack of convergence is observed. However, the problem of robustness persists, and alternatives employing so-called Quasi-Newton solves have been proposed by some authors (see, for instance, [73]). A different approach to solving the system of linearized equations is to use the (Pre-conditioned) Jacobian-free Newton-Krylov (PJFNK) method [74] that uses a finite difference approximation of the Jacobian. Hales et al. [74] identified some of the advantages of using JFNK to solve complex problems involving a multi-fields framework: quadratic convergence can still be achieved without actually evaluating the Jacobian, it is a fully coupled approach and does not rely upon fixed point iterations (staggered schemes), and does not require loose coupling between fields, leading to good results in multi-fields scenarios. The solution vector Δs is obtained at each iteration by computing the finite difference approximation

$$\mathbf{J}\left(\mathbf{s}_v\right)\mathbf{b} \approx \frac{\mathbf{r}\left(\mathbf{s}_v + \varepsilon\mathbf{b}\right) - \mathbf{r}\left(\mathbf{s}_v\right)}{\varepsilon}. \tag{5.10}$$

Preconditioning can be added by defining a preconditioning matrix $\mathbf{M}$ [74] and solving

$$\mathbf{J}\left(\mathbf{s}_v\right)\mathbf{M}^{-1}\mathbf{w} = -\mathbf{r}\left(\mathbf{s}_v\right) \tag{5.11}$$

for $\mathbf{w} = \mathbf{Mb}$. Using an appropriate preconditioning matrix the condition number of the system may be decreased [74] due to the local character of shape functions and especially for multi-fields models exhibiting a high number of null coefficients of mutual influence in the tangent virtual stiffness matrix. Results obtained using PJFNK and JFNK for nonlinear solid mechanics alone or coupled with heat conduction in solid medias [74] provided mixed results in terms of computational performance compared to a Newton solve. Another important aspect for choosing the type of solve is the degree of coupling between all physics involved in a problem. Tight and loose coupled multiphysics are considered by either solving each individual physics separately, keeping the solutions for the remaining physics fixed at each iteration, or by simultaneously solving all equations at each iteration, considering all residuals when checking for convergence [75]. Examples usually given for the former are thermo-, electro- and chemo-mechanical problems with no contact involved, where a one-way coupling exists - thermal expansion leads to the appearance of eigenstrains. The best solution scheme to employ is highly dependent on the physics of

[1] This is the case, for instance, for linear elastic Quasi-static processes

each problem, and evaluating which leads to better performance is a difficult task since for smaller, less complex problems a fully coupled Newton method provides us with faster iterative procedures, while for problems with more computationally expensive Jacobians preconditioning of the system or the JFNK method may reduce computational time and, on the other hand, more complex multi-fields problems may require changing a fully-coupled system to a loosely-coupled one by employing a staggered scheme. Considering the multitude of solution techniques to solve multiphysics problems available, and considering results reported in the literature, three different solution schemes were used to solve the phase field models for brittle fracture presented hereafter. Namely, the systems of equations involving phase field coupled with mechanics,

- fully coupled, or monolithic Newton solve schemes were used as the default approach,

$$\mathbf{J}\mathbf{s} = -\mathbf{r} \tag{5.12}$$

- followed a preconditioned Newton solve,

$$\mathbf{J}\mathbf{M}^{-1}\left(\mathbf{M}\mathbf{s}\right) = -\mathbf{r} \tag{5.13}$$

- after which a JFNK iterative solution was considered (with or without preconditioning),

$$\mathbf{J}\left(\mathbf{s}_v\right)\mathbf{M}^{-1}\mathbf{w} = -\mathbf{r}\left(\mathbf{s}_v\right) \tag{5.14}$$

- and if results lack numerical robustness or lead to inconsistent results, the monolithic scheme was abandoned and loosely coupled iterations were considered,

$$\begin{bmatrix} \mathbf{J_{uu}} & \mathbf{J_{ud}} \\ \mathbf{J_{du}} & \mathbf{J_{dd}} \end{bmatrix} \begin{Bmatrix} \mathbf{s_u} \\ \mathbf{s_d} \end{Bmatrix} = - \begin{Bmatrix} \mathbf{r_u} \\ \mathbf{r_d} \end{Bmatrix} \tag{5.15}$$

  where each solution vector $\mathbf{s_u}$, $\mathbf{s_d}$ is computed while holding the other constant.

Preconditioned systems of algebraic equations

The FEM model implemented takes advantage of the phase-field and so-called Tensor Mechanics[2] modeling capabilities of MOOSE, and agrees with the multi-fields framework presented in chapter 3 proposed by Miehe et al. [51]. The driving force considered is the one typically adopted for brittle fracture,

$$\tilde{D} = \frac{2\psi^{+}(\varepsilon)}{\mathcal{G}_c/l} \tag{5.16}$$

Even though a Quasi-Static process is assumed, Eq.4.24 was considered, including the rate-dependent term, here recast as a viscous regularization stabilizing the numerical solution [55]. Two different displacement-phase field stiffness matrices were

[2]Here, Tensor Mechanics refers to FEM models with governing equations based on the elasticity theory

considered by defining the non-diagonal terms or setting them to zero. Accordingly, the system of equations in 5.17

$$\left\{ \begin{array}{c} \mathbf{R_u} \\ \boldsymbol{R_d} \end{array} \right\}_t = \left[\begin{array}{cc} \boldsymbol{K_{uu}} & \boldsymbol{K_{ud}} \\ \boldsymbol{K_{du}} & \boldsymbol{K_{dd}} \end{array} \right] \cdot \left(\left\{ \begin{array}{c} \boldsymbol{u} \\ \boldsymbol{d} \end{array} \right\}_t - \left\{ \begin{array}{c} \boldsymbol{u} \\ \boldsymbol{d} \end{array} \right\}_{t+\Delta t} \right) \tag{5.17}$$

takes into account off-diagonal terms for computing the residual vector $\mathbf{R}_t$ while the system of equations 5.18

$$\left\{ \begin{array}{c} \mathbf{R_u} \\ \boldsymbol{R_d} \end{array} \right\}_t = \left[\begin{array}{cc} \boldsymbol{K_{uu}} & 0 \\ 0 & \boldsymbol{K_{dd}} \end{array} \right] \cdot \left(\left\{ \begin{array}{c} \boldsymbol{u} \\ \boldsymbol{d} \end{array} \right\}_t - \left\{ \begin{array}{c} \boldsymbol{u} \\ \boldsymbol{d} \end{array} \right\}_{t+\Delta t} \right) \tag{5.18}$$

is obtained by neglecting those terms, leading to a symmetric matrix ideal for the numerical treatment of the model [76]. Using a Newton-type solve, and if provided, the full matrix given in expression 5.17 is considered to obtain the new solution vector, while using the PJFK method naturally leads to discarding off-diagonal matrix elements $\boldsymbol{K_{ud}}$ and $\boldsymbol{K_{du}}$.

Post-processor

Postprocessing was obtained using *in-situ* postprocessing [65]. This in-situ postprocessing capability allows a permanent tracking of the evolution of a model. For instance, if the qualitatively solution for a problem is known *a priori* (such as the crack path for a phase field fracture model) the value of d at a specific location may be monitored to check the physical consistency of the results obtained. All values computed by the post processor at the end of each time step were stored in a csv file for further data acquisition and graphical representation.

Reaction forces R_i at fixed boundaries were computed by considering the sum of nodal residual forces across the boundaries,

$$\mathbf{R} = \mathbf{f}_{\text{ext}} - \mathbf{f}_{\text{int}} \tag{5.19}$$

where the the vector $\mathbf{R}$ stores all components R_i according to the dimension of the problem.

Continuously monitoring the apparent stiffness (measured considering a linear behavior from unloaded to current loaded configurations, which is never the actual behavior for the AT-2 model, and current load at the support provided a valuable tool for immediate comparison with benchmark problems.

Chapter 6

Model validation

The model implemented and described in chapter 5 was validated by comparing with several benchmark problems typically studied in the literature. Taking into account the key advantages of phase field models - capacity to model brittle fracture, crack initiation as a consequence of stress concentration, and crack propagation - and also the main difficulties of theses models - slow convergence and low robustness of the optimization problem due to non-convexity of F, fine discretization near the damaged zone, imposing anisotropic fracture behavior during tension and compression - several force-displacement curves will be analyzed for each test considered. Nomenclature followed hereafter agrees with the one used for phase field models of fracture throughout section 2.7 and standard notation used in solid mechanics, as summarized in table 6.1. Furthermore, if no color legend is explicitly provided, red and blue colors indicate the highest and lowest field values. For visual plots involving the phase field, regions in red and blue indicate fully damaged and pristine material, respectively, and intermediate colors can be seen in the diffusive region surrounding crack surfaces. Table 6.2 summarizes the parameters necessary to define the discretization with h-adaptivity which are common to all models.

Table 6.1: Nomenclature for Solid Mechanics parameters

Symbol	Parameter
E	Young's modulus
ν	Poisson's ratio
G	Shear modulus
λ	Lamé's first parameter
μ	Lamé's second parameter (equivalent to the shear modulus)
Δu	Displacement increment at each load step
P	Peak load obtained from a force-displacement curve
K	Stiffness measure from a linear or Quasi-linear force-displacement curve
U	Displacement at peak load

Table 6.2: Meshing parameters

Parameter	Value
h_0	initial mesh size
h_{lvls}	Max No of h-adaptivity refinement levels from initial mesh
α_{ref}	Coefficient defining the threshold for refinement
α_{coar}	Coefficient defining the threshold for coarsening

6.1 SENT - Single-edge notched tension test

In what follows, a Single Edge Notched Tension (SENT) test using the phase-field model coupled with elasticity is considered according to the test configuration shown in Fig.6.1 and the model parameters summarized in Table 6.3. The test performed allows us to study the ability to predict crack paths during propagation, and the peak load and stiffness obtained for notched specimens under a remote tensile load. In spite of its simplicity, the SENT test has become a classical validation step in phase field models and its good convergence rate allows the understanding of the effect of using different Jacobian matrices for solving the algebraic system of FEM equations, coupling iteration schemes, and discretization techniques. A pre-existing crack was modeled by imposing an initial condition on the phase field variable and the test is performed under displacement control conditions with the displacement applied to the entire top edge. Benchmark results were retrieved from [11], where results were obtained for a phase field model using strain energy decomposition and staggered solving scheme with 8 staggered iterations, and will be referred to as *benchmark* hereafter.

Table 6.3: Model and material parameters for the SENT test

Parameter	Value
a (mm)	0.5
l (mm)	4.0e-3
λ $(kNmm^{-2})$	121.15
μ $(kNmm^{-2})$	80.77
$\mathcal{G}_c(kNmm^{-1})$	2.7e-3
Δu_1 (mm)	1e-5
$u_{\Delta u=1 \rightarrow \Delta u=2}$ (mm)	5e-3
Δu_2 (mm)	1e-6

6.1.1 Monolithic solution

A model considering strongly coupled iterations was developed using h-adaptivity refinement based on the gradient jump of d. The initial mesh was determined by first solving the same test using only linear elasticity and no initial crack assuming that the level of refinement demanded by the existence of ∇d is sufficient to accurately capture the local strain energy. The initial mesh thus obtained is considerably coarse. As an example, the initial and final meshes obtained using 8 levels of refinement are shown in Fig.6.2. The initial mesh was obtained after performing initial h-adaptivity steps based on the gradient of d_0, the initial crack phase field value. Considering also the final mesh shown in Fig.6.2b it is clearly shown that the task of discretizing the domain based on the current gradient of d can provide a powerful tool to model notched specimens if used correctly. Moreover, discretization errors influencing the direction of crack propagation are minimized since no *a priori* information concerning an expected crack path was considered. A volumetric/deviatoric strain energy decomposition was chosen.

Figure 6.3 shows the crack field at the (6.3a) initial stage and (6.3b) final load step. The initial edge crack propagated as expected for SENT tests of isotropic plates and results for a fully cracked plate were obtained. The force-displacement

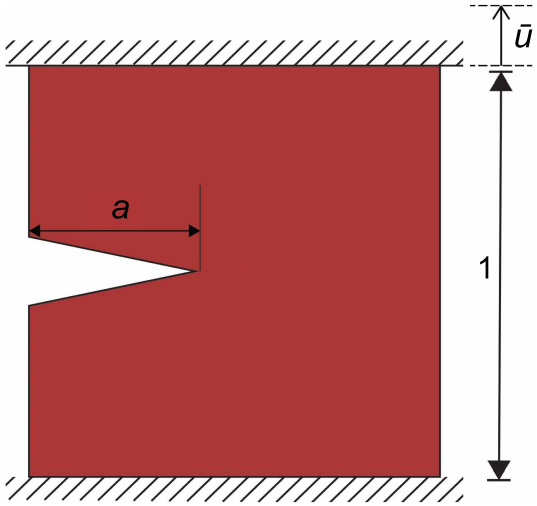
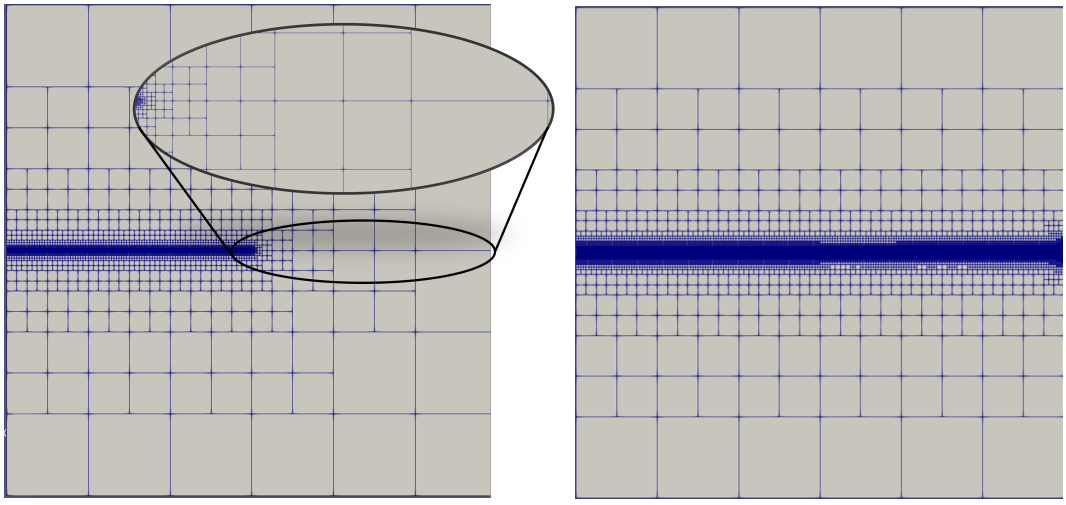


Figure 6.1: SENT test configuration. Adapted from [2]

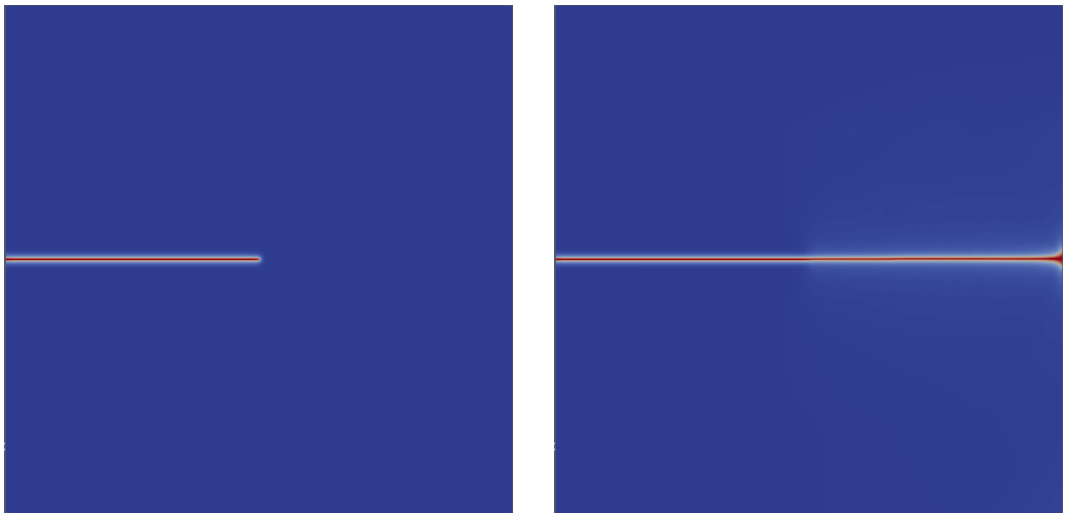


(a) Initial h-adapted mesh based on d_0, with $h_{lvls}^{max} = 8$

(b) Final mesh

Figure 6.2: SENT mesh using h-adaptivity

curve and the set of peak values (P, K, U) obtained are presented and compared to the benchmark result in Fig.6.4 and Table 6.4. The results obtained for the monolithic model are in good agreement with the benchmark case, especially the peak load obtained. A higher stiffness ($\approx$ 3%) was observed for the latter and, consequently, the crack begins to propagate at a slightly smaller displacement U. The most significant difference between both curves is the post peak load decay. The monolithic solution exhibits a smoother softening (or less brittle) behavior than obtained in [11] indicating a deviation from the result expected for Griffith's brittle fracture model.



(a) Specimen with initial notch (b) Cracked specimen after final load step

Figure 6.3: Crack field at (a) initial and (b) final load steps.

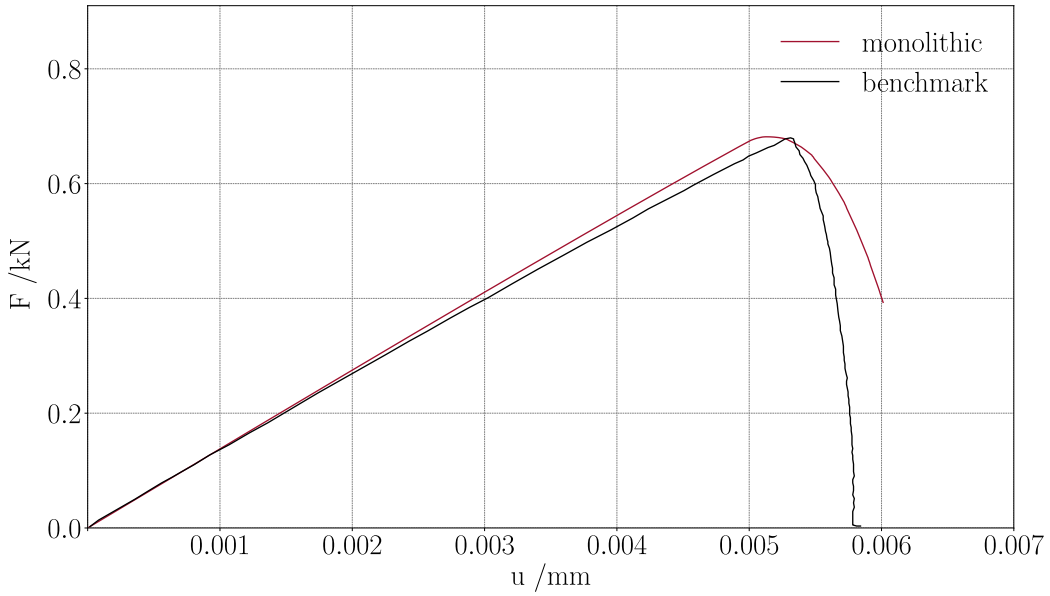


Figure 6.4: SENT test results: load-displacement curves for monolithic solution

Table 6.4: Peak values (U,P) and stiffness comparison between benchmark and monolithic results for the SENT

Parameter	Benchmark	monolithic	Difference (%)
P (kN·10^{-1})	6.80	6.82	0.29
K (kNmm^{-1})	128	133	3.91
$U \cdot 10^{-3}$ (mm)	5.31	5.12	3.58

6.1.1.1 Effect of initial mesh size and h-adaptivity levels

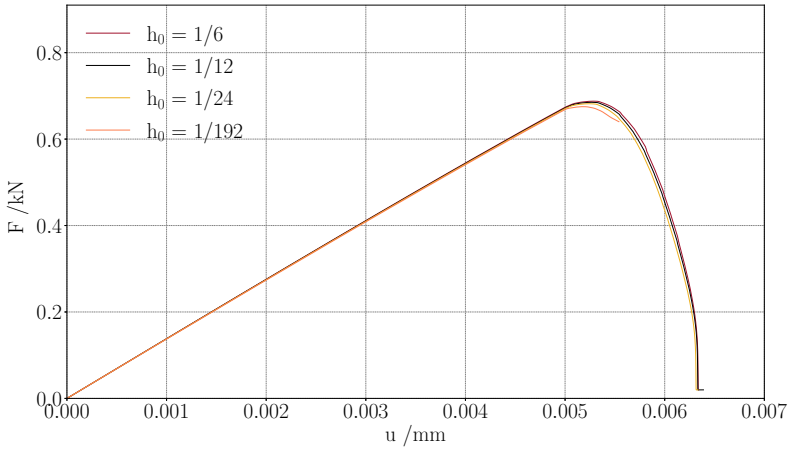
In this section, the influence of the initial mesh size h_0 and adaptivity parameters on the curve and crack propagation is studied. Fig.6.5 shows curves for models exhibiting different minimum element sizes and adaptivity based on the scaled residual norm of the coupled problem. Fig.6.6 shows a similar study involving a continuous increase of the maximum refinement obtained by controlling the parameter h_{lvls}^{max}.

Initial element size Due to the high number of mesh parameters used for the discretization of the domain, the effect of varying each parameter on the force-displacement curve was studied. Fig.6.5a shows results for different values of h_0 and fixed $h/l = 1.62E-1$, a value low enough to focus the study on the effect of decreasing h_0 (and, consequently, increasing h_{lvls}). The curves obtained are practically coincident for both linear and softening regimes, and a negligible maximum relative difference in stiffness measured with respect to the most compliant response was obtained ($\approx$ 0.43%. On the other hand, the time required to obtain a solution for the heaviest model (smallest value of h_0) can be reduced by more than 73% if the less computationally expensive discretization ($h_0 = 1/6$) is employed.

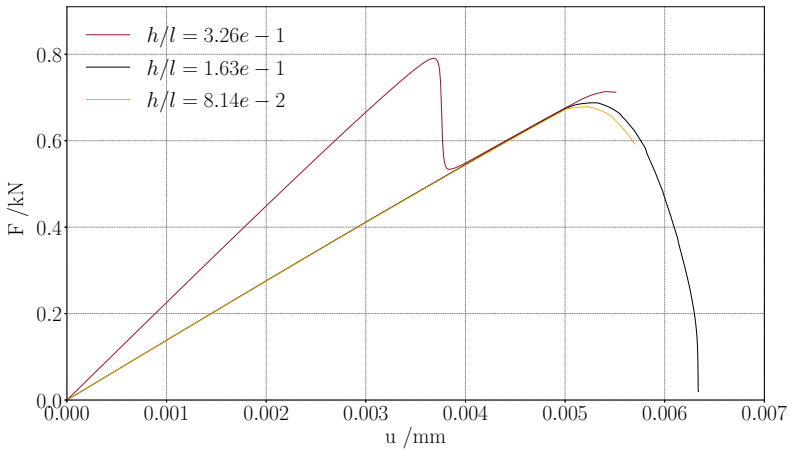
Maximum h-adaptivity levels Fig.6.5b shows results for different meshes obtained by varying the value of h_{lvls} and maintaining an initial mesh size of 6x6 elements. Given the algorithmic coupling between both field, h-adaptivity was based on the total scaled residual norm. For a value of $h_{lvls} = 7$, the ratio between minimum element size (obtained at the crack region) is $h/l = 3.26E-1$, and subsequent ratios are obtained by increasing refinement to 8 and 9 levels, respectively. Contrary to the initial mesh size, the value of h/l produced a significant influence on the curve obtained. For the less refined model, an unphysical snap-back effect is observed (instead of an approximately linear behavior) before the crack propagates. Conversely, a less significant change in response between the intermediate and most refined model is observed.

6.1.1.2 Effect of refinement threshold

Besides the dependency on mesh initial size and maximum levels of refinement studied above, the average element size h_{avg} and element size at damaged elements h_{min} are also controlled by a third parameter introduced in chapter 5: the refinement threshold α_{ref} used to identify which will be included during the next mesh adaptivity. Fig 6.6 shows different force-displacement curves obtained by varying its value from 0.8 to 0.04. The results obtained clearly show the importance of establishing an appropriate value for α_{ref} enabling an adequate adaptivity scheme near the crack region. In fact, for larger values of this parameter, it is seen that the



(a) Different initial mesh size h_0



(b) Variation of h_{min}/l by increasing h_{lvls}

Figure 6.5: Mesh size effects on SENT test force-displacement curve

expected propagation may not occur, leading to an overestimation of P (no softening was obtained before the maximum displacement considered). Moreover, for the intermediate value $\alpha_{ref} = 0.5$, propagation occurred for significantly larger values of displacement, and the peak force was largely overestimated. Convergence of the results was obtained for the value $\alpha_{ref} = 0.04$ corresponding to the curve used for comparison with the benchmark result. Given the visible difference between peak forces in Fig. 6.6, the values obtained for P and U are summarized in Table 6.5. For increasingly refined meshes, both values decrease until convergence is achieved. Furthermore, the error obtained with respect to the most refined result is essentially the same for P and U, which can be qualitatively assessed by the negligible difference in stiffness observed in Fig. 6.6.

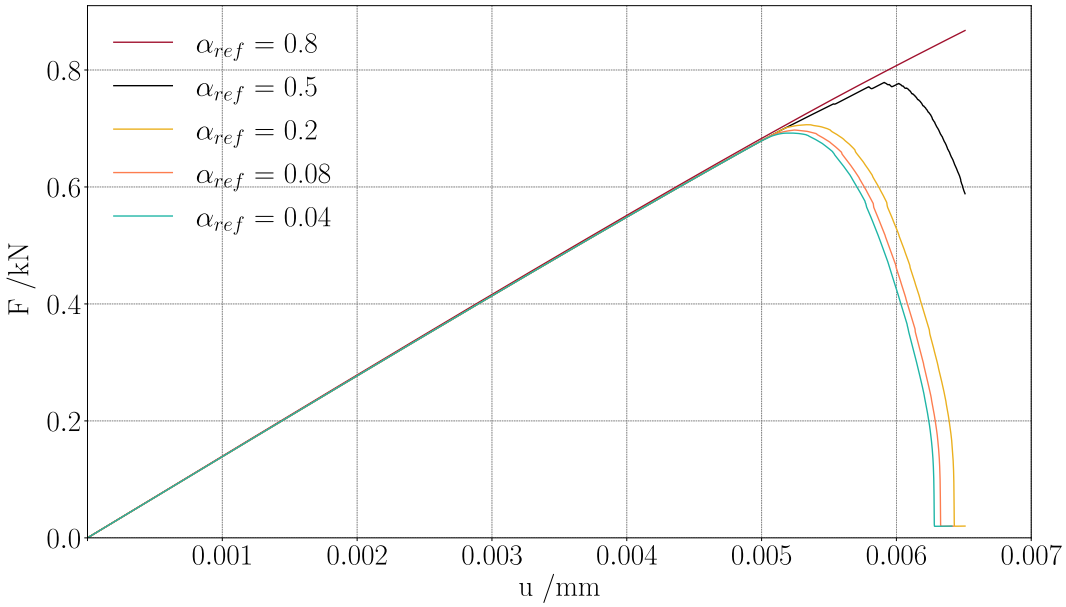


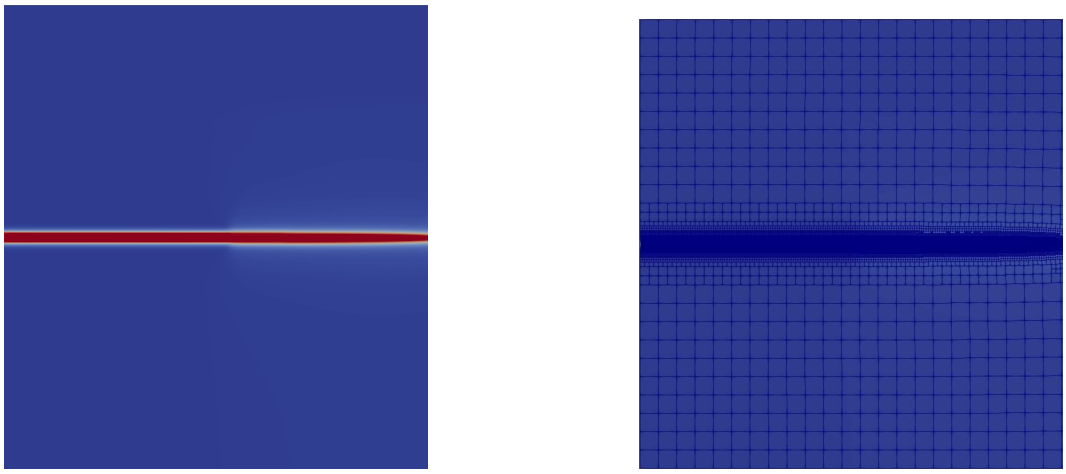
Figure 6.6: Effect of refinement threshold on the force-displacement curves

Table 6.5: Peak values (U,P) obtained for monolithic simulations of the SENT using different values of α_{ref}

α_{ref}	Final $\bar{h}$	P (kN·10^{-1})	Error (%)	U (mm·10^{-3})	Error (%)
0.5	3.79e-3	7.79	13	5.91	13
0.2	3.36e-3	7.06	2	5.33	2
0.08	2.73e-3	6.97	0.7	5.24	0.6
0.04	2.09e-3	6.92	-	5.21	-

6.1.2 Staggered solution

To understand the effect of using different algorithm schemes to solve the SENT problem a staggered solution for the same problem above described was obtained. Fig. 6.7a shows that the predicted crack path is in good agreement with the result obtained for the monolithic solution. Given the decoupling between the elasticity and phase-field problems, the energy error norm was now used instead of the residual norm to check for convergence of Jacobi-type coupled iterations by setting a relative tolerance of TOL $= 1e-6$. The final mesh, shown in Fig. 6.7b, is in good agreement with the monolithic case and the expected mesh topology for a SENT. A comparison between force-displacement curves obtained for the monolithic, staggered, and benchmark results is presented in Fig. 6.8. It can be seen in Table 6.6 that the staggered solution leads to a more similar result for the pre-peak region of the curve. However, the post-peak behavior for the same model is even less abrupt than what is obtained using the monolithic model. This unexpected behavior may be caused by the tolerance criterion adopted; an additional study should be conducted to study the influence of the convergence parameter TOL on the post-peak curve. Another interesting approach would be to fix the number of staggered iterations for each simulation and guarantee that convergence can be obtained using



(a) Crack path (b) Final mesh obtained

Figure 6.7: SENT simulation using a staggered scheme: (left) crack path and (right) final mesh topology. Displacement scale factor = 2

sufficient iterations.

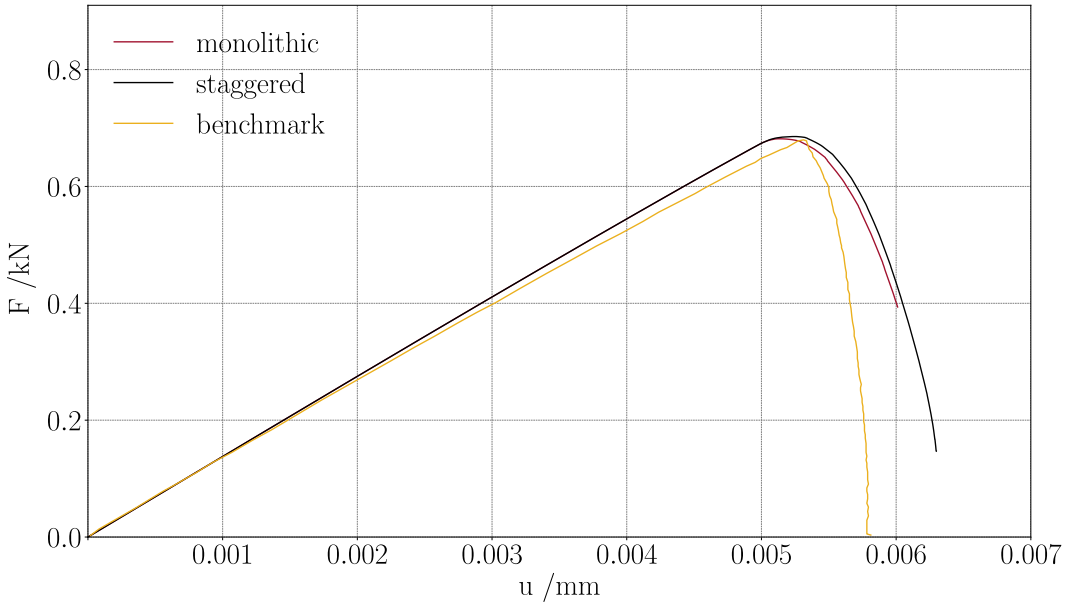


Figure 6.8: SENT test results: load-displacement curves for monolithic and staggered solution

Table 6.6: Peak values (U,P) and stiffness comparison between benchmark, monolithic and staggered results for the SENT

Parameter	Benchmark	monolithic (% Benchmark)	staggered (% Benchmark)
P (kN $\cdot 10^{-1}$)	6.80	6.82 (0.29)	6.85 (0.74)
K (kNmm^{-1})	128	133 (3.91)	130 (1.6)
U (mm $\cdot 10^{-2}$)	5.31	5.12 (3.58)	5.26 (0.94)

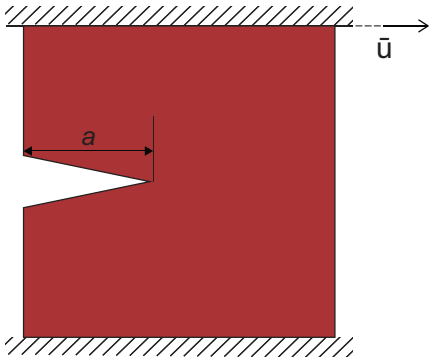


Figure 6.9: SENS test configuration.

6.2 SENS - Single-edge notched shear test

Using the same parameters defined in Table 6.3 with a fixed displacement increment $\Delta u = \Delta u_1$ for the SENT model a Single-Edge Notched Shear test (SENS) was simulated to understand how the model behaves under mode-II loading, which is closely related with the strain energy decomposition used[1]. The boundary conditions prescribed are shown in Fig. 6.9 and the benchmark result was also taken from [11].

6.2.1 Monolithic solution

The force-displacement curve obtained for the SENS simulation using a monolithic algorithm scheme is shown in Fig. 6.10. A less significant difference between benchmark and monolithic results was obtained in terms of maximum load and apparent stiffness. These values are shown in Table 6.7. Moreover, the post-peak softening behavior obtained is in good agreement with the benchmark result and the progressive stiffness degradation typically observed for a mode-II loading condition.

[1]The same volumetric/deviatoric decomposition used for the SENT was here adopted

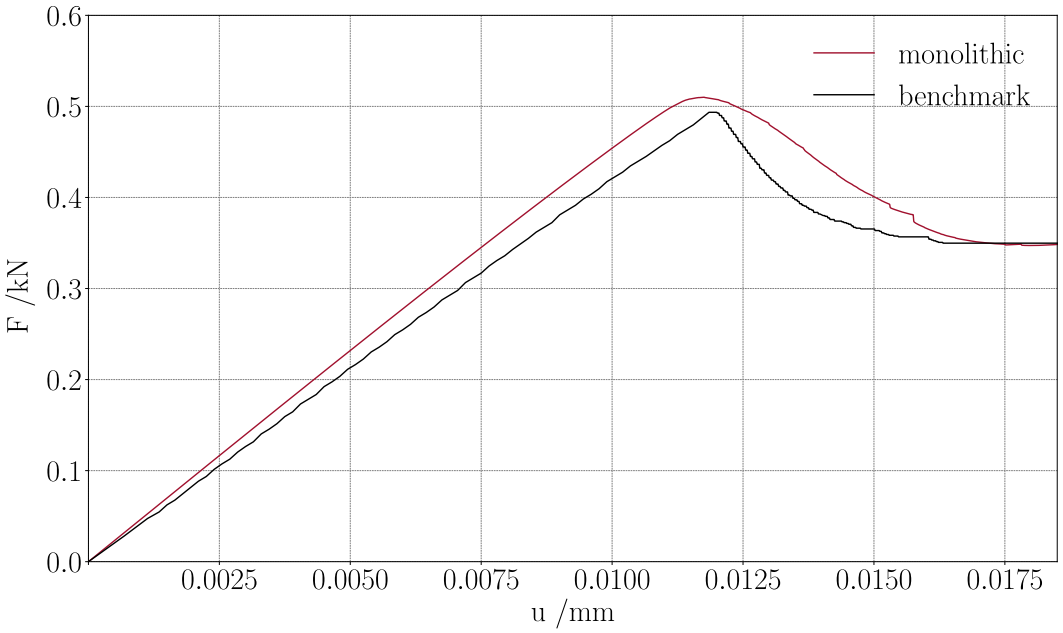


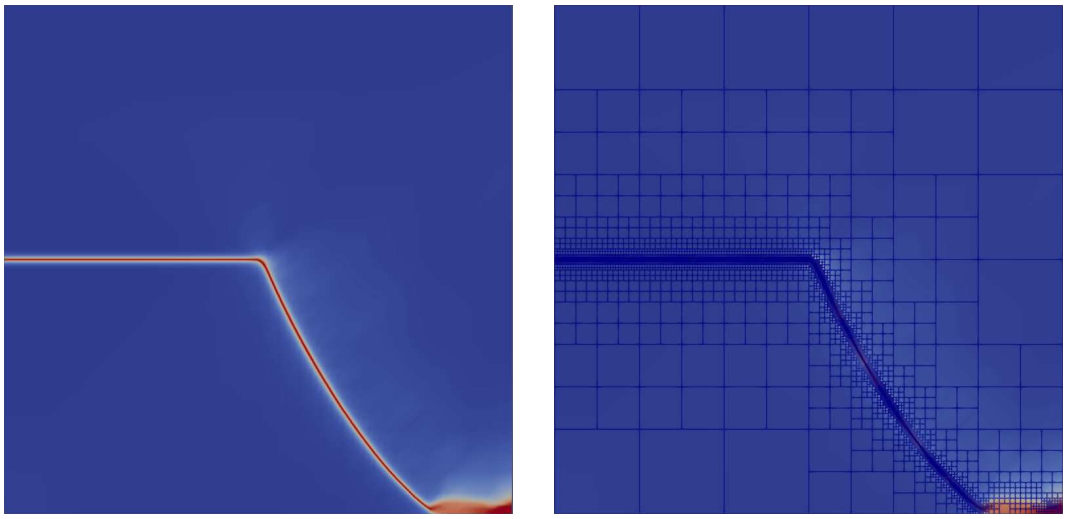
Figure 6.10: SENS test results: load-displacement curves for monolithic solution

Table 6.7: Peak values (U,P) and stiffness comparison between benchmark and monolithic results for the SENS

Parameter	Benchmark	monolithic	Difference (%)
P (kN $\cdot 10^{-1}$)	4.9	5.1	4.1
K (kNmm^{-1})	42	43	2.3
U (mm $\cdot 10^{-2}$)	1.19	1.18	0.8

6.2.2 Crack path prediction for mode-II loading

The final (6.11a) crack path and (6.11b) h-adapted mesh obtained for the SENS simulation are illustrated in Fig. 6.11. The ability to predict the oblique crack path relying on h-adaptivity instead of a pre-existing local refinement of the discretization is, once again, highlighted. Furthermore, the unphysical crack branching phenomenon found for phase-field models using inappropriate (or non-existent) strain energy decomposition was successfully avoided.



(a) Final crack path (b) Final mesh

Figure 6.11: Monolithic SENS test crack path and mesh for the final load step

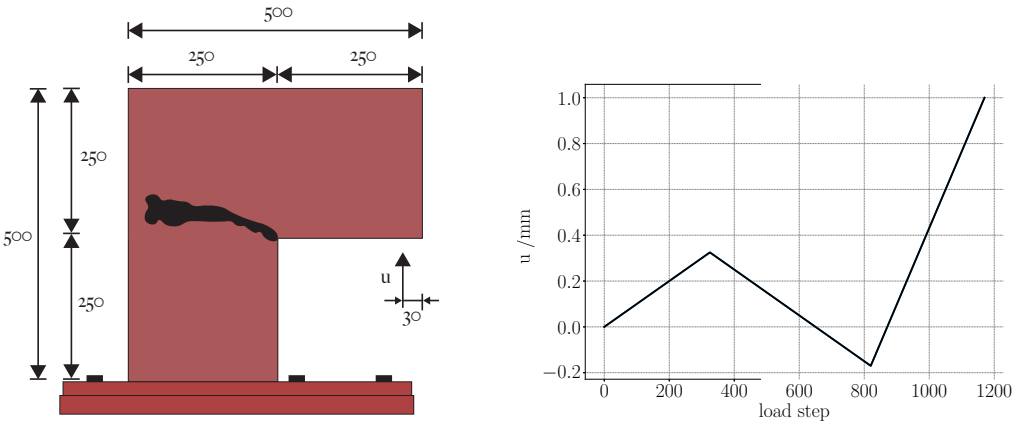
6.3 L-shaped panel test

In spite of their apparent simplicity, the SENT and SENS test provide a robust analysis methodology to detect common pitfalls encountered when modeling brittle fracture with phase-field models. Both are standard fracture mechanics tests of fundamental importance to predict crack growth in materials for which the K-dominance zone size is sufficiently large [77].

The successful use of phase-field fracture models should also depend on the ability to predict crack initiation and subsequent propagation in unnotched test specimens. To study the performance of the model here proposed when modeling such fracture phenomenon the L-shaped panel test depicted in Fig. 6.12a was considered, where the (approximate) expected crack pattern based on experimental observations [11] is included. For the boundary conditions and geometry tested, it is the effect of stress concentration near the inner right angle, where the maximum tensile stress is expected to occur, that should lead to crack initiation. Additionally, the same load reversal conditions used in [11] will be applied to study crack closure and consequent stiffness recovery phenomena. A cyclic displacement-controlled loading of $|\Delta u| =$ 1e-3 mm is imposed according to Fig. 6.12b. The material and model parameters considered are shown in Table 6.8 and a volumetric/deviatoric decomposition was considered.

6.3.1 Monolithic and staggered results

The test obtained in [11] using the anisotropic formulation and spectral decomposition will be used as the benchmark result for validation. The force-displacement curve obtained with the monolithic and staggered schemes are compared with those for [11] in Fig. 6.13. The evolution of the crack field with the load steps is shown in Fig. 6.14. Using an initially uniform mesh and h-adaptivity, the crack pattern is



(a) Configuration tested. Adapted from [78]

(b) Cyclic loading history

Figure 6.12: L-shaped panel test definition

Table 6.8: Model and material parameters for the L-shaped panel test

Parameter	Value
l (mm)	1.1875
λ $(kNmm^{-2})$	6.16
μ $(kNmm^{-2})$	10.95
$\mathcal{G}_c(kNmm^{-1})$	8.9e-5
$\lvert\Delta u\rvert$ (mm)	1e-3

in close agreement with results obtained in [11] and the experimental observations mentioned in the same work. The peak load obtained for the current model in both algorithm schemes is fairly larger than for the reference curve considered. An explanation for this substantial difference has not yet been obtained but the decrease in peak load from the monolithic to the staggered solution seen in Fig. 6.13 indicates that it could be attributed to the algorithmic approach (usage of monolithic iterations and insufficient staggered iterations)[2]. Ongoing studies will help clarify if the behavior seen in the reference work is obtained by increasing the number of staggered iterations, or, conversely, the increase of maximum load is only attributed to expected discrepancies between distinct modeling strategies. Table 6.9 provides further insight into the results obtained by comparing P, U, the apparent stiffness measured at the peak, K_t, and the stiffness in compression, K_c. Both monolithic and staggered models were able to accurately capture the effect of stiffness recovery and prevent crack face interpenetration.

[2]The residual error norm and energy error norm were used to check for convergence of the monolithic and staggered models, respectively. A value of TOL $= 1{\cdot}10^{-6}$ was used for the staggered scheme

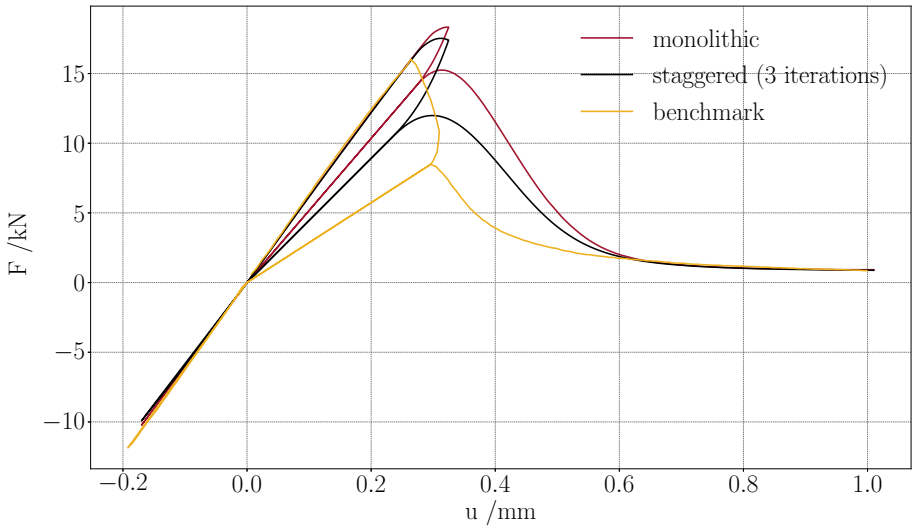
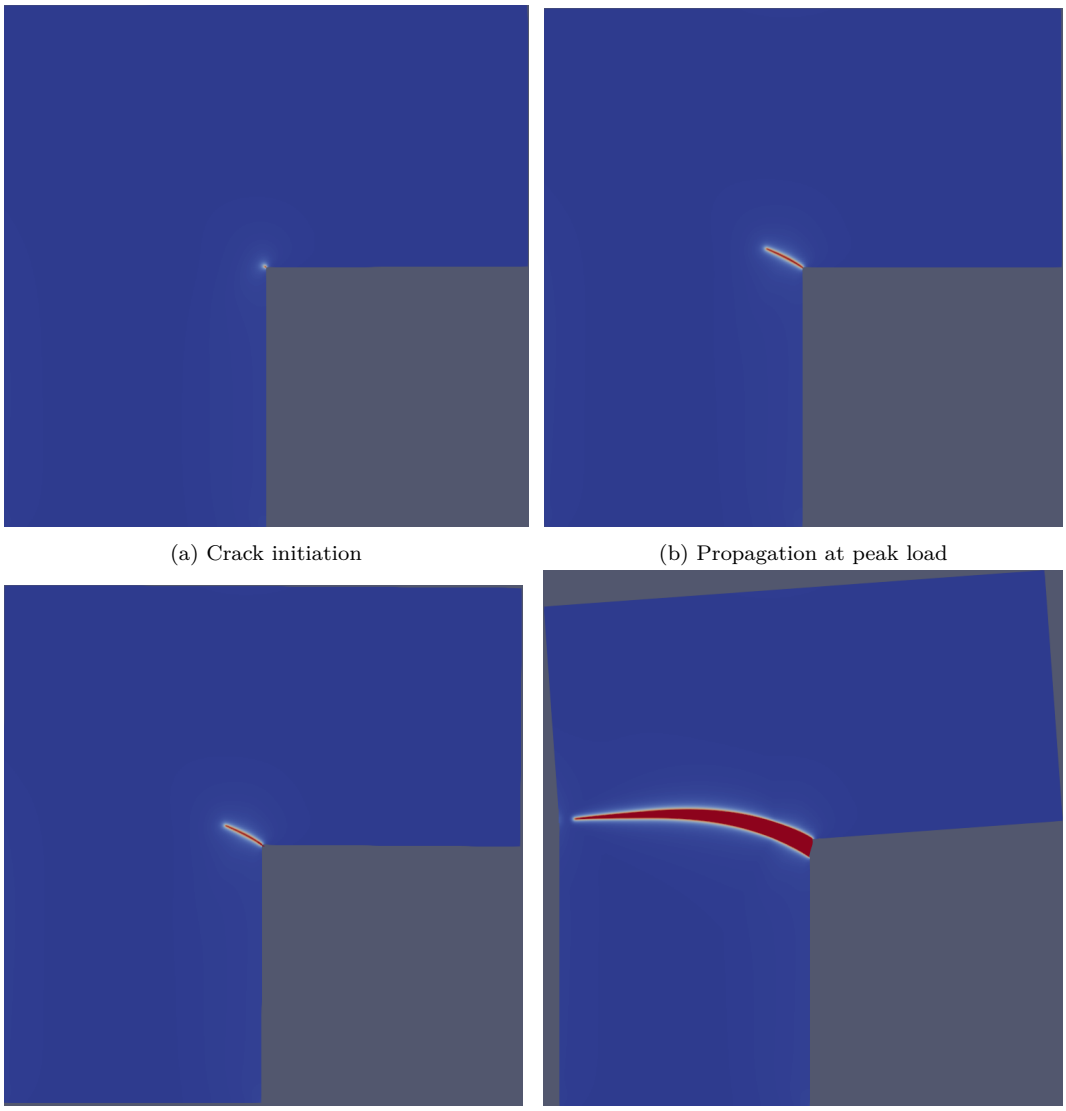


Figure 6.13: Force-displacement curve for the L-shaped panel test

Table 6.9: Peak values (U,P) and stiffness comparison between benchmark, monolithic and staggered results for the l-shaped panel test

Parameter	Benchmark	monolithic (% Benchmark)	staggered (% Benchmark)
P	16.02	18.32 (14)	17.52 (9)
U (mm $\cdot 10^{-1}$)	2.64	3.25 (23)	3.12 (18)
K_t (kNmm^{-1})	61	56 (8)	56 (8)
K_c (kNmm^{-1})	62	60 (3)	58 (6)
K_t/K_c	0.98	0.93	0.97



(a) Crack initiation

(b) Propagation at peak load

(c) Minimum displacement (10x scale factor)

(d) After softening

Figure 6.14: Evolution of cracks for the l-shaped panel test

6.4 Concluding remarks

Three classical phase-field benchmark tests - SENT, SENS, and l-shaped panel test - were simulated using the model adopted in this work. For the linear elastic fracture mechanics tests (SENT and SENS) crack propagation and crack path in displacement controlled loading conditions were accurately captured using monolithic iterations and a staggered coupling scheme for the former. The pre-peak curve obtained is in very good agreement with the benchmark result considered. A post-peak softening response was obtained for the SENT instead of an abrupt load drop typical in mode-I brittle fracture. Future works should provide solutions to improve the failure of these specimens. Conversely, the post-peak curve obtained for Mode-II loading conditions is in close agreement with the benchmark case. From the results obtained for the l-shaped panel test, it was concluded that the model is also able to capture crack phenomena for unnotched specimens with local stress concentration effects and under the more complex cyclic loading condition. While crack initiation and propagation were successfully captured for tensile loading, crack face interpenetration was avoided due to the strain energy decomposition used. Moreover, this was achieved by effectively modeling crack closure since no crack healing occurred throughout the entire load history.

Even though some discrepancies between benchmark results and tests performed in this work still require further validation studies, overall good agreement with validated results were observed and the fairly good description of crack phenomena were attained, which gives us confidence to simulate multi-field coupled fracture problems.

Chapter 7

Coupled thermo-mechanical SENT model

7.1 Introduction

The coupled problem modeling capabilities of the work developed are hereby tested using a simple transient heat conduction problem. A simple illustrative example built by adding a temperature field to the SENT model discussed in chapter 6. The effect of continuously degrading the thermal conductivity of a solid with an active crack phase-field is studied as well as the influence of thermal expansion on the stress state, crack propagation, and the force-displacement curve obtained.
In spite of the physical meaning attributed to the coupled temperature field, the results provided may also be interpreted as a more general coupling between phase-field fracture and a simple diffusion problem within the framework discussed in section 3.3 of chapter 3. Nevertheless, studying thermal effects in fractured media (and vice-versa) is an important topic especially for ferroelectric-based battery cells showing electrostatic and electro-chemical properties highly dependent on thermal conditions [79]. The thermal and model parameters required to model transient heat conduction are defined in Table 7.1

Table 7.1: Nomenclature for Heat transfer parameters

Symbol	Parameter
k	thermal conductivity
α	linear thermal expansion
C	specific heat capacity
ρ	Density
T_0	Initial temperature
T_i	Constant temperature prescribed at boundary i
$T = T(t)$	Time-dependent temperature prescribed at the boundary

7.2 SENT test with time-dependent heat conduction

To understand the effect of heating a single-edge notched plate while performing the same SENT test described in chapter 6, heat conduction without heat generation across the test specimen was studied and introduced via prescribed temperature and adiabatic boundary conditions, as seen in Fig. 7.1. The thermal properties and model required to reproduce the model are given in Table 7.2. A constant velocity of 1 mm/min for the first part of the test was considered to ob-

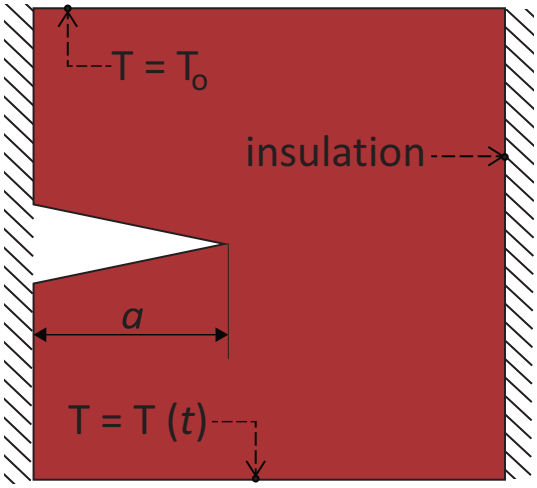


Figure 7.1: Thermal boundary conditions for the SENT heat transfer problem

tain its corresponding time increment. Moreover, given that no real-life problem was modeled, thermal properties for aluminum alloys were arbitrarily considered. A monolithic algorithm was used to solve the problem which leads to a strong coupling between the crack phase-field and the displacement field equations. Furthermore, due to the one-way coupling framework adopted, the thermal field is loosely coupled with the remaining ones in spite of the algorithm scheme.

Table 7.2: Model and material parameters for the SENT with heat transfer test

Parameter	Value
k (W·mm^{-1}·K^{-1})	251·10^{-3}
α (K^{-1})	23.5·10^{-6}
c (J·kg^{-1})·K^{-1}	1050
ρ (kg·mm^{-1})	2.7·10^{-6}
T$_0$ (°C)	21
T(t) (°C)	$5t \cdot 10^{-3}$
Δt (s)	6·10^{-4}

Results and Discussion

To study the effect of thermo-mechanical coupling caused by thermal expansion force-displacement curves for the SENT heat transfer problem with and without thermal expansion is shown in Fig. 7.2. It is highlighted that the models without expansion and purely mechanical possess slightly different curves due to the change in h-adaptivity introduced by the temperature field. The significant increase on peak force seen for the thermal expansion model is further described in Table 7.3. This effect was attributed to the change in local strain state caused by the thermal expansion of the solid since the stiffness essentially remains unchanged. Recall that heterogeneous expansion occurs with higher expansion values below the notched region. The vertical displacement u_y and thermal fields obtained at the time step for initial crack propagation observed for the non-expanding plate are represented in

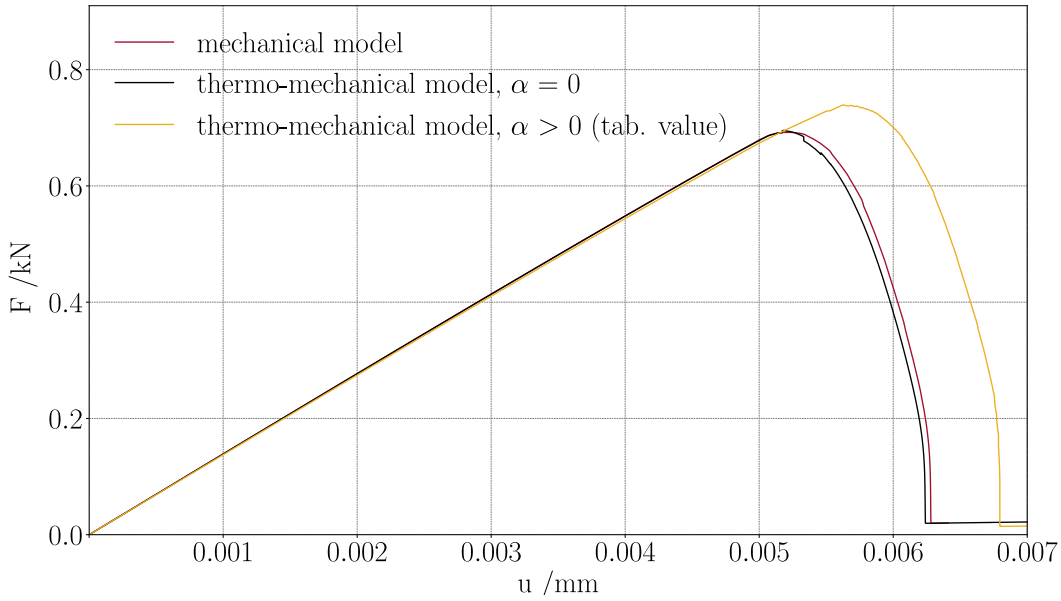
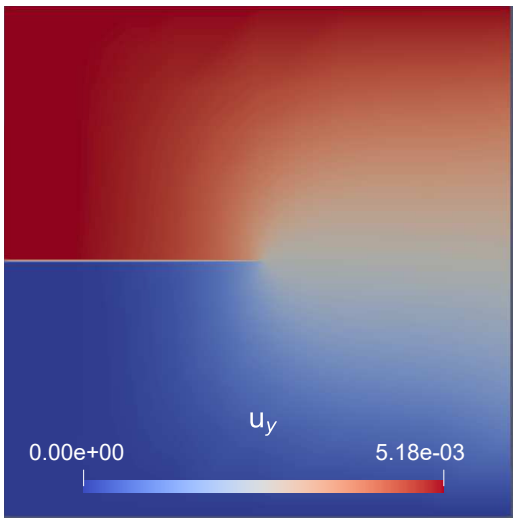


Figure 7.2: Effect of thermo-mechanical coupling on the force-displacement curve for the SENT heat transfer problem.

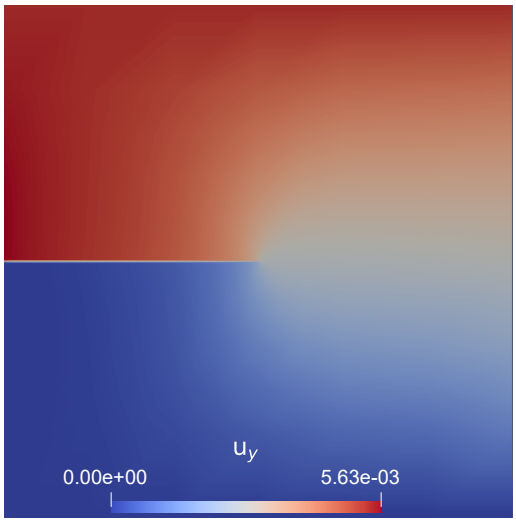
Fig. 7.3. Furthermore, the model was able to capture the effect of stress and heat flux spatial evolution with an evolving crack tip. Fig. 7.5 and Fig. 7.4 show the respective fields for initial crack propagation and the final load step before full crack propagation.

Table 7.3: Peak values (U,P) and stiffness comparison for the SENT heat transfer problem with and without thermo-mechanical problem

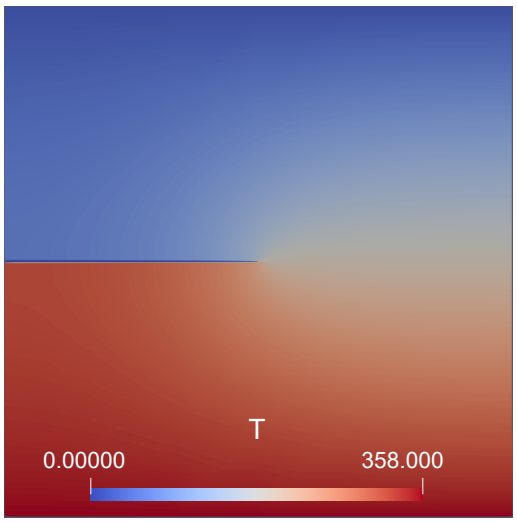
Parameter	Model		Difference (% α=0)
	α=0	α>0	
P (kN $\cdot 10^{-1}$)	6.95	7.39	6.3
K (kNmm^{-1})	134	131	2.2
U (mm $\cdot 10^{-3}$)	5.18	5.63	8.7



(a) α=0 model: u_y

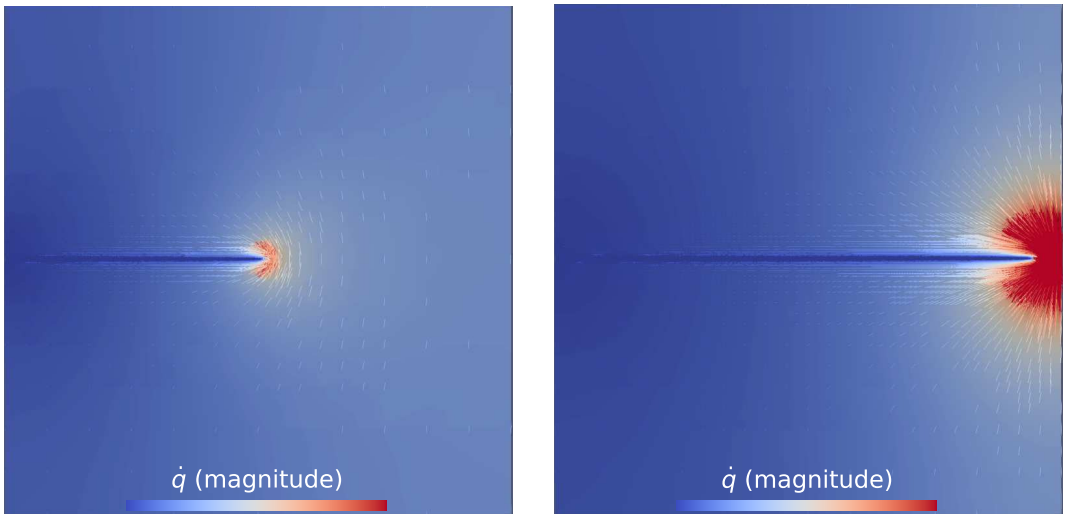


(b) Model with thermal expansion: u_y



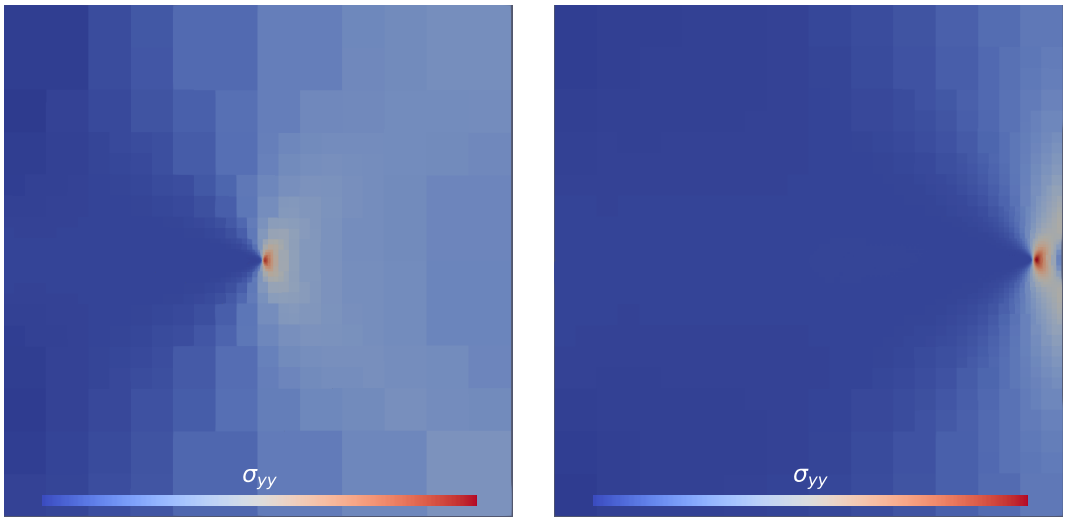
(c) Temperature field

Figure 7.3: Vertical displacement (u_y) and temperature field for the load step prior to initial crack propagation.



(a) At the start of crack propagation (b) Load step prior to full propagation

Figure 7.4: Heat flux concentration near the crack tip



(a) At the start of crack propagation (b) Load step prior to full propagation

Figure 7.5: σ_{yy} field near the crack tip

Part IV

Experimental work

Chapter 8

Flexural response of an all-solid-state structural beam-type battery

Tubular and cylindrical beam- and shell-type components are one of the most common structural elements used in vehicles and infrastructures. Tubular shapes are usually favored due to their cost and weight saving higher specific stiffness (with respect to weight). In terms of purely structural optimization, this has led to classical tubular design concepts such as the frame of a bicycle, automotive chassis, tubular fuselage, among others. For multi-functional materials such as a structural battery, cylindrical configurations may instead be considered to achieve system-level optimization of mass, structural, thermal and electrochemical performance and facilitate the manufacturing solution. In this chapter, an assessment of the structural performance of a novel cylindrical composite battery beam based on all-solid-state battery (ASSB) technology and thin-ply carbon fibre/resin prepregs is presented. The advantages of using ASSBs instead of liquid electrolyte batteries as the energy storage material are manifold and highlighted in [3, 4]: increased resistance against fire due to mechanical damage and overheating interaction, delayed degradation of electrochemical performance and increased structural properties of the composite battery, among others. To understand the effect of replacing the inner void for an electrochemically active coaxial material system on the mechanical response of a laminated tubular beam, three point bending tests are performed on laminated composite cylindrical beams. The same outer layup material system - produced from unidirectional *prepregs* of thin-ply carbon fibre/epoxy - is considered but with different inner layers of material - hollow shell and filled cylindrical configurations. Unlike other design concepts involving sandwich beam and plate geometries proposed for structural batteries [4], coaxial circular structural batteries were manufactured following the same procedure as described in [3]. To provide further insight into the deformation at structurally critical sections, all test were performed on specimens equipped with strain gauges aligned with the axis of principal stresses.

8.1 Introduction

The experimental work described in this chapter is part of a first series of mechanical tests aiming to provide qualitative and quantitative information regarding the mechanical response of a novel patented material system capable of withstanding mechanical loads while storing energy in the form of electric and chemical potentials. This patent provided an innovative cylindrical design approach to structural batteries for which plate, sandwich or tubular structures are usually proposed [80–

83]. Moreover, most of these concepts rely on liquid state or solid/liquid biphasic electrolyte systems that compromise safety against fire and electrochemical performance retention [5] and also exhibit a non-structural behavior.

The new approach to structural battery design is the outcome of two extensive review works focusing on the latest trends in electric vehicles batteries [5] and recent research on structural batteries [3]. With these review efforts, a complete picture of the performance requirements imposed by targeted real life applications was obtained and allowed to understand the electrochemical performance indicators that must be achieved to bridge the gap between an innovative and exciting multi-functional concept and industry-ready technologies. Since most design ideas for structural batteries consist in building multi-functionality from a starting structural element, the main engineering challenge faced is to achieve the desired specific energy and power, fast-charging, long lasting capacity retention and safe functioning of an energy storage system while retaining a mechanical behavior sufficient to meet vehicle industry required structural behavior. Results from previous three-point bending tests [3] already showed that the coaxial structural battery can in fact behave as a structure when loaded in bending. A beam battery was fabricated from a simple structure - tubular CFRP shell, a structural element used in vehicles such as lightweight electric bicycle - by embedding an ASS Na battery. Compared to the latter, the composite battery was able to sustain a higher peak load, achieved higher deformation before catastrophic failure, and showed increased flexural stiffness. Although simple solid mechanics principles predicted this effect for a bulk cylindrical beam fabricated from CFRP, this experimental evidence provided valuable insight into the validity of the design concepts, especially considering the existence of heterogeneous interfaces and the potential weakness that may arise from their presence in structural materials. However, further mechanical characterization is required to obtain a rigorous quantitative assessment of the beam battery; its realization is paramount to comprehend its potential weaknesses and desired improvements towards achieving the desired multi-functional behavior. In this chapter, three-point bending tests for the ASS coaxial structural battery using specimens fabricated outside the scope of the present work and following the same fabrication procedure as first proposed in [3] are presented. Strain gauges were used to measure the tensile strain at the central section where the load is applied. Force-strain curves of the multi-functional material are obtained for the first time. Moreover, a different cathode material from the one used in [3] providing superior chemical potential and with a chemical composition similar to what is found in electric vehicles batteries [5] was also tested. To understand the degree of electrochemical/mechanical coupling associated with the bending response of the beam batteries, the mechanical test was stopped and later resumed before the ultimate load to generate cyclic voltammetry curves.[1]

[1]Electrochemical analyses are out of the scope of this work.

8.2 Material characterization. Fabrication and configuration of test specimens

Fabrication and specimen geometry

In this work, three material configurations were used to study the flexural response of cylindrical beams of different cross-sections. The UD *prepreg* tapes were supplied by North Thin Ply Technology and fabricated using the T800-736LT 100 gsm carbon-epoxy prepreg [84]. The all-solid-state electrolyte synthesis, cell preparation using Aluminum and Copper negative and positive electrodes, respectively, and full structural cell assembly were previously made during a prior experimental campaign. The work published by Danzi et al. [3] describes the entire fabrication process required to obtain the multi-functional specimens used in this study. In addition to the same previous work, Aluminum foils coated with Lithium Manganese oxide ($LiMn_2O_4$) powder was used as a cathode material for cells. All three configurations have an exterior CFRP outer shell obtained by curing a quasi-isotropic $[90/0/+45/-45]_S$ laminate in a hot press at 80^{o}C for 8 hours. Two types of composite cells were obtained by using different cathode materials that were co-cured with the CFRP outer shell. Table 8.1 summarizes the three material systems tested. The geometry of each layer remains fixed for all three except for the absence a battery block for the CFRP outer shell control specimen. The structural batteries tested are distinguished by the cathode type: a Na^+/Li^+-ASSB configuration using $LiMn_2O_4$ as the cathode and Na^+-ASSB using copper as the positive electrode. Fig. 8.1 illustrates the shape and dimensions for the outer shell used in all specimens.

All specimens were instrumented with strain gauges in compliance with the manufacturer specifications. The strain gauges used were supplied by Micro-Measurements and positioned at the mid-length section and aligned with the longitudinal axis of the cylindrical specimens. Fig.8.1 exhibits the gauge location with respect to the specimens.

Table 8.1: Configurations tested for the three-point bending test

Configuration	Battery layers			
	CFRP sub-laminate[2]	Cathode	Electrolyte	Anode
CFRP shell (No.1)	$[90/0/+45/-45]_S$	-	-	-
Na^+-ASSB (No.2)	$[90/0/+45/-45]_S$	Copper foil	$Na_{2.99}Ba_{0.005}OCl$	Aluminium rod
Na^+/Li^+-ASSB (No.3)	$[90/0/+45/-45]_S$	$LiMn_2O_4$	$Na_{2.99}Ba_{0.005}OCl$	Aluminium rod

[2]carbon fibre/epoxy thin-ply

Table 8.2: Nominal dimensions of the battery components according to Fig. 8.1

Parameter	Battery layers			
	CFRP sub-laminate	Cathode	Electrolyte	Anode
R_0 (mm)	7	6.025	6	2
t (mm)	9.375e-1	6.25e-2	4	2
L (mm)	100	100	100	120

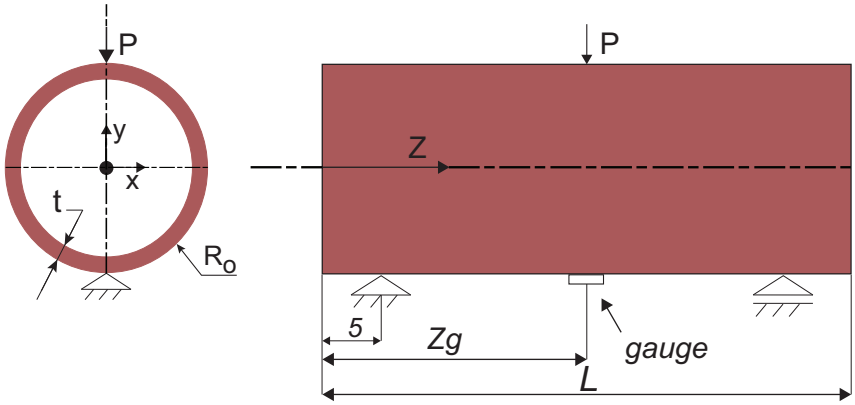


Figure 8.1: Simplified drawing of the outer shell and experimental setup for the beam battery bending tests. The hollow entire is completely filled for beam cell configurations

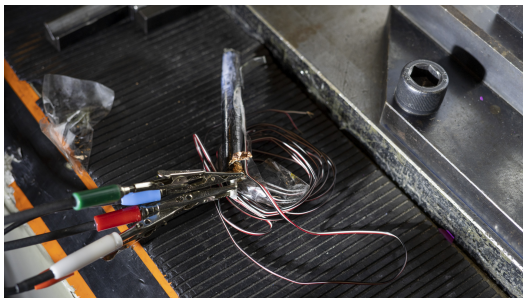
Experimental setup

The three-point bending test configuration depicted in Fig.8.1 and Fig8.2 provides a visual description of the experimental setup. The setup of the bending test started by fixing the center load cell using a bolted connection and positioning the bottom supports with the adequate distance from the point of load application and measuring the total span between end supports as shown in Fig.8.2a. The end tabs of the composite batteries were connected to a potentiostat according to Fig8.2b.

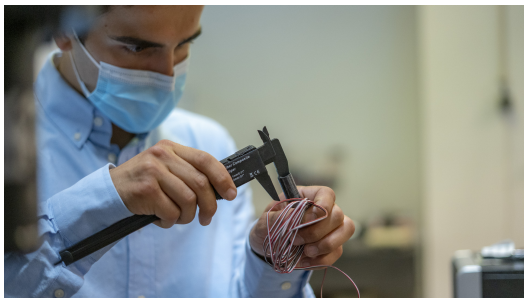
The tests were performed at a controlled speed of 2.0 mm/min, in an INSTRON 4208 electro-mechanical universal testing machine equipped with a 5 kN load cell and were interrupted twice to obtain cyclic voltammetry curves: once in the linear region for a prescribed load of 1 kN and after the peak load was obtained. For the electro-chemical test, the battery specimens were cycled between +0.5 and −0.5 V using a scan rate of 50 mV·s^{-1}.
Due to a shortage of fabricated specimens, one test per each configuration shown in Table 8.1 was performed. The total thickness and outer diameter of the specimens were confirmed by measuring their values with a carbon fibre caliper as shown in Fig.8.2c. The average values obtained from three measures per dimension and specimen are presented in Table 8.3



(a) Measurement of the span between supports



(b) Tabs connection to the potentiostat



(c) Measurement of specimens

Figure 8.2: Visual description of test setup and measurements

Table 8.3: Real cross-section dimensions of the three specimens

Measured dimension (Avg value)	CFRP outer shell	Na^+-ASSB	Na^+/Li^+-ASSB
d_o (mm)	ϕ11.8	ϕ14.23	-
t (mm)	1.17	1.0	-

8.3 Results and discussion

Force-displacement curves

In the previous experimental work (prev. work in subsequent figures) [3] experimental curves for three-point bending tests performed for the configurations No.1 and No.2 were obtained. Fig.8.3 combines these previously determined experimental curves with the results obtained for the three-point bending test performed for all specimens. The control configuration (CFRP outer shell) shows a similar response for both experimental tests. The initial non-linear response, attributed to the initial accommodation of the specimen and test equipment, is followed by a linear curve followed by a less significant non-linear response until the peak load is obtained. A visible small difference in stiffness (K) can be explained by a change in thickness (t) between shell specimens since its value is highly sensitive to this dimension ($K \propto t^3$ for shells). The peak load obtained agrees well with the past observation allowing the calculation of an average value. Moreover, the post-peak behavior is identical for both curves and clearly shows a steady load drop and stiffness degradation. A comparison between previous and current experimental results for the configuration Na^+-ASSB may also be done based on Fig. 8.3 taking into consideration that the

mechanical test was interrupted during the linear stage and after the peak load was recorded. A similar linear response with a slightly larger value of peak load, mainly attributed to the same thickness effect above reported aggravated by the more complex and less controlled battery cell fabrication process and the interruption step at the point of 1 kN measured force. The post-peak behavior obtained agrees well with that obtained in the previous work [3] and clearly shows a load plateau for increasing post-peak displacement. Considering the good agreement shown between both experimental works, the current work supports the results reported in [3]. For all beam battery specimens (configurations 2 and 3) the curves show not only an increase in bending stiffness but also significantly higher peak loads. Both results were expected following simple principles concerning the bending of beams. Moving from a hollow thin tube configuration to a composite cylindrical bulk section increases the second moment of area I about the neutral axis x of the bent beam, which proportionally increases the flexural rigidity (defined as the product of Young's Modulus, E, and I). Conversely, the post-peak behavior provides interesting results requiring a thorough phenomenological study of the failure mode obtained. In [3], the pseudo-ductile response shown for beam batteries, as opposed to the progressive post-peak degradation of both stiffness and load tolerance, was attributed to the compaction of electrolyte in the region above the neutral axis where a compressive stress state exists. Moreover, the existence of a solid section also prevents crushing and ovalization of the beam [3] which delays the final failure. However, the phenomena responsible for the structural non-linear behavior leading to a larger ability to dissipate energy, which occurs in a stable way, have not been clearly understood yet and still require further studies. Nonetheless, the change in failure mode represents an interesting and significant improvement to the structural behavior of the beam. In addition, an unexpected increase of peak load for the beam battery using $LiMn_2O_4$ powder as the cathode compared with that obtained for the Na^+-ASSB battery was registered. As also noted in [3], further quantitative analysis of the failure processes would require the nonexistent knowledge of the elastic properties of the electrolyte and fracture properties for the CFRP/Cathode/Electrolyte/Anode interfaces. However, the peak loads obtained may be calculated by taking the average result for configurations No. 1 and 2 and using the value obtained for the Na^+/Li^+-ASSB specimen. Table 8.4 shows the maximum loads obtained, total mass measured for each configuration, and respective specific maximum load values, three parameters typically used as indicators for the mechanical performance of structural batteries. In spite of the increase in maximum load obtained for the beam battery configurations, both show a significant decrease in specific peak load, $\bar{P}$ with respect to the tubular thin-ply beam. From a purely mechanistic and weight/cost optimization point of view, and assuming that the beam would be designed to withstand some prescribed load without yielding, the new structure would lead to degraded efficiency. Knowledge of its electrochemical performance is required to better understand the full performance of the multi-functional structure.

Force-strain curves

The force-strain curves measured for the three specimens are presented in Fig. 8.4 (refer to Fig. 8.1 for a visual depiction of the position used to measure strain). To focus the analysis on relevant strain information post-peak values were discarded

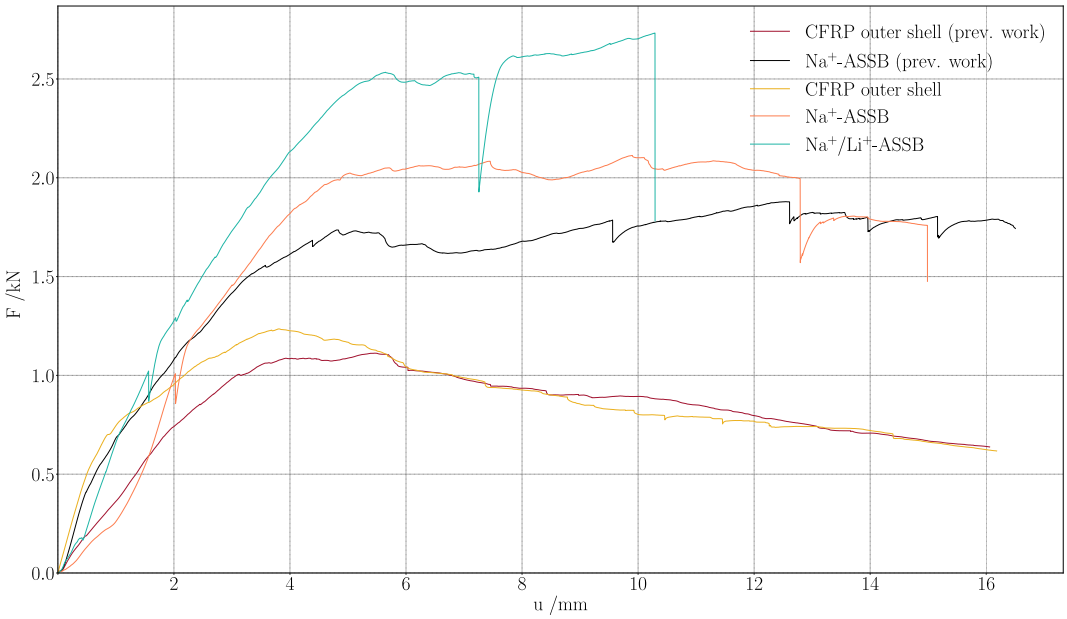


Figure 8.3: Experimental force-displacement curves obtained in previous (prev.) [3] and current three point bending tests

from the representation. Comparing with the force-displacement curve in Fig. 8.3, it is highlighted the clearly initial linear response indicating that the initial region of the force-displacement curve was significantly affected by irrelevant test setup effects. Moreover, a significant difference in the pre-peak zone between beam batteries was obtained, as the Na^+/Li^+-ASSB configuration exhibits a strongly linear curve up to the peak-load. To understand what caused the apparent change in pre-peak damage evolution, the specimens were visually inspected and a significant misalignment in the circumferential direction between the loading plane and strain gauge was observed, and the differences observed were attributed to the heterogeneity of the crushing and ovalization effect near the mid-section of tested specimens, as can be seen in Fig. 8.5. It was concluded that a comparison between the Na^+-ASSB battery and the CFRP outer shell is more appropriate since similar pre-peak curves

Table 8.4: Structural batteries and CFRP outer shell beams bending performance: peak load, P, mass, m, and specific maximum load, $\bar{P}$

Configuration		P (kN)	m (g)	$\bar{P} = P/m$ (kN·kg^{-1})	$\bar{P}/\bar{P}_{CFRP}$ (%)
CFRP outer shell					
	Previous work	1.11	6.40	173.4	-
	Current work	1.24	5.55	223.4	-
	Avg. Value	1.18	5.98	197.3 ($\bar{P}_{CFRP}$)	-
Na^+-ASSB					
	Previous work	1.87	21.60	86.6	44
	Current work	2.11	21.39	98.6	50
	Avg. Value	1.99	21.50	92.6	47
Na^+/Li^+-ASSB					
	Current work	2.73	21.58	126.5	64

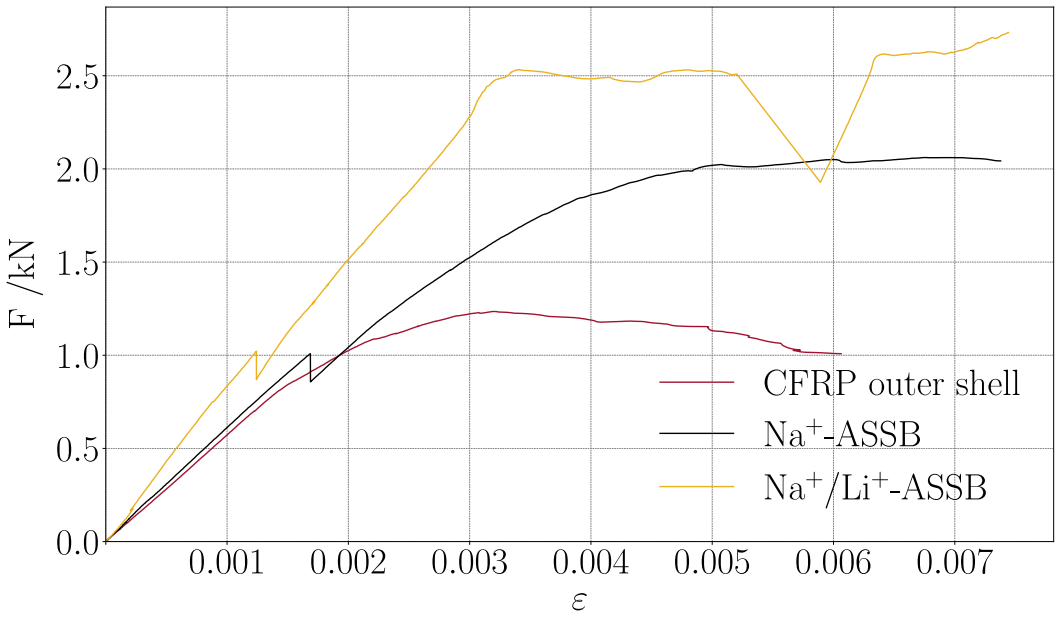


Figure 8.4: Experimental force-strain curves obtained for all three point bending tests

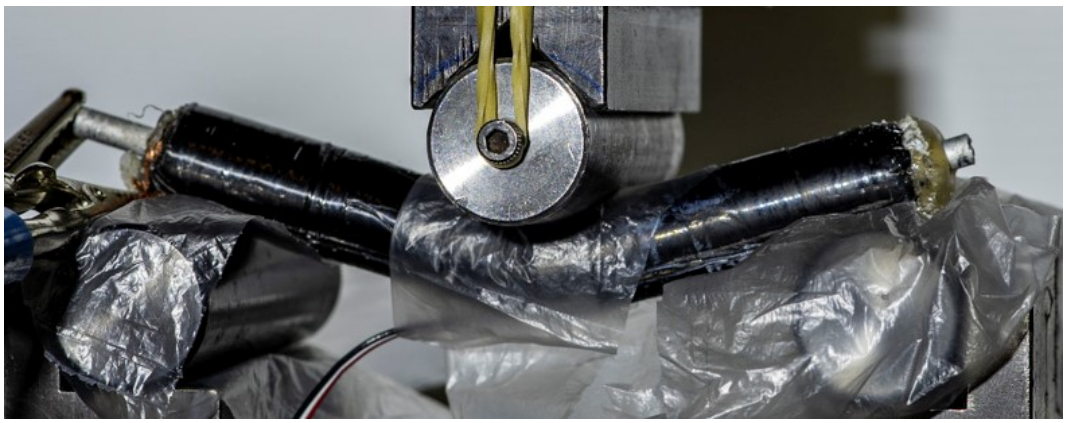


Figure 8.5: Mid-section ovalization due to the mechanical test of composite batteries

were obtained for both specimens: identical slopes were obtained for both configurations, which is consistent with the fact that strain is measured on the same outer 90 ° ply of thin-ply carbon fibre material (recall that for an Euler-Bernoulli beam the slope of a F/ε curve is proportional to the product between Young's modulus E and cross-section area of the outer ply). Moreover, similar damage onsets prior to the maximum load were obtained with the composite battery showing a significantly larger extent for this region, i.e., a relevant pseudo strain hardening effect increases the strain corresponding to the peak load for the Na^+-ASSB specimen.

System-level performance of the composite battery

Even though the specific energy E/V and energy density $\bar{E}$ for the two composite batteries tested have not been measured, these values may be estimated using the experimental data of performance indicators reported in [3] which is reproduced

in Table 8.5. A (very limited) mass comparison between a simplified traditional structure and its structural multi-functional counterpart will be presented hereafter.

Assuming that a specification is given for the total electrical energy the system must be capable to provide, E_{req}, and adopting the values of energy density provided for the cells as the reference for system-level battery design[3], the total mass required for each scenario is given by

$$m_i = \frac{E_i}{\bar{E}_i} \tag{8.1}$$

where subscript i denotes the structural battery (sb) or a traditional **b**attery sub-system. Knowledge of the value of mas of structural battery m_{sb} required allows us to estimate its structural performance. If we consider that the structure consists in a system of springs connected in parallel where each composite beam is modeled with a spring stiffness equivalent to the bending stiffness of the former, the maximum load capacity is simply given by the sum of the peak load that each beam withstands. Fig. 8.6 illustrates both traditional and multi-functional energy storage systems. Under these conditions and using values of $\bar{P}$ presented in Table 8.4 for the battery beams, the total load capacity for the multi-functional structure of mass m_{sb} is given by

$$P^* = \bar{P}_{sb} \cdot m_{sb} \tag{8.2}$$

where subscript *sb* denotes the composite beam battery configuration in Fig. 8.6b. The equivalent traditional structure would require a total mass of CFRP beams of $m_{CFRP} = P^*/\bar{P}_{CFRP}$ to withstand the same load. Combining this value with the mass required for the battery cells obtained using a traditional fabrication, the total mass of the system obtained may be compared with the mass of structural battery required by noting that

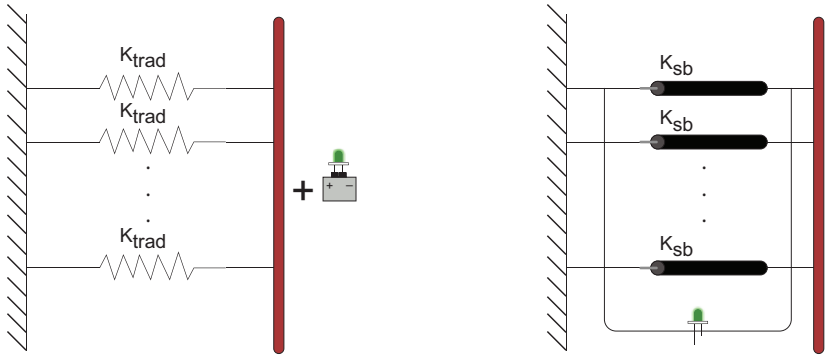
$$\begin{aligned} m_{CFRP} &= \frac{\bar{P}_{sb}}{\bar{P}_{CFRP}} m_{sb} = \alpha \cdot m_{sb} \\ m_b &= \frac{\bar{E}_{sb}}{\bar{E}_b} m_{sb} = \beta \cdot m_{sb} \end{aligned} \tag{8.3}$$

and summing the mass of both traditional sub-systems:

$$m_{sb} = \frac{1}{\alpha + \beta} m_{trad}. \tag{8.4}$$

The sum of the multi-functional efficiency coefficients α and β must exceed the value of 1 to reduce the mass of the total system. Table 8.6 shows the values obtained for α and β of both beam batteries tested using the average values for $\bar{P}$ provided in Table 8.4 and the values for $\bar{E}$ provided in Table 8.5. Given that no information regarding the energy density for configuration Na^+/Li^+-ASSB is known, its respective coefficient β was left undetermined. It can be seen that the configuration $Na^+ - ASSB$ practically achieved the same mass efficiency measured in terms of total energy and maximum admissible load. Moreover, this comparison did not take into account the change in failure mode observed for the composite battery, which is a significant improvement for structural applications.

[3]The energy density of battery packs is significantly lower than for battery cells



(a) Traditional multi-component system (b) Structural battery

Figure 8.6: Multi-functional vs traditional structural and energy storage systems

Table 8.5: Experimental data reported in [3] for the performance of the Na^+-ASSB composite battery

Parameter	Full Cell	Full Cell (No CFRP)
Specf. Energy (WhL^{-1})	56.2	76.3
Energy density, $\bar{E}$ ($Wh{\cdot}kg^{-1}$)	38.0	75.8

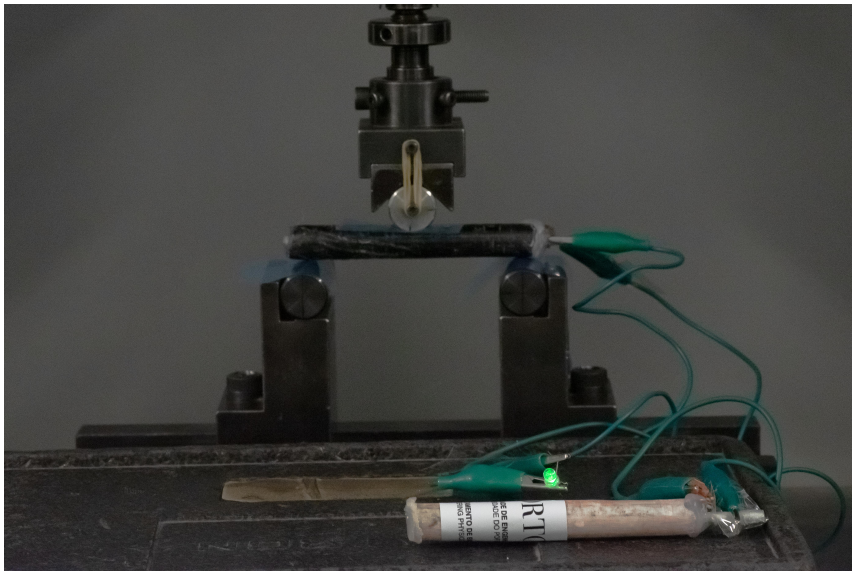
Table 8.6: Multi-functional performance of the structural batteries

Parameter	Na^+-ASSB	Na^+/Li^+-ASSB
α	0.47	0.64
β	0.50	Unknown
$\alpha + \beta$	0.97	-

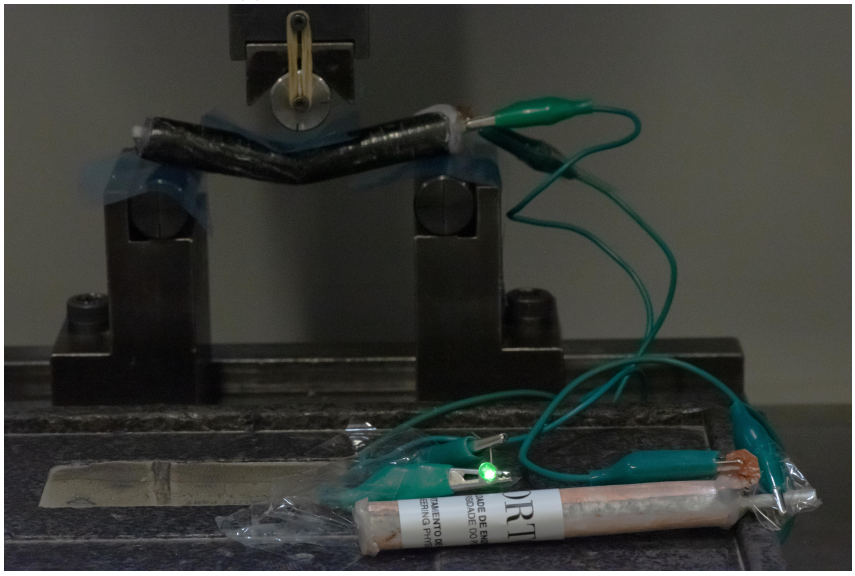
8.4 Concluding remarks

Composite batteries offer a set of conceptual advantages over traditional structures and batteries used in electrified systems. Achieving mass reduction via multifunctional design may be the disruptive technology that will shape future electric mobility solutions with a positive impact in the transports, automotive, marine, aeronautical, and aerospace industries. However, the state-of-the-art for these material systems is still far from developing industry-ready solutions.

A novel structural battery concept was presented and experimental three-point bending tests characterizing their bending response were here performed. The key differences over alternative composite batteries proposed in other works are the innovative circular beam design and advanced materials used: while the reinforcing structural element was fabricated using thin-ply carbon fibre/epoxy prepregs, the structural battery relies on an all-solid-state energy storage cell with a ferroelectric composite Na-glass electrolyte with enhanced thermal and electrochemical properties [79, 85, 86]. Besides being regarded as the next disruptive technological improvement for energy storage devices, solid-state cells provide a remarkable structural advantage over battery cells with liquid-phase electrolytes. The surprising synergistic effect of pseudo-ductile failure observed for the composite batteries is the best proof of the structural integrity here achieved. In spite of the mechanical tests conducted beyond the ultimate structural failure of these composite batteries, no electro-chemical failure was observed throughout the entire loading history. Moreover, to the best of our knowledge, this structural battery is the first of its kind that may be mechanically tested beyond its failure point with no occurrence of overheating or fire incidents, as can be seen in Fig. 8.7 for the experiment done in [3], where it is highlighted that the structural battery is still able to light a LED bulb after performing the three-point bending test up to failure.



(a) Before the three-point bending test



(b) After mechanical failure

Figure 8.7: Multi-functional test [3]: LED light bulb powered by a beam battery loaded in bending

Part V

Conclusions and future work

Chapter 9

Conclusions and future work

The main conclusions of the work presented in this thesis and clues for potential future developments are presented in this chapter.

9.1 Conclusions

9.1.1 Phase-field models to predict the failure of brittle materials

A phase-field numerical model to predict brittle fracture of solid media was implemented and validated by comparison with benchmark results in this thesis. The model formulation considered here was supported by a review of those recently proposed in the literature encompassing the entire formulation from Griffith's law and the variational statement for brittle fracture to the intricacies of their numerical implementation. Rather than seeking a novel approach to phase-field modeling, the strategy adopted here was to obtain a model capable of providing physically sound results and modeling complex fracture phenomena where the direcftion of crack propagation may not be known *a priori*.

To simulate fracture mechanisms such as crack initiation, crack propagation, stiffness recovery in compression, and the ability to prevent unphysical crack propagation due to compressive stress states, three of the most relevant validation tests for phase-field fracture models were performed: the single-edge notched tension test, the single-edge notched shear test, and the L-shaped panel test with load reversal after an initial crack propagation. A good agreement was found between the results obtained and those reported in the literature. Moreover, a careful sensitivity analysis was performed to study the influence of the discretization considered on the results obtained. It was seen that accurate estimation of crack propagation and initiation may be obtained without introducing *a priori* local mesh refinement based on prior knowledge that inevitably *guides* the results obtained towards some expected result. These facts indicate that the methodology presented here is a first step towards the simulation of novel materials or structures whose failure mechanisms are yet to be understood.

9.1.2 Coupled problems modeling

The proposed numerical framework was also coupled with the heat conduction problem following a so-called loosely-coupled coupling. A simple yet represen-

tative example for a single-edge notched tension test combined with a transient heat conduction simulation imposed by a prescribed increase in temperature at one of its boundaries. It was concluded that by simply degrading the thermal properties based on the phase-field variable the effect of thermal flux concentration near the crack tip can be captured. Additionally, the tensile stress state caused by a thermal expansion of the domain affects the force-displacement curve obtained for the test considered. These facts indicate that the coupling methodology presented here is a first step towards developing more complex problems involving the phase-field model for fracture and other diffusion problems.

9.1.3 Bending response of a coaxial structural battery

The effect of combining a tubular carbon fibre thin-ply beam with an all-solid-state battery cell to obtain a multi-functional structure on the structural performance was experimentally studied. The specimens tested were fabricated according to a patented coaxial structural beam battery developed within the scope of an ongoing project aiming to redefine the mechanical and energy storage design concept of electric mobility. Supported by previous experimental tests performed outside the scope of the work presented here, further mechanical characterization of these structural cells was obtained. In spite of the lack of experimental support to obtain a full quantitative mechanical characterization, the experiments reported here showed a promising improvement of the failure modes for the structural battery components: a pseudo-ductile response and larger displacement value at the peak load were obtained compared to the progressive load and stiffness drop registered for the carbon fiber tubular beam. Furthermore, and to the best of our knowledge, structural batteries were tested until ultimate mechanical failure without a complete loss of electrical performance, overheating or fire incidents. These facts strongly suggest the adequacy of solid-state technology for multi-functional structural integration.
To understand the potential for total mass reduction achieved with the structural batteries tested, calculations based on simplifying assumptions for total mass equivalence between a multi-functional system and mono-functional systems based on structural and electrical performance indicators was performed. It was concluded that (considering the simplifying assumptions made) the beam battery tested practically achieved the same mass efficiency as an equivalent traditional system, providing an optimistic initial reference for future multi-functional design optimization steps.

9.2 Future work

The phase-field brittle fracture model proposed should be further validated for other more complex test configurations and material systems of interest. Additionally, the model should be understood as a first step towards more evolved phase-field modeling of brittle fracture and some of engineering strategies from the literature adopted here require a careful revision and potential future improvements. Of particular importance is the definition of a more appropriate strain energy decomposition enabling a more sound connection between the local stress state and the crack driving force.
The coupled problems model here proposed should be further tested by considering

other diffusion problems such as the existence of species concentration, electrostatic or magnetic fields. The loosely-coupled strategy followed allows the introduction of several coupled phenomena with minimal impact on the mechanical base problem. Moreover, an appropriate validation strategy must be determined since no standard benchmark results exist for this class of problems.
Within the next decade, a significant leap in all-solid-state batteries performance and fabrication process is expected and will significantly upgrade present-day electrochemical energy harvesting systems. The composite beam battery tested is at an early stage of conceptual and material development. In spite of the promising structural response obtained for the configurations tested here, several other experimental tests should be performed to obtain a quantitative measure of its mechanical properties: the elastic properties of the electrolyte could be estimated using inverse parameter identification by fitting the experimental curve with numerical models simulating the bending tests performed; knowledge of the interfacial fracture properties is paramount to further investigate the failure modes highlighted in the discussion of the experimental results; and the fracture toughness of the electrolyte should also be determined. The three-point bending test performed must be the first step of a more ambitious experimental campaign that could aid the design of future structural power composites and material improvements. In addition to the material characterization, other structural battery concepts should be explored by taking into account some of the promising results found in the literature. Considering the unexpected character of the pseudo-ductile response obtained for the bending tests, new mechanically efficient structural cells may be created by simply combining the same materials in a different structural element shape such as a laminated plate.

Bridging the gap between the proposed analysis models and the experimental campaign for composite batteries
The connection between the experimental tests and coupled models developed within the scope of this work should be understood by taking into consideration the motivation described in the introduction of this thesis. Both the phase-field fracture and coupled fracture-diffusion problems models may now be used to simulate the behavior of all-solid-state composite batteries provided that (1) the experimental campaign recently initiated leads to an appropriate characterization of the material properties required as input data for these models and (2) further validation steps and modeling improvements are carried out. The current ambition is to obtain, from the numerical models, a valuable tool providing the ability not only to (1) predict and explain in the most detailed way the complex physical phenomena involving several fields but also (2) establish an iterative material and structural design methodology without the need to rely on expensive and time consuming experimental tests. However, we should also pose the question *Under which conditions should the phase-field fracture model for coupled problems be used?* before applying this or more elaborate future versions of the phase field model to study the damage tolerance of advanced materials, for which phenomenological damage models such as the one addressed in the literature survey lead to remarkably fast and accurate numerical results.

Part VI

Appendix

Chapter A

Peak stress for a 1D bar in tension with prescribed displacement

Consider the 1D bar shown in Fig. A.1 with its end fixed at $x = 0$ and prescribed displacement $\bar{u}$ at $x = L$. Assuming a second order quadratic approximation for the crack surface density, the governing equations for this problem are

$$\begin{cases} \frac{\mathrm{d}\sigma_x}{\mathrm{d}x} = 0, \quad in\Omega & \text{(Elasticity equilibrium Eq.)} \\ u_x(0) = 0, \quad u_x(L) = \bar{u} & \text{(Elasticity BCs)} \\ \\ (1-d)\psi - \frac{G_c}{2l_0}d + \frac{G_c l_0}{2}\frac{\mathrm{d}^2 d}{\mathrm{d}x^2} = 0, \text{ in } \Omega & \text{(PF equilibrium equation)} \\ \frac{\mathrm{d}d}{\mathrm{d}x} = 0, \quad x = 0, \ x = L & \text{(PF BCs)} \end{cases} \tag{A.1}$$

Assuming linear elastic behavior, the elastic strain energy Ψ is given by $\Psi = 1/2E\left(\bar{u}^2/L^2\right)$. Substituting in the governing equation for the PF in A.1, solving the equation at $x = 0 \vee x = L$ where the Neumman-type BCs provided in A.1 are prescribed

$$E\left(\frac{\bar{u}}{L}\right)^2 - \left[\frac{\mathcal{G}_c}{l_0} + E\left(\frac{\bar{u}}{L}\right)^2\right] \cdot d = 0. \tag{A.2}$$

The closed-form solution for d is thus given by the following equivalent expressions,

$$\begin{aligned} d = \frac{E\left(\frac{\bar{u}}{L}\right)^2}{\frac{\mathcal{G}_c}{l_0} + E\left(\frac{\bar{u}}{L}\right)^2} &= \frac{1}{1 + \frac{\mathcal{G}_c L^2}{E\bar{u}^2 l_0}} \\ &= \frac{El_0\bar{u}^2}{\mathcal{G}_c L^2 + El_0\bar{u}^2} \end{aligned} \tag{A.3}$$

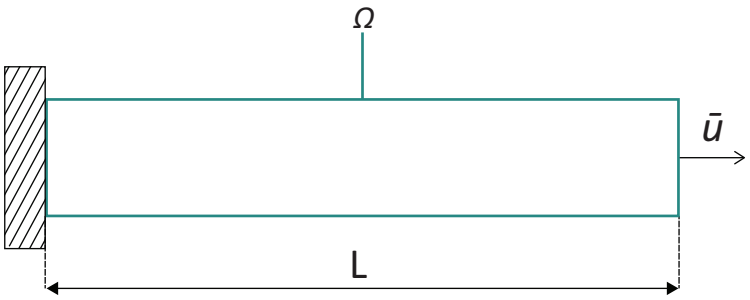


Figure A.1: Fixed-free 1D bar with homogeneous damage growth and prescribed displacement at the free end

Considering a quadratic strain energy degradation function $\omega(d)$, σ_x is given by

$$\sigma_x = (1-d)^2 \cdot \tilde{\sigma}_x \ = (1-d)^2 \cdot \frac{E\bar{u}}{L} \tag{A.4}$$

where $\tilde{\sigma}_x$ is the undamaged stress. Then, the relation $\sigma_x = \sigma_x(\bar{u})$ is

$$\begin{aligned} \sigma_x &= \left[\frac{\mathcal{G}_c L^2}{(\mathcal{G}_c L^2 + E\bar{u}^2 l_0)}\right]^2 \frac{E}{L} \cdot \bar{u} \\ &= \mathcal{G}_c^2 L^3 E \cdot \frac{\bar{u}}{(\mathcal{G}_c L^2 + E l_0 \bar{u}^2)^2}. \end{aligned} \tag{A.5}$$

Defining $C = \mathcal{G}_c^2 L^3 E$ and taking the derivative of stress with respect to $\bar{u}$, the displacement $\bar{u}_c$ at peak stress, σ_c, is found,

$$\begin{aligned} \frac{\mathrm{d}}{\mathrm{d}\bar{u}}(\sigma_x/C) &= \left(\mathcal{G}_c L^2 + E\bar{u}^2 l_o\right)^2 - 2\left(\mathcal{G}_c L^2 + E\bar{u}^2 l_0\right) \cdot 2E\bar{u} l_0 \bar{u} \\ &= \frac{3(El_0)^2}{L^4}\bar{u}^4 + \frac{2El_0\mathcal{G}_c}{L^2}\bar{u}^2 - \mathcal{G}_c^2 = 0. \end{aligned} \tag{A.6}$$

Replacing $\alpha = \bar{u}^2$ in Eq. A.6, and evaluating the positive root α_c of the resulting quadratic expression on α ($\bar{u}_c^2 >= 0$)

$$\begin{aligned} \alpha_c &= \frac{-2\frac{El_0\mathcal{G}_c}{L^2} + \sqrt{4(El_0\mathcal{G}_c)^2 L^{-4} + 12(El_0\mathcal{G}_c)^2 L^{-4}}}{6(El_o)^2 L^{-4}} \\ &= \frac{1}{3}\frac{\mathcal{G}_c L^2}{El_0} \end{aligned} \tag{A.7}$$

the peak stress can, thus, be computed as a function of a set of parameters, $\sigma_c = \sigma_c(\mathcal{G}_c, E, l_0)$

$$\begin{aligned} \sigma_c &= \mathcal{G}_c^2 L^3 E \frac{1/\sqrt{3}\sqrt{\mathcal{G}_c/(El_0)}L}{(1/3L^2\mathcal{G}_c + \mathcal{G}_c L^2)^2} \\ &= \frac{9}{16}\sqrt{\frac{\mathcal{G}_c E}{3l_0}}. \end{aligned} \tag{A.8}$$

The expression A.8 may be re-written with l_0 as the dependent variable,

$$l_0 = \frac{27}{256}\frac{E\mathcal{G}_c}{\sigma_c^2}. \tag{A.9}$$

Eq. A.9 is valid for 1D prescribed displacement problems involving second-order quadratic approximations for the crack surface density γ, where a homogeneous evolution of the PF ($\nabla d = 0$) or the PF evolution at $\partial\Omega$ is studied. This equation has led several authors to regard l_0 as a material parameter (derived from other materials parameters typically determined by experiments) in their models, especially when the so-called engineering approach is considered.

Bibliography

[1] J. Reinoso, M. Paggi, and C. Linder, "Phase field modeling of brittle fracture for enhanced assumed strain shells at large deformations: formulation and finite element implementation," Computational Mechanics, vol. 59, no. 6, pp. 981–1001, 2017.

[2] T. Anderson and T. Anderson, Fracture Mechanics: Fundamentals and Applications, Third Edition. Taylor & Francis, 2005.

[3] F. Danzi, P. P. Camanho, and M. H. Braga, "An all-solid-state coaxial structural battery using sodium-based electrolyte," Molecules, vol. 26, no. 17, 2021.

[4] F. Danzi, R. M. Salgado, J. E. Oliveira, A. Arteiro, P. P. Camanho, and M. H. Braga, "Structural batteries: A review," Molecules, vol. 26, no. 8, 2021.

[5] R. M. Salgado, F. Danzi, J. E. Oliveira, A. El-Azab, P. P. Camanho, and M. H. Braga, "The latest trends in electric vehicles batteries," Molecules, vol. 26, no. 11, 2021.

[6] H. Santos and V. Silberschmidt, Finite Element Modelling of 2D Brittle Fracture: The Phase-Field Approach, pp. 1–21. Springer, Cham, 04 2015.

[7] A. Egger, U. Pillai, K. Agathos, E. Kakouris, E. Chatzi, I. A. Aschroft, and S. P. Triantafyllou, "Discrete and phase field methods for linear elastic fracture mechanics: A comparative study and state-of-the-art review," Applied Sciences, vol. 9, no. 12, 2019.

[8] M. Kuna, Finite Elements in Fracture Mechanics: Theory - Numerics - Applications. Solid Mechanics and Its Applications, Springer Netherlands, 2013.

[9] P. Areias, M. Msekh, and T. Rabczuk, "Damage and fracture algorithm using the screened poisson equation and local remeshing," Engineering Fracture Mechanics, vol. 158, pp. 116–143, 2016.

[10] V. Carollo, T. Guillén-Hernández, J. Reinoso, and M. Paggi, "Recent advancements on the phase field approach to brittle fracture for heterogeneous materials and structures," Advanced Modeling and Simulation in Engineering Sciences, vol. 5, no. 1, p. 8, 2018.

[11] M. Ambati, T. Gerasimov, and L. De Lorenzis, "A review on phase-field models of brittle fracture and a new fast hybrid formulation," Computational Mechanics, vol. 55, 12 2014.

[12] G. Molnár and A. Gravouil, "2d and 3d abaqus implementation of a robust staggered phase-field solution for modeling brittle fracture," Finite Elements in Analysis and Design, vol. 130, pp. 27–38, 2017.

[13] I. Escobar, M. R. Tupek, and J. E. Bishop, "Brittle fracture phase-field modeling of a short-rod specimen," Report SAND2015-8420; Other: 607509 United States 10.2172/1225864 Other: 607509 SNL English, Sandia National Lab. (SNL-NM), Albuquerque, NM (United States), 2015.

[14] G. Voyiadjis, Handbook of Damage Mechanics: Nano to Macro Scale for Materials and Structures. Springer New York, 2014.

[15] G. Voyiadjis, P. Kattan, and M. Yousef, Some Basic Issues of Isotropic and Anisotropic Continuum Damage Mechanics, pp. 1–37. Springer, New York, NY, 01 2014.

[16] Y.-Q. Guo, Y. Li, B. Abbès, H. Naceur, and A. Halouani, Damage Prediction in Metal Forming Process Modeling and Optimization: Simplified Approaches, pp. 765–813. New York, NY: Springer New York, 2015.

[17] A. Cauvin and R. B. Testa, "Damage mechanics : basic variables in continuum theories," International Journal of Solids and Structures, vol. 36, pp. 747–761, 1999.

[18] G. Voyiadjis, P. Kattan, and Z. Taqieddin, Use of Fabric Tensors in Continuum Damage Mechanics of Solids with Micro-cracks, pp. 76–109 (printed version) http://link.springer.com/referenceworkentry/10.1007/978. Springer, New York, NY, 09 2015.

[19] P. Maimí, P. Camanho, J. Mayugo, and C. Dávila, "A continuum damage model for composite laminates: Part i – constitutive model," Mechanics of Materials, vol. 39, no. 10, pp. 897–908, 2007.

[20] P. Maimí, P. Camanho, J. Mayugo, and C. Dávila, "A continuum damage model for composite laminates: Part ii – computational implementation and validation," Mechanics of Materials, vol. 39, no. 10, pp. 909–919, 2007.

[21] J. Lemaitre, "A Continuous Damage Mechanics Model for Ductile Fracture," Journal of Engineering Materials and Technology, vol. 107, pp. 83–89, 01 1985.

[22] U. Cicekli, G. Z. Voyiadjis, and R. K. Abu Al-Rub, "A plasticity and anisotropic damage model for plain concrete," International Journal of Plasticity, vol. 23, no. 10, pp. 1874–1900, 2007. In honor of Professor Dusan Krajcinovic.

[23] S. T. Pinho, C. G. Dávila, P. P. Camanho, L. Iannucci, and P. Robinson, "Failure models and criteria for frp under-in-plane or three-dimensional stress states including shear non-linearity," NASA/TM-2003-213530, 2005.

[24] S. Biner, Programming Phase-Field Modeling. Springer International Publishing, 2017.

[25] K. Elder and N. Provatas, Introduction, ch. 1, pp. 1–7. John Wiley Sons, Ltd, 2010.

[26] A. Salhoumi and P. Galenko, "Gibbs–thomson condition for the rapidly moving interface in a binary system," Physica A: Statistical Mechanics and its Applications, vol. 447, pp. 161–171, 2016.

[27] A. Jokisaari, P. Voorhees, J. Guyer, J. Warren, and O. Heinonen, "Benchmark problems for numerical implementations of phase field models," Computational Materials Science, vol. 126, pp. 139–151, 2017.

[28] N. Moelans, B. Blanpain, and P. Wollants, "An introduction to phase-field modeling of microstructure evolution," Calphad, vol. 32, no. 2, pp. 268–294, 2008.

[29] G. Francfort and J.-J. Marigo, "Revisiting brittle fracture as an energy minimization problem," Journal of the Mechanics and Physics of Solids, vol. 46, no. 8, pp. 1319–1342, 1998.

[30] B. Bourdin, Une Méthode variationnelle en mécanique de la rupture. PhD thesis, Université Paris-Nord, 1998. Thèse de doctorat dirigée par Francfort, Gilles Mathématiques Paris 13 1998.

[31] B. Bourdin, G. Francfort, and J.-J. Marigo, "Numerical experiments in revisited brittle fracture," Journal of the Mechanics and Physics of Solids, vol. 48, no. 4, pp. 797–826, 2000.

[32] L. Ambrosio and V. M. Tortorelli, "Approximation of functional depending on jumps by elliptic functional via t-convergence," Communications on Pure and Applied Mathematics, vol. 43, no. 8, pp. 999–1036, 1990.

[33] T. Gerasimov and L. De Lorenzis, "On penalization in variational phase-field models of brittle fracture," Computer Methods in Applied Mechanics and Engineering, vol. 354, pp. 990–1026, 2019.

[34] C. Miehe, F. Welschinger, and M. Hofacker, "Thermodynamically consistent phase-field models of fracture: Variational principles and multi-field fe implementations," International Journal for Numerical Methods in Engineering, vol. 83, no. 10, pp. 1273–1311, 2010.

[35] O. Gueltekin, H. Dal, and G. Holzapfel, "A phase-field approach to model fracture of arterial walls: Theory and finite element analysis," Computer Methods in Applied Mechanics and Engineering, vol. 312, pp. 542–566, 04 2016.

[36] C. Miehe, M. Hofacker, and F. Welschinger, "A phase field model for rate-independent crack propagation: Robust algorithmic implementation based on operator splits," Computer Methods in Applied Mechanics and Engineering, vol. 199, no. 45, pp. 2765–2778, 2010.

[37] C. Miehe, L.-M. Schänzel, and H. Ulmer, "Phase field modeling of fracture in multi-physics problems. part i. balance of crack surface and failure criteria for brittle crack propagation in thermo-elastic solids," Computer Methods in Applied Mechanics and Engineering, vol. 294, pp. 449–485, 2015.

[38] A. Dean, P. Asur Vijaya Kumar, J. Reinoso, C. Gerendt, M. Paggi, E. Mahdi, and R. Rolfes, "A multi phase-field fracture model for long fiber reinforced composites based on the puck theory of failure," Composite Structures, vol. 251, p. 112446, 2020.

[39] M. Paggi and J. Reinoso, "Revisiting the problem of a crack impinging on an interface:a modeling framework for the interaction between the phase field approach for brittle fracture and the interface cohesive zone model," Computer Methods in Applied Mechanics and Engineering, vol. 321, pp. 145–172, 2017.

[40] B. Bourdin, G. Francfort, and J.-J. Marigo, "The variational approach to fracture," Journal of Elasticity, vol. 91, pp. 5–148, 04 2008.

[41] M. J. Borden, T. J. Hughes, C. M. Landis, A. Anvari, and I. J. Lee, "A phase-field formulation for fracture in ductile materials: Finite deformation balance law derivation, plastic degradation, and stress triaxiality effects," Computer Methods in Applied Mechanics and Engineering, vol. 312, pp. 130–166, 2016. Phase Field Approaches to Fracture.

[42] J.-Y. Wu, "A unified phase-field theory for the mechanics of damage and quasi-brittle failure," Journal of the Mechanics and Physics of Solids, vol. 103, pp. 72–99, 2017.

[43] J.-Y. Wu and V. P. Nguyen, "A length scale insensitive phase-field damage model for brittle fracture," Journal of the Mechanics and Physics of Solids, vol. 119, pp. 20–42, 2018.

[44] G. Lancioni and G. Royer-Carfagni, "The variational approach to fracture mechanics. a practical application to the french panthéon in paris," Journal of Elasticity, vol. 95, no. 1-2, pp. 1–30, 2009.

[45] H. Amor, J.-J. Marigo, and C. Maurini, "Regularized formulation of the variational brittle fracture with unilateral contact: Numerical experiments," Journal of the Mechanics and Physics of Solids, vol. 57, no. 8, pp. 1209–1229, 2009.

[46] A. Quintanas-Corominas, A. Turon, J. Reinoso, E. Casoni, M. Paggi, and J. Mayugo, "A phase field approach enhanced with a cohesive zone model for modeling delamination induced by matrix cracking," Computer Methods in Applied Mechanics and Engineering, vol. 358, p. 112618, 2020.

[47] V. Lubarda, D. Krajcinovic, and S. Mastilovic, "Damage model for brittle elastic solids with unequal tensile and compressive strengths," Engineering fracture mechanics, vol. 49, no. 5, pp. 681–697, 1994.

[48] J. Bleyer and R. Alessi, "Phase-field modeling of anisotropic brittle fracture including several damage mechanisms," Computer Methods in Applied Mechanics and Engineering, vol. 336, pp. 213–236, 2018.

[49] E. Tanné, T. Li, B. Bourdin, J.-J. Marigo, and C. Maurini, "Crack nucleation in variational phase-field models of brittle fracture," Journal of the Mechanics and Physics of Solids, vol. 110, pp. 80–99, 2018.

[50] A. Singh and S. Pal, "Multi-phase field modeling for various fracture mechanisms in composites," Engineering Fracture Mechanics, vol. 241, p. 107348, 2021.

[51] C. Miehe, L.-M. Schänzel, and H. Ulmer, "Phase field modeling of fracture in multi-physics problems. part i. balance of crack surface and failure criteria for brittle crack propagation in thermo-elastic solids," Computer Methods in Applied Mechanics and Engineering, vol. 294, 12 2014.

[52] L. Wang, J. Lee, M. Anitescu, A. Azab, L. C. McInnes, T. Munson, and B. Smith, "A differential variational inequality approach for the simulation of heterogeneous materials," in Proceedings of SciDAC 2011 Conference, 2011.

[53] J.-S. Pang and D. E. Stewart, "Differential variational inequalities," Mathematical programming, vol. 113, no. 2, pp. 345–424, 2008.

[54] T. Gerasimov, N. Noii, O. Allix, and L. De Lorenzis, "A non-intrusive global/local approach applied to phase-field modeling of brittle fracture," Advanced Modeling and Simulation in Engineering Sciences, vol. 5, 05 2018.

[55] C. Miehe, M. Hofacker, and F. Welschinger, "A phase field model for rate-independent crack propagation: Robust algorithmic implementation based on operator splits," Computer Methods in Applied Mechanics and Engineering, vol. 199, no. 45, pp. 2765–2778, 2010.

[56] T. Gerasimov, U. Römer, J. Vondřejc, H. G. Matthies, and L. De Lorenzis, "Stochastic phase-field modeling of brittle fracture: Computing multiple crack patterns and their probabilities," Computer Methods in Applied Mechanics and Engineering, vol. 372, p. 113353, 2020.

[57] I. Escobar, M. R. Tupek, and J. E. Bishop, "Brittle fracture phase-field modeling of a short-rod specimen," tech. rep., Sandia National Lab.(SNL-NM), Albuquerque, NM (United States), 2015.

[58] P. Areias, T. Rabczuk, and M. Msekh, "Phase-field analysis of finite-strain plates and shells including element subdivision," Computer Methods in Applied Mechanics and Engineering, vol. 312, pp. 322–350, 2016. Phase Field Approaches to Fracture.

[59] A. C. Hansen-Dörr, R. de Borst, P. Hennig, and M. Kästner, "Phase-field modelling of interface failure in brittle materials," Computer Methods in Applied Mechanics and Engineering, vol. 346, pp. 25–42, 2019.

[60] R. Alessi, J.-J. Marigo, C. Maurini, and S. Vidoli, "Coupling damage and plasticity for a phase-field regularisation of brittle, cohesive and ductile fracture: One-dimensional examples," International Journal of Mechanical Sciences, vol. 149, pp. 559–576, 2018.

[61] J. Reinoso, A. Arteiro, M. Paggi, and P. Camanho, "Strength prediction of notched thin ply laminates using finite fracture mechanics and the phase field approach," Composites Science and Technology, vol. 150, pp. 205–216, 2017.

[62] T. Guillén-Hernández, I. G. García, J. Reinoso, and M. Paggi, "A micromechanical alysis of inter-fiber failure in long reinforced composites based on the phase field approach of fracture combined with the cohesive zone model," International Journal of Fracture, vol. 220, no. 2, pp. 181–203, 2019.

[63] R. de Borst and C. V. Verhoosel, "Gradient damage vs phase-field approaches for fracture: Similarities and differences," Computer Methods in Applied Mechanics and Engineering, vol. 312, pp. 78–94, 2016. Phase Field Approaches to Fracture.

[64] G. Z. Voyiadjis and N. Mozaffari, "Nonlocal damage model using the phase field method: Theory and applications," International Journal of Solids and Structures, vol. 50, no. 20, pp. 3136–3151, 2013.

[65] C. J. Permann, D. R. Gaston, D. Andrš, R. W. Carlsen, F. Kong, A. D. Lindsay, J. M. Miller, J. W. Peterson, A. E. Slaughter, R. H. Stogner, and R. C. Martineau, "Moose: Enabling massively parallel multiphysics simulation," SoftwareX, vol. 11, p. 100430, 2020.

[66] A. Singh and S. Pal, "Coupled chemo-mechanical modeling of fracture in polycrystalline cathode for lithium-ion battery," International Journal of Plasticity, vol. 127, p. 102636, 2020.

[67] A. Shadowitz, The Electromagnetic Field. Dover Books on Physics, Dover Publications, 2012.

[68] P. Nithiarasu, R. Lewis, and K. Seetharamu, Fundamentals of the Finite Element Method for Heat and Mass Transfer. Wiley Series in Computational Mechanics, Wiley, 2016.

[69] K. Bathe, Finite Element Procedures. Prentice Hall, 2006.

[70] B. S. Kirk, J. W. Peterson, R. H. Stogner, and G. F. Carey, "`libMesh`: A C++ library for parallel adaptive mesh refinement/coarsening simulations," Engineering with Computers, vol. 22, no. 3–4, pp. 237–254, 2006. `http://dx.doi.org/10.1007/s00366-006-0049-3`.

[71] D. W. Kelly, J. P. De S. R. Gago, O. C. Zienkiewicz, and I. Babuska, "A posteriori error analysis and adaptive processes in the finite element method: Part i—error analysis," International Journal for Numerical Methods in Engineering, vol. 19, no. 11, pp. 1593–1619, 1983.

[72] T. Belytschko, W. Liu, and B. Moran, Nonlinear Finite Elements for Continua and Structures. John Wiley Sons, Ltd, 2000.

[73] J.-Y. Wu, Y. Huang, and V. P. Nguyen, "On the bfgs monolithic algorithm for the unified phase field damage theory," Computer Methods in Applied Mechanics and Engineering, vol. 360, p. 112704, 2020.

[74] J. D. Hales, S. R. Novascone, R. L. Williamson, D. R. Gaston, and M. R. Tonks, "Solving nonlinear solid mechanics problems with the jacobian-free newton krylov method," Computer Modeling in Engineering & Sciences, vol. 84, no. 2, pp. 123–154, 2012.

[75] W. Xianmeng, W. Mingyu, H. Xiao, W. Zhaoshun, C. Yinyu, L. Xu, and G. Suxuan, "Multi-physics coupling simulation in virtual reactors," SIMULATION, vol. 97, no. 10, pp. 687–702, 2021.

[76] Y. Navidtehrani, C. Betegón, and E. Martínez-Pañeda, "A simple and robust abaqus implementation of the phase field fracture method," Applications in Engineering Science, vol. 6, p. 100050, 2021.

[77] C. Sun and Z.-H. Jin, "Chapter 3 - the elastic stress field around a crack tip," in Fracture Mechanics (C. Sun and Z.-H. Jin, eds.), pp. 25–75, Boston: Academic Press, 2012.

[78] Y. Zhan, "Multilevel modeling of fiber-reinforced concrete and application to numerical simulations of tunnel lining segments," 2016.

[79] M. H. Braga, J. E. Oliveira, T. Kai, A. J. Murchison, A. J. Bard, and J. B. Goodenough, "Extraordinary dielectric properties at heterojunctions of amorphous ferroelectrics," Journal of the American Chemical Society, vol. 140, no. 51, pp. 17968–17976, 2018.

[80] J. Pyo, H.-W. Park, M.-S. Jang, J.-S. Choi, S. K. Sathish Kumar, and C.-G. Kim, "Tubular laminated composite structural battery," Composites Science and Technology, vol. 208, p. 108646, 2021.

[81] D. Carlstedt and L. E. Asp, "Performance analysis framework for structural battery composites in electric vehicles," Composites Part B: Engineering, vol. 186, p. 107822, 2020.

[82] A. K. Singh, L. Cao, J. Ma, J. Seo, C. E. Bakis, Y. Zhang, M. A. Hickner, and C. D. Rahn, "Design, manufacture and test of a novel structural battery based on sandwich construction," Journal of Sandwich Structures & Materials, vol. 17, no. 6, pp. 666–690, 2015.

[83] J. Galos, A. Afaghi Khatibi, and A. Mouritz, "Vibration and acoustic properties of composites with embedded lithium-ion polymer batteries," Composite Structures, vol. 220, p. 10, 2019.

[84] N. thin ply technology, "Product datasheet-thinpregŮ 80ep-736/cf.." `https://www.thinplytechnology.com/assets/mesimages/NTPT-DS-ThinPreg-736LT-v2.pdf`, 2015. [Online; accessed 09-September-2021].

[85] M. H. Braga, N. S. Grundish, A. J. Murchison, and J. B. Goodenough, "Alternative strategy for a safe rechargeable battery," Energy Environ. Sci., vol. 10, pp. 331–336, 2017.

[86] M. H. Braga, J. A. Ferreira, V. Stockhausen, J. E. Oliveira, and A. El-Azab, "Novel li3clo based glasses with superionic properties for lithium batteries," J. Mater. Chem. A, vol. 2, pp. 5470–5480, 2014.